JPL Quarterly Technical Review

Volume 2 October 1972 Number 3

Papers on:

Materials
Orbits and Trajectories
Power Sources
Satellite Geodesy
Structural Engineering

Abstracts of:

Technical Reports
Technical Memorandums
JPL Quarterly Technical Review
Open Literature Reporting

Jet Propulsion Laboratory/California Institute of Technology

JPL Quarterly Technical Review

Volume 2 October 1972 Number 3

Contents

1 3-D Multilateration: A Precision Geodetic Measurement System

P. R. Escobal, H. F. Fliegel, R. M. Jaffe, P. M. Muller, K. M. Ong, O. H. von Roos, and M. S. Shumate

12 An Algorithm for Synthesizing Mass and Stiffness Matrices From Experimental Vibration Modes

R. G. Ross, Jr.

22 Xenon-Filled Silicon Germanium Thermoelectric Generators

F. de Winter

32 Long-Term Aging of Elastomers: Chemorheology of Viton B Fluorocarbon Elastomer

S. H. Kalfayan, R. H. Silver, A. A. Mazzeo, and S. T. Liu

40 Extensional Flow of Bulk Polymers

T. J. Peng

46 A Summary of the Pioneer 10 Maneuver Strategy

R. B. Frauenholz and J. E. Ball

Bibliography of Current Reporting

64 Author Index With Abstracts

125 Subject Index

139 Publication Index

JPL Quarterly Technical Review Volume 2, Number 3 October 1972

Index: Earth surface, environmental sciences, masers and lasers, radio astronomy

3-D Multilateration: A Precision Geodetic Measurement System

P. R. Escobal, H. F. Fliegel, R. M. Jaffe, P. M. Muller,
K. M. Ong, and O. H. von Roos

Mission Analysis Division

M. S. Shumate

Telecommunications Division

The assessment of earthquake hazards, indication of probable locations for earthquakes, and the eventual possibility of earthquake prediction or premonitory warning have become an important part of the NASA Earth Physics Applications Program. The key to moving toward these goals is believed to be precision monitoring of the near- and far-field strain buildup and release within a few hundred kilometers of active fault zones such as the San Andreas. A system with the capability of determining 1-cm accuracy station positions in three dimensions has been designed using pulsed laser Earth satellite tracking stations coupled with strictly geometric data reduction.

Introduction

The systems analysis and laboratory demonstration described in this article indicate that a new technique of satellite geodesy, to be called *3-D Multilateration*, can determine the relative three-dimensional coordinates of ground stations within 1 cm over baselines of 20–10,000 km. With this high accuracy, several crucial geodetic applications become possible, including earthquake hazards assessment, precision surveying, plate tectonics, and orbital determination.

Achievement of this accuracy can be attained through use of pulsed lasers to measure simultaneously the slant ranges between an ensemble of six or more ground stations and a compact moving retroreflector whose trajectory is known *a priori* only to the accuracy necessary for aiming the lasers. Specifically, the positions of the satellite- or airplane-carried retroreflector are eliminated from the equations which govern determination of station locations. The trajectory of the retroreflector *and* the locations of the stations are determined in the same solution. The numerical analysis has shown that suitably chosen multi-station configurations result in well-conditioned solutions with very small error magnification of the inherent ranging errors.

Laboratory tests have demonstrated that a laser hardware system with a ranging accuracy of 3 cm can be built from commercially available components. By 1975, at the latest, an accuracy level of 1 cm can be achieved. Costs are probably lower than other proposed systems on a sites-occupied and determined basis.

Nature of the Earth Physics Applications

The basic cause of earthquakes is an unrelieved buildup of strain within the Earth. In many situations, this strain is relieved by a gradual creeping between the crustal blocks on different sides of a fault. However, if the creeping is insufficient to relieve the buildup of strain, an earthquake will eventually result. Many geophysicists now believe that a reasonable estimate of the location, and possibly the approximate time, of major earthquakes in known fault zones can be made by relating: (1) the amount of creeping taking place along the fault, and (2) the strain buildup in a large region surrounding the fault.

There is little problem in measuring the creeping along the fault since the motion takes place over relatively short distances. However, in order to evaluate the strain buildup in a large region surrounding the fault, it is necessary to measure precisely the relative motion of points in various parts (including the periphery) of this large region. If this motion is to be evaluated within a period of 1 to 2 yr, it will be necessary to measure distances as large as 1000 km with an accuracy of 3 cm or better. At present, there is no technique which is capable of making such measurements.

The 3-D Multilateration technique appears to provide not only a 1-cm accuracy distance measuring capability, but also determines each station position in *three dimensions.* This allows complete evaluation of the strain field. Furthermore, since the 3-D Multilateration technique will require only 1–5 days to obtain raw data and process this data into station positions, it will be possible to detect the presence of rapidly occurring ground deformations which may give a premonitory indication of earthquakes.

It should be noted that the 3-D Multilateration technique can be used in facets of geophysical analysis not directly related to earthquake prediction. This technique is sufficiently flexible to permit a wide variety of applications, as illustrated in Figure 1.

In summary, if the performance of the 3-D Multilateration technique demonstrated in this article is realized, not only will science be provided with a valuable tool for investigation of tectonic phenomena, but there is a significant possibility that geophysicists will be able to predict the location, and perhaps the approximate time, of future earthquakes.

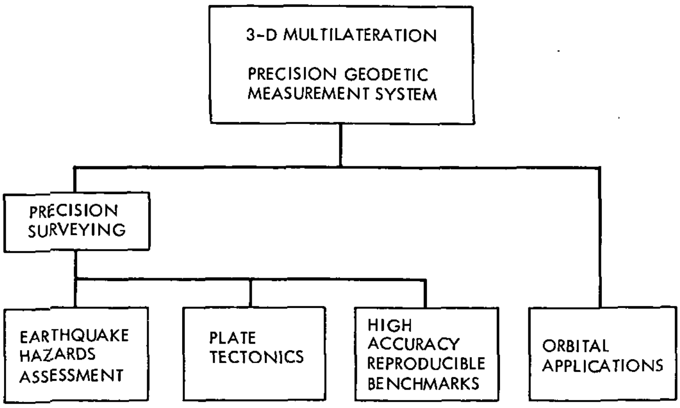

Figure 1. Applications of 3-D Multilateration

The Requirement for 1-cm Position Determinations

Fault motions along the San Andreas are in the range of 3 cm per year, as measured near the fault zones. Tectonic plate motions might be as high as 5–10 cm per year. If we assume that 2 cm per year is a reasonable motion threshold in creep determinations, then it can be easily calculated that the accuracy with which station positions can be determined (expressed in centimeters) is also the number of years over which sites must be monitored in order to prove the motion is real, and obtain a safe quantitative measure of it (assuming a 2:1 motion-threshold to error-level ratio).

For this reason, an accuracy of 5 cm or better is required in these applications, and 1 cm is a highly desirable goal. Systems for station position measurement which fail to yield all three dimensional components, or which cannot be refined to approach 1 cm, are weak in this context of earthquake hazards estimation and precision surveying. For the purpose of the system reported here, 1 cm is the assumed goal, and it is shown that this can be closely approached with equipment and methods of data analysis which currently exist and can be assembled into the 3-D Multilateration hardware-software system.

Description of the 3-D Multilateration Technique

The 3-D Multilateration technique can be implemented through use of a number of ground stations which simultaneously transmit laser pulses to compact reflectors on a moving vehicle, e.g., an airplane or a satellite. Each station evaluates station-to-vehicle range by measuring the time interval between transmission of the original pulse and reception of the reflected pulse. Simultaneous range measurements are then processed so as to yield relative station locations in three dimensions.

The geometric coordinate system used for this system is a relative coordinate system, in which Station 1 is placed at the origin, arbitrary placement of Station 2 fixes the X axis, and arbitrary location of Station 3 defines the X–Y plane of the coordinate system (See Figure 2).

This coordinate system can be linked to the inertial geocentric coordinate system, if desired, via the geographic coordinates of the first three adopted stations. Errors in this transformation, however, have no bearing whatsoever on the *relative* station position determinations necessary for the tectonic applications.

Conceptually, only two stations are required for determination of the baseline between them. In this case, the inertial trajectory in Earth-centered coordinates must be computed and modeled over days, weeks, and even months to permit the data reduction. That is, in the existing dynamic laser tracking systems, several passes of the satellite over two stations are required to permit adequate determination, and these determinations must be done by tying the satellite passes together in geocentric coordinates. The difficulty of modeling spacecraft behavior to sub-meter accuracy levels is well known, and probably limits the dynamic laser systems to accuracies of 20 to 50 cm.

Solving equations simultaneously for both station and satellite positions, thereby eliminating dependence upon trajectory calculation, turns out to be possible if six or more stations range simultaneously. Conceptually, the reason is as follows. Assume six stations range to four reflector positions (not necessarily on the same trajectory). This yields 24 equations which are equal to the number of trajectory parameters (4 × 3) plus the station positions in the above coordinate system (6 × 3 – 6). It turns out, in detailed theoretical analysis, that six stations ranging to four or more points (not in the same plane) are sufficient to solve the 24 simultaneous quadratic equations. It is only necessary that the stations be reasonably located (not in a straight line,

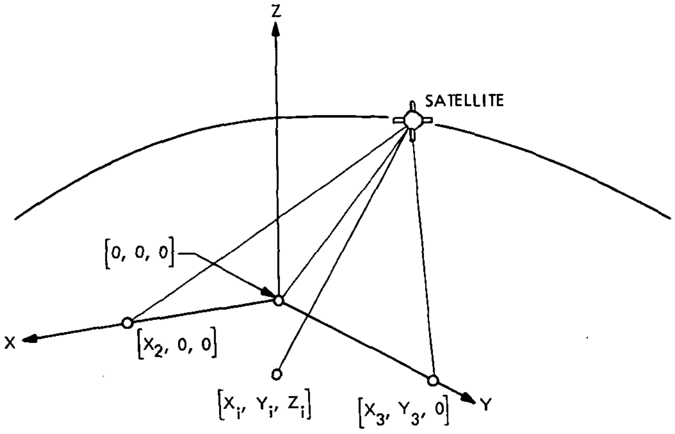

Figure 2. Geometric coordinate system

for example), and that the reflector points not be in a plane (using parts of two different spacecraft passes, for example). Redundant observations contribute to a least squares solution of improved quality, and, in actual operation, thousands of observations may be combined. Since geometric systems are reversible in principle, four stations viewing six trajectory points should also work. This is the case, but only if the four stations are well out of a plane (are intercontinental, for example). This and other special cases noted in Reference 1 are not discussed further here in the interest of brevity.

We see the key point, then, that simultaneous ranging from six or more stations frees laser tracking from the limiting error source of current dynamical approaches. The trajectory need be known only well enough to acquire the spacecraft for tracking, and the limiting accuracy achievable improves from 20 cm to under 1 cm in principle. 3-D Multilateration provides:

(1) The relative three-dimensional coordinates of all six stations utilized in the operational configuration.

(2) The equally precise positions of the moving retroreflector in the adopted coordinate system.

Given six ground stations (Figure 3) which make a sequence of four or more simultaneous strikes over two or more satellite passes separated in time by any arbitrary duration, a mathematically and numerically stable solution for the determination of relative three-dimensional station locations exists, and can be obtained without any knowledge whatsoever of the satellite position.

Hardware System and Accuracy Demonstration

The hardware subsystem for measuring station-vehicle ranges is identical for all station configurations. In order to attain high accuracy range measurements, the subsystem utilizes a new type of pulsed laser. This laser is a mode-locked, Q-spoiled ruby laser, and has the capability of emitting light pulses of very short duration (0.1 ns or less). The subsystem employs a tracking mount to aim transmitting and receiving telescopes at the vehicle. A measurement is made of the time required for a laser pulse to make a round-trip flight from the station to the vehicle-borne retroreflector. This time, measured with a resolution of 0.1 ns, is used in conjunction with an atmospheric model to calculate the range to the vehicle.

Each ground station also contains an X–Y tracking mount for steering the two telescopes, a small computer to direct the tracking mount toward the satellite, timing circuitry, recording equipment, and power supplies. In order to satisfy the requirement for "simultaneous" ranging, the clocks at each station must be synchronized to 3 μs; such synchronization is easily achievable using low-cost components. Synchronization of laser firing to 1 ms is adequate and well within the state of the art; variations of laser firing within this range are compensated for by time-tagging range measurements,

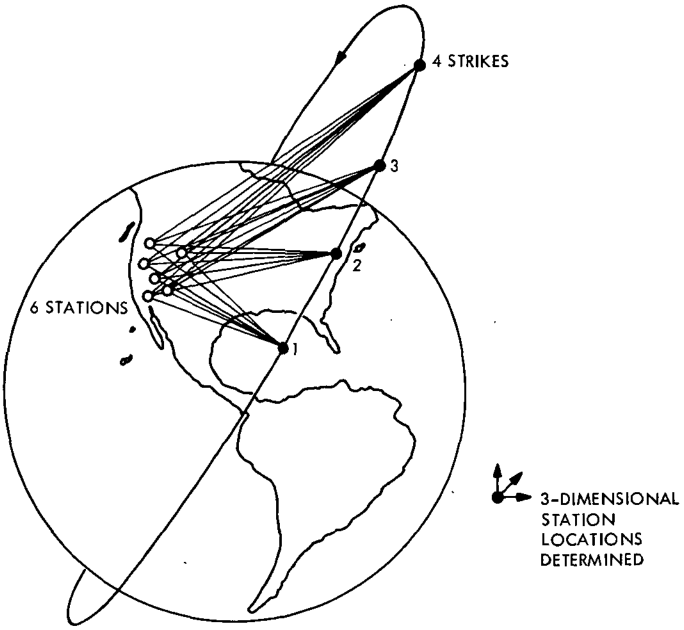

Figure 3. Six-station solution

and interpolating between successive measurements so as to obtain effective simultaneity among stations.

A demonstration ranging system was assembled using commercially available components in order to evaluate the measurement errors produced by current hardware. This system simulated a long distance ranging system over short path lengths by using attenuated return signals. The results obtained with this system show that hardware-related errors in range measurement can be made acceptably small, typically less than 2 cm. Future systems, fabricated circa 1975, can be expected to operate at satellite distances with 1-cm ranging accuracy.

Figure 4 indicates the schematic of hardware components in the system. These can be assembled from commercially available components, packaged compactly, and placed in a transportable van as indicated in Figure 5.

Analysis of System Errors

It is emphasized that the system errors caused by the satellite, Earth constants, and orbital perturbations do *not* enter into the process. In fact, since the proposed techniques are independent of the location of the retroreflector, the only error sources which enter into the range measurement are:

(1) Bias error due to atmospheric delay.

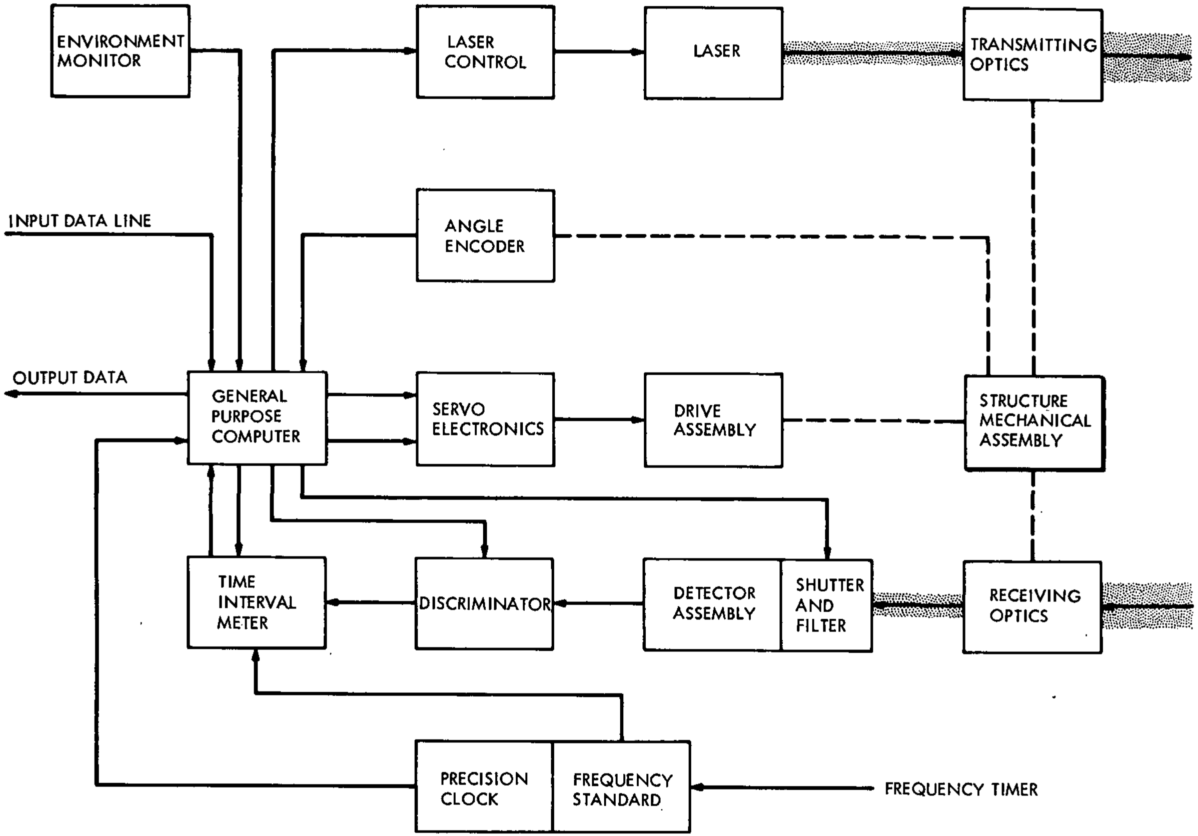

Figure 4. Schematic of laser ranging station hardware

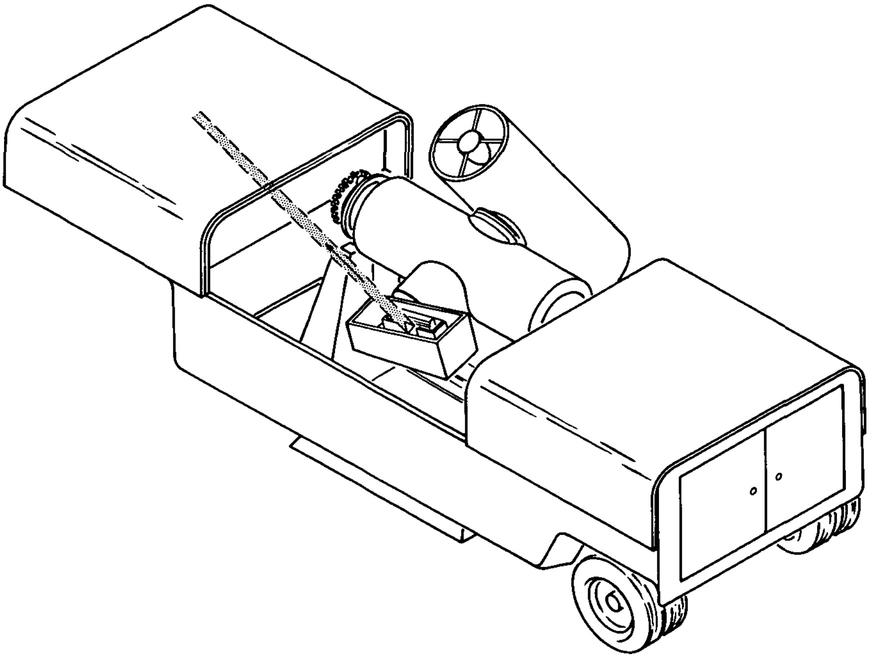

Figure 5. Artist's conception of laser tracking station

(2) Random error due to atmospheric turbulence.

(3) Random equipment measurement error.

(4) Equipment bias error.

It is shown in Reference 1 that a ranging subsystem can be fabricated in which the net effect of these errors will lead to ranging accuracy of 1 cm.

Careful sensitivity analyses of the system have been made. In addition, a detailed Monte Carlo numerical simulation of the system was conducted, in which the raw range measurements were corrupted by random noise, and the station parameters were solved for various configurations and data sets. The conclusions appear in detail in Reference 1, and include:

(1) For a single data set consisting of two satellite passes at different altitudes (such as 500 and 750 km), with 50 ranging points taken to each, the standard deviation of error in station coordinates ranged from one to four times the random range error (error magnifications of 1 to 4 times).

(2) For 10 passes as above, in a combined solution, the error in station coordinate determinations ranged from 0.1 to 1.0 times the ranging error.

We can conclude from this that, given a 1-cm ranging system, station positions of 3- to 5-cm accuracy can be obtained on each clear-weather day of observation. For 10 such days, which would be a normal site-occupancy time, accuracy of 0.3 to 1.0 cm would be obtained. No other proposed system of station position measurement has as much promise of reaching such high accuracy.

The effect of biases was studied briefly, with the conclusion that biases tend to cancel out due to the varieties of geometry obtained over different data sets, and that the system is therefore stable in the presence of bias-type errors. Detailed study of bias plus random errors in the ranging systems will be conducted in the coming months, but the results are not expected to cause any changes of consequence within the conclusions stated in this article.

Comparison With Other Techniques

There are three other techniques which are comparable to the 3-D Multilateration technique:

(1) The Geodolite.

(2) The Goddard Laser Ranging System.

(3) Very Long Baseline Interferometry.

Spectra-Physics of Mountainview, California, manufactures a laser-ranging device known as the *Geodolite*, which is capable of measuring the distance between points on the Earth's surface. The Geodolite can measure only line-of-sight distances, but provides excellent accuracy over its severely constrained range. For example, the U. S. Geological Survey (USGS) has used a Geodolite to measure baselines of 30 km with accuracies of 1 cm or better; however, in order to achieve this accuracy, the USGS combined a number of partially redundant measurements from different benchmarks, and then corrected these raw measurements with temperature and humidity data obtained by overflying the baselines with a helicopter. In summary, although the Geodolite appears to be an excellent device for obtaining high accuracy distance measurements over short baselines, it is not an acceptable tool for measuring the three-dimensional components of distance over long baselines. (Although it would be conceptually possible to augment the Geodolite's measurements with measurements of vertical motion provided by tiltmeters or gravimeters, such systems are not feasible in practice.)

The second technique was pioneered by Goddard Space Flight Center. It employs laser ranging between two stations and a satellite retroreflector. Three-dimensional station locations are deduced from processing data over long arcs of weeks and months. This is the "dynamic system" referred to above. Polar motion, possibly universal time, and long period orbital information can be secured in addition to station locations. Current accuracies range in the 0.3- to 2.0-m range depending upon which parameter is considered, with station locations tending toward accuracy levels of 1 to 2 m. As has been noted above, long period orbit determination and modeling restricts the accuracy of station parameter solutions. It is doubtful if the orbit determination capabilities can be sufficiently improved in the foreseeable future to break the 10-cm accuracy level. This is precisely why the geometric techniques are being considered in the context of station location solutions.

Very Long Baseline Interferometry (VLBI) can deduce station locations in three dimensions by measuring differential time of arrival at two or more stations of identical random radio signals from extragalactic radio sources.

The ability to convert VLBI observations into accurate geophysical measurements is limited mainly by Earth atmospheric and charged-particle uncertainties. Dual-frequency VLBI has promise for charged-particle calibrations, and water vapor radiometry are promising for atmospheric wet-component calibration.

Recent VLBI experiments have demonstrated a formal instrumental precision of 5 cm for measurement of two components of a 16-km baseline using 4 h of data. Caution is required in extrapolating these 5-cm results to longer baselines as the systematic atmospheric and charged-particle errors may dominate. Further experiments are planned, and 3-cm or better three-dimensional station location determination accuracy is forecast for the 1975 time frame.

Advantages of this method include: (1) ability to develop 3 cm or better station location accuracy in geocentric coordinates, independent of the separation between stations, and relative to a nearly invariant extragalactic set of sources. (2) The system is virtually weather-independent. (3) Portable stations are feasible (ARIES System: Astronomical Radio Interferometric Earth Surveying). (4) There is no requirement for orbiting reflectors, or to transmit any radio or light signals from the Earth. VLBI is entirely passive, using only natural radio signals.

Possible disadvantages include dependence upon experimental frequency and digital recording systems, the larger (than optical system) dependence on charged-particle and atmospheric corrections, the need for time and polar motion calibrations (in the geocentric system), and possible reliance on major radio tracking facilities. None of these constraints appears to be critical, and the method has great promise.

Implementation and Operational Considerations

The dry atmosphere of the Earth can be calibrated to 1 cm or better, and the hardware will be operational at about the 1-cm level. Weather imposes a constraint until the number of operational stations goes above 10 or 12, as it is necessary to have at least six stations viewing simultaneously. For employment in a favorable climate, over a local area (several hundred kilometers), analysis indicates that eight stations is sufficient to guarantee substantial data returns.

The main implementational disadvantage of the system is that approximately eight stations must be constructed. Reference 1 includes cost estimates for station procurement in lots of four to eight. This estimates that the station cost is one-half to one-third that of competing systems. Operation is intended to be semi-automatic, to keep operational costs down. If these difficult cost and operation constraints can be met, total system cost should be at least comparable to other competing techniques. On a per site-occupied basis, even including substantial transportation costs, the price is probably less than any currently considered system. This arises from the larger number of stations.

As was seen in Figure 5, the system is carried in a single trailer, to be emplaced on prepared sites. An eight-station system should be able to comfortably occupy 50 to 80 sites, twice per year, at a reasonable transportation and manpower cost. This would create a substantial number of precision surveying points suitable for a major geophysical monitoring program as described above.

Conclusions

The study described here, and detailed in Reference 1, has shown that a geometric, multi-station, laser tracking system is feasible and will deliver cost effective, 1-cm accuracy, three-dimensional station position information suitable for major advances in earthquake hazard estimation and geophysics.

The key point of the systems proposal is obtaining freedom from errors in Earth satellite trajectory computations, which currently limits existing two-station laser systems to an accuracy of 20 to 100 cm. The price of this freedom and markedly increased accuracy is six or more stations simultaneously operational. The cost and complexity of such networks does not appear to be prohibitive, and is, on a site-occupied basis at least, quite competitive with existing laser systems and proposed very long baseline radio interferometry approaches.

The proposed 3-D Multilateration system is the only system currently analyzed which has been shown to be capable of 1 cm and lesser errors in three-dimensional station coordinate determinations, which can be operational in the 1975 time frame.

Reference

1. Escobal, P. R., et al., *3-D Multilateration: A Precision Geodetic Measurement System,* Preliminary Document TM 391-340, July 5, 1972 (JPL internal document).

JPL Quarterly Technical Review Volume 2, Number 3 October 1972

Index: mathematical sciences, mechanics, power sources, solid-state physics, structural engineering

An Algorithm for Synthesizing Mass and Stiffness Matrices From Experimental Vibration Modes

R. G. Ross, Jr.

Engineering Mechanics Division

It is sometimes desirable to derive a dynamic model of highly complex structures from experimental vibration data. This article presents an algorithm for synthesizing the mass and stiffness matrices from experimentally derived modal data in a way that preserves the physical significance of the individual mass and stiffness elements. The mass and stiffness matrices are derived for a rollup solar array example, and are then used to define the modal response of a modified array.

Introduction

Structural design often requires an estimate of the response of a conceived structure to dynamic excitation before the design is finalized. The predicted response is generally obtained using a finite element discretization of the governing differential equations to calculate the matrices $\mathbf{K}$ and $\mathbf{M}$ that characterize the structure's stiffness and mass properties. The solution to the algebraic eigenvalue problem $\mathbf{K}x = \omega^2\mathbf{M}x$ defines the predicted natural frequencies ω and vibration mode shapes of the structure.

To verify the analytical model, the low-order natural frequencies and mode shapes may also be determined experimentally in a modal test. These tests are usually run on the final structure or on a structural simulation of the final structure, often at a time when it is difficult to incorporate anomalies into the design cycle. For this reason, there is a growing desire to incorporate modal test results of early prototypes or skeletal systems into the analytical models of these systems so that extrapolation to final designs can be made with greater confidence.

In addition to space applications as described in this article, one area of current interest is the modal testing of multistory building structures that is conducted after the completion of the primary structure but before the addition of interior walls, trim, and furnishings. It is desired to use the results of preliminary modal tests to improve the analytical model of the primary structure so that extrapolation to the dynamic earthquake response of the finished building can be made by adding the elemental stiffness and mass matrices describing the structural modifications directly to the synthesized matrices.

Several methods for synthesizing the governing mass and stiffness matrices from experimental vibration modes have been recently described (Reference 1). This article describes an improved matrix synthesis technique that is shown to allow elemental stiffness and mass matrices describing structural modifications to be added directly to the synthesized matrices.

Definition of Problem

Following the rationale outlined in Reference 1, the problem is the following: with a set of p eigenvalues λ_i ($\lambda_i = \omega_i^2$) and corresponding eigenvectors ϕ_i (mode shapes) of the unknown structural system, we wish to determine the n^{th} order mass and stiffness matrices so that the eigensystem

$$\mathbf{K}x = \lambda \mathbf{M}x \tag{1}$$

will possess eigenvalues and eigenvectors that are either equal to or as close as possible to the measured ones. Since the most significant characteristics of the mass and stiffness matrices are their representation of the system's kinetic and strain energies (Reference 1), **M** and **K** are further required to accurately represent known kinetic and strain energy characteristics of the system. This is necessary if **M** and **K** are to be compatible with the analytical model of the structure.

To determine the requirements for **M** and **K**, we note that if **M** and **K** are required to be symmetric and to define the measured eigensolution, then the eigenvectors must be orthogonal with respect to them; i.e., if $\mathbf{\Phi}$ is the modal matrix of eigenvectors, then

$$\Phi^T \mathbf{M} \Phi = \mathbf{D} \quad \text{and} \quad \Phi^T \mathbf{K} \Phi = \Lambda \mathbf{D} \tag{2}$$

where **D** is an arbitrary diagonal matrix and Λ is a diagonal matrix of the λ_i. If we temporarily assume that n eigenvectors are available so that $\mathbf{\Phi}$ is nonsingular, then Equation 2 requires

$$\mathbf{M} = {\Phi^{-1}}^T \mathbf{D} \Phi^{-1} \tag{3}$$

and

$$\mathbf{K} = {\Phi^{-1}}^T \mathbf{D} \Lambda \Phi^{-1}$$

However, because the number of coordinates used is assumed to be much larger than the number p of natural modes determined, only the first p out of n eigenvectors are available, and the inverse of the modal matrix is not defined. To alleviate the problem, we consider the inverse matrices

$$\begin{aligned} M^{-1} &= \Phi D^{-1} \Phi^T \\ K^{-1} &= \Phi \Lambda^{-1} D^{-1} \Phi^T \end{aligned} \tag{4}$$

which are singular, rank p matrices when only p modes are available. Since ultimately **M** and **K** are required, the inversion of these rank deficient matrices will be necessary. However, first consider the problem of determining the diagonal normalization matrix **D** so as to preserve as much as possible the known kinetic and strain energy characteristics.

Determination of the Normalization Matrix D

In most cases, knowledge of the system energies is limited to that represented by the analytical mass and stiffness matrices. Allowing for other known energy characteristics, $\tilde{\mathbf{M}}$ is defined as the approximate mass matrix that represents knowledge of the system kinetic energy, and similarly $\tilde{\mathbf{K}}$ is defined as the approximate stiffness matrix that represents knowledge of the system strain energy.

Recalling that the strain and kinetic energies associated with an arbitrary displacement q_i or velocity distribution v_i are given by $1/2 q_i^T \mathbf{K} q_i$ and $1/2 v_i^T \mathbf{M} v_i$, respectively, the normalization **D** can be defined by requiring that

$$v_i^T M v_i = v_i^T \tilde{M} v_i \tag{5}$$

and

$$q_i^T K q_i = q_i^T \tilde{K} q_i \tag{6}$$

for a total of p arbitrary vectors q_i and v_i. If more than p important energy relationships exist, **D** can be alternatively defined by requiring that Equations 5 and 6 be satisfied in the least squares sense.

To preserve the important energies defined by **M** and **K**, the arbitrary vectors should be chosen as meaningful displacement and velocity distributions for the structural system under examination. Though the optimum vectors will depend on the specific characteristics of $\tilde{\mathbf{K}}$ and $\tilde{\mathbf{M}}$, a logical choice for most problems can be made by noting that **M** will approximate the kinetic energies of the low-order modes reasonably well; i.e., $\phi_i^T \mathbf{M} \phi_i$ is well described by $\phi_i^T \widetilde{\mathbf{M}} \phi_i$ for low-order ϕ_i. For such problems, the measured ϕ_i are therefore a logical choice for the arbitrary vectors. With this selection, and the use of Equation 3 for **M**, the p d_i are defined by

$$d_i = \phi_i^T \widetilde{\mathrm{M}} \phi_i \; [i = 1, p] \tag{7}$$

Similarly, if a measured mode ϕ_i is used as a q_i, the i^{th} diagonal element is defined by

$$d_i = (\phi_i^T \widetilde{\mathrm{K}} \phi_i) / \lambda_i \tag{8}$$

Inversion of the Rank Deficient Inverse Matrices

If the number p of vibration modes determined is equal to the number of measured coordinates n, then Equations 4, and 7 and/or 8 define nonsingular inverse mass and stiffness matrices that, when inverted, define the measured frequencies and mode shapes exactly. When p is less than n, the inverse matrices are singular, rank p, and Equations 7 and 8 generally only approximate the equalities defined by Equations 5 and 6.

In Reference 1 it was suggested that Equations 4 could be made invertable by filling out the modal matrix with n-p arbitrary linearly independent vectors. Though these vectors will be eigenvectors of the resulting eigensystem, choosing larger λ_i for them will make them higher order modes out of the range of interest. The advantage of this approach is that the resulting mass and stiffness matrices define the measured frequencies and mode shapes exactly, and Equations 5 and 6 are satisfied exactly for a total of n vectors. The disadvantage of this technique is the difficulty sometimes encountered in choosing linearly independent vectors to fill out Φ that are not nearly dependent on the measured mode shapes, and that do not lead to ill-conditioned mass and stiffness matrices.

An alternate inversion approach, which is considered here, is a modified spectral inversion of the rank difficient inverse mass and stiffness matrices. Recall that these symmetric matrices can be described in terms of their spectral decompositions (eigenvalues and eigenvectors) as follows

$$\mathrm{M}^{-1} = \sum_{i=1}^{n} \beta_i \xi_i \xi_i^T = \mathrm{XBX}^T \tag{9}$$

and

$$K^{-1} = \sum_{i=1}^{n} \alpha_i \zeta_i \zeta_i^T = ZAZ^T \tag{10}$$

where

β_i = i^{th} eigenvalue of M^{-1} (ordered smallest to largest)

ξ_i = i^{th} eigenvector of M^{-1}(normalized $\xi_i^T \xi_i = 1$)

α_i = i^{th} eigenvalue of K^{-1} (ordered smallest to largest)

ζ_i = i^{th} eigenvector of K^{-1} (normalized $\zeta_i^T \zeta_i = 1$)

$\mathbf{B}$ = diagonal matrix of β_i

$\mathbf{X}$ = modal matrix of ξ_i

$\mathbf{A}$ = diagonal matrix of α_i

$\mathbf{Z}$ = modal matrix of ζ_i

Since the eigenvectors of symmetric matrices are orthonormal, $\mathbf{X}^T = \mathbf{X}^{-1}$, $\mathbf{Z}^T = \mathbf{Z}^{-1}$ and thus

$$M = XB^{-1}X^T \tag{11}$$

and

$$K = ZA^{-1}Z^T \tag{12}$$

However, because $\mathbf{K}^{-1}$ and $\mathbf{M}^{-1}$ are rank p, $\alpha_i = 0$ and $\beta_i = 0$ $[i = 1, n - p]$ and $\mathbf{A}^{-1}$ and $\mathbf{B}^{-1}$ are undefined. This is overcome by requiring

$$\xi_i^T M \xi_i = \xi_i^T \widetilde{M} \xi_i \; [i = 1, n - p]$$

and

$$\zeta_i^T K \zeta_i = \zeta_i^T \widetilde{K} \zeta_i \; [i = 1, n - p]$$

Substituting into Equations 11 and 12 gives

$$\alpha_i^{-1} = \zeta_i^T \widetilde{K} \zeta_i \; [i = 1, n - p] \tag{13}$$

$$\beta_i^{-1} = \xi_i^T \tilde{M} \xi_i \; [i = 1, n - p] \tag{14}$$

Using $\alpha_i^{-1} = 1/\alpha_i$ and $\beta_i^{-1} = 1/\beta_i$ for $i = n - p + 1, n$ in conjunction with Equations 13 and 14 completely defines $\mathbf{A}^{-1}$ and $\mathbf{B}^{-1}$.

The complete algorithm for synthesizing the mass and stiffness matrices from experimental modal data is defined by Equations 4, 7 and/or 8, 11, 12, 13, and 14.

Example—Application to Rollup Solar Array

As a demonstration, the matrix synthesis technique just described is used to synthesize the mass and stiffness matrices for the rollup solar array shown in Figure 1. The array consists of two solar-cell blankets tensioned between the base and a relatively stiff leading edge beam that is attached to the tip of the deployed boom (Reference 2). For the purposes of this example, the out-of-plane dynamic behavior of the array is described by the seven-degree-of-freedom model in Figure 2. The parameter values associated with the array are given in Table 1. Note that the actual array is assumed to have unequal blanket tensions on the two sides and an uneven mass distribution. The first few eigenvalues (natural frequencies squared) and mode shapes defined by this model will be used as the "experimentally determined modal data" and are given in Table 2.

The idealized equal tension uniform mass values in Table 1 are assumed in the approximate analytical model that defines $\tilde{\mathbf{K}}$ and $\tilde{\mathbf{M}}$. For comparison, the eigenvalues and mode shapes defined by $\tilde{\mathbf{K}}$ and $\tilde{\mathbf{M}}$ are given in Table 2. Note that this "approximate" model leads to a pair of equal eigenvalue pure blanket resonances in addition to the pure symmetric and antisymmetric

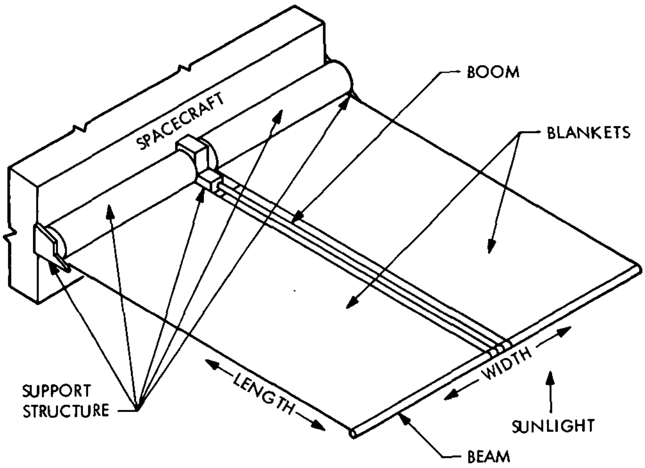

Figure 1. Deployed array

Table 1. Solar array parameter values

Parameter	Units	Actual array	Approximate model
Length	m	1.22	1.22
Width	m	0.61	0.61
Boom mass	kg	0.56	0.54
Boom bending stiffness (EI)	Nm^2	18.6	16.5
Boom torsional stiffness (GJ)	Nm^2	0.	0.
Leading edge beam mass	kg	0.41	0.45
Boom tip mass	kg	0.04	0.0
Blanket mass:			
Outer half left side	kg	0.95	0.91
Inner half left side	kg	0.86	0.91
Outer half right side	kg	0.95	0.91
Inner half right side	kg	0.86	0.91
Blanket tension:			
Left side	N	9.3	8.9
Right side	N	7.1	8.9

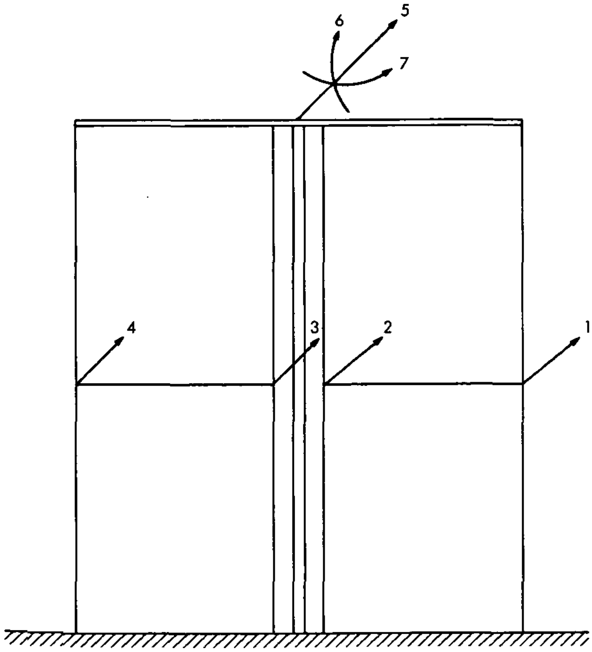

Figure 2. Finite element model of array

Table 2. Eigensolutions for example array

"Measured" eigensolution of actual array						
0.787+01	0.137+02	0.392+02	0.493+02	0.758+02	0.924+02	0.801+04
1	2	3	4	5	6	7
0.504	0.414	0.589	−0.228	0.660	−0.157	0.018
0.002	0.455	−0.797	−0.084	0.237	0.184	0.018
0.002	0.388	0.045	0.785	0.408	0.272	0.018
−0.462	0.423	0.123	−0.567	−0.319	0.777	0.018
0.003	0.503	0.015	0.029	−0.236	−0.240	−0.075
0.001	0.192	0.006	0.011	−0.088	−0.089	−0.996
0.730	−0.045	−0.026	0.050	−0.421	0.445	0.000
Eigensolution from approximate model						
0.811+01	0.121+02	0.483+02	0.483+02	0.878+02	0.885+02	0.720+04
1	2	3	4	5	6	7
−0.479	−0.407	0.130	−0.587	0.455	−0.603	0.018
−0.000	−0.407	0.094	0.789	0.455	−0.000	0.018
−0.000	−0.407	−0.801	−0.021	0.455	−0.000	0.018
0.479	−0.407	0.577	−0.182	0.455	0.603	0.018
−0.000	−0.542	0.000	−0.000	−0.389	0.000	−0.072
−0.000	−0.208	0.000	−0.000	−0.145	0.000	−0.997
−0.735	0.000	−0.000	−0.000	0.000	0.523	−0.000
Eigensolution from synthesized model						
0.787+01	0.137+02	0.392+02	0.493+02	0.537+02	0.881+03	0.121+04
1	2	3	4	5	6	7
0.504	0.414	−0.589	0.228	0.506	0.189	0.012
0.002	0.455	0.797	0.084	0.331	0.055	0.006
0.002	0.388	−0.045	−0.785	−0.013	−0.352	−0.010
−0.462	0.423	−0.123	0.567	−0.344	−0.590	−0.020
0.003	0.503	−0.015	−0.029	−0.387	0.457	−0.350
0.001	0.192	−0.006	−0.011	−0.212	0.158	0.936
0.730	−0.045	0.026	−0.050	−0.567	−0.505	−0.022

[a] The eigenvalues are listed horizontally using scientific notation and the eigenvectors are listed vertically beneath them.

structural modes. These are different from the modes of the "actual" array as given in Table 2.

The problem is to synthesize new mass and stiffness matrices that better approximate the assumed "measured" modal data, and that remain compatible with the finite element analysis used to define the approximate model. Using the previously derived algorithm in conjunction with the first four measured modes ($p = 4$) gives new matrices for the structure. The eigenvalues and mode shapes defined by these synthesized mass and stiffness matrices are given in Table 2, and compare quite favorably with the "measured" modal data.

To demonstrate the compatibility with the approximate finite element model, the effect of assuming a 1.36 Nm/rad (1 ft-lb/rad) torsional stiffness for the boom and adding a 0.45 kg (1 lb) lumped mass to the tip of boom is considered. Adding the appropriate mass and stiffness terms to the "actual," approximate, and synthesized matrices leads to the modified eigenvalues and mode shapes given in Table 3. From these results, it is clear that the

Table 3. Eigensolutions for modified array

"Measured" eigensolution of modified array

0.116+02	0.240+02	0.392+02	0.495+02	0.702+02	0.117+03	0.782+04
1	2	3	4	5	6	7
0.443	0.707	−0.552	−0.199	0.533	−0.400	0.013
0.435	−0.049	0.820	−0.071	0.336	0.022	0.013
0.383	−0.033	−0.052	0.757	0.636	0.029	0.013
0.377	−0.548	−0.138	−0.616	0.264	0.591	0.013
0.534	−0.029	−0.017	0.025	−0.294	−0.036	−0.054
0.204	−0.011	−0.006	0.009	−0.110	−0.013	−0.998
0.009	0.442	0.029	0.045	−0.172	0.699	0.000

Eigensolution from modified approximate model

0.101+02	0.246+02	0.483+02	0.483+02	0.752+02	0.117+03	0.704+04
1	2	3	4	5	6	7
0.397	0.619	0.500	−0.316	0.474	−0.524	0.013
0.397	0.000	−0.500	0.632	0.474	−0.000	0.013
0.397	−0.000	−0.500	−0.632	0.474	−0.000	0.013
0.397	−0.619	0.500	0.316	0.474	0.524	0.013
0.568	0.000	0.000	0.000	−0.297	0.000	−0.052
0.218	0.000	0.000	0.000	−0.111	0.000	−0.998
−0.000	0.483	−0.000	−0.000	−0.000	0.671	0.000

Eigensolution from modified synthesized model

0.116+02	0.237+02	0.392+02	0.495+02	0.627+02	0.705+03	0.113+04
1	2	3	4	5	6	7
−0.411	0.733	−0.557	0.188	0.406	0.174	0.076
−0.426	0.048	0.818	0.055	0.228	0.060	0.023
−0.401	−0.092	−0.055	−0.778	−0.120	−0.398	−0.110
−0.415	−0.446	−0.126	0.596	0.146	−0.583	−0.206
−0.525	−0.099	−0.024	−0.001	−0.281	0.374	−0.120
−0.201	−0.056	−0.011	0.004	−0.153	−0.192	0.944
−0.005	0.491	0.012	−0.018	−0.803	−0.539	−0.186

[a] The eigenvalues are listed horizontally using scientific notation and the eigenvectors are listed vertically beneath them.

modified synthesized model provides a much better description of the modified structure than does the modified approximate model. Though the agreement between the modified synthesized and modified exact models is not perfect, it is considered good in light of the size of the error in the starting approximate model and the size of modification that was made.

References

1. Ross, R. G., "Synthesis of Stiffness and Mass Matrices from Experimental Vibration Modes," Paper No. 710787, presented at the Society of Automotive Engineers 1971 National Aeronautics and Space Engineering and Manufacturing Meeting, Los Angeles, California, Sept. 28–30, 1971. To be published in *SAE Transactions*, Vol. 80, Society of Automotive Engineers, Inc., New York.

2. *Final Report, Design and Development of a 30 Watt per Pound, 250 Square Foot Rollup Solar Array*, Document 705D4286. Prepared for the Jet Propulsion Laboratory by Missiles and Space Division, General Electric Co., Philadelphia, Pennsylvania, Dec. 1, 1970.

JPL Quarterly Technical Review Volume 2, Number 3 October 1972

Index: fluid mechanics, power sources

Xenon-Filled Silicon Germanium Thermoelectric Generators

F. de Winter

Guidance and Control Division

An analysis is presented that shows the desirability and feasibility of using a xenon fill in the initial stages of operation of a silicon-germanium radioisotope thermoelectric generator (RTG) to be used in outer-planetary exploration. The xenon cover gas offers protection against oxidation and against material sublimation, and allows the generator to deliver required power throughout the prelaunch and launch phases. The protective mechanisms afforded by the xenon cover gas and the mechanization of a xenon supply system are also discussed.

Introduction

The spacecraft studied at JPL for outer-planetary exploration is powered by a radioisotope thermoelectric generator (RTG) system of about 450 W at beginning of life (BOL). This is to be supplied by silicon-germanium thermoelectric generators that will eventually be exhausted to the vacuum of space, either by command or through leaks, during transplanetary flight.

During the prelaunch and launch phases, the spacecraft requires approximately 250 W of electrical power. Even if no power were required from the RTGs, the isotope capsules will supply heat that must be removed in a manner that maintains the oxidation-prone materials at acceptable temperatures, or isolates these materials from oxygen. If a high degree of confidence existed that a completely leakproof RTG could be manufactured, the generator could simply be evacuated to 10^{-6} or 10^{-7} torr and vented in space after launch with the knowledge that no oxygen could have entered during the launch and prelaunch phases. In the absence of such confidence it is possible to utilize a generator filled with some inert atmosphere at a pressure higher than atmospheric. This would then produce a sweeping diffusion barrier in any leakage hole, to keep oxygen out of the system. If the right gas were selected, the generators could supply enough power to meet the requirements of the launch and prelaunch phase as well as protect components from degradation.

A number of questions must be answered to understand the use of such a gas:

1. What is the optimum gas to use and why?
2. How does the gas affect RTG operation on the launch pad?
3. How effective might the gas really be in keeping oxygen out?
4. What is there to be gained by keeping inert gas in the RTGs during part of the mission?
5. How is the whole process mechanized?

Gas Selection

For maximum power a gas of low thermal conductivity is required; for minimum gas leakage, low molecular velocities; and for low oxygen back-diffusion, low diffusion coefficients. These requirements are satisfied simultaneously if a gas with a high molecular weight is selected. The most desirable inert gas is obviously xenon, with an average molecular weight of 131.3. Krypton, with a molecular weight of 83.8, is not quite as good; radon is unstable.

Prelaunch Power

It has been shown that xenon, the most desirable gas, allows the RTG to produce more than the 250 W necessary for this phase of the mission. The remainder of this article deals with the last three questions.

Oxygen Flow into a Generator Filled with Xenon

It is highly desirable to exclude oxygen from the RTG during the launch and prelaunch phases. To avoid oxygen inflow, the RTG is to be pressurized at above atmospheric pressure with xenon. This gas will then flow out of any leakage holes. Oxygen can enter the RTG only by a countercurrent diffusion process.

The countercurrent diffusion process depends on leakage hole size and configuration. Since a leakage hole is an unplanned entity, the configuration is quite arbitrary, and a shape must be chosen to enable analysis of the governing factors.

An analysis was made of this countercurrent diffusion process using cylindrical (circular) holes. The process governing the flow of xenon was considered to be either in the free molecular flow regime or in the continuum (nonslip) fully developed laminar flow condition. The countercurrent diffusion of oxygen was then analyzed, and it was found possible to obtain solutions quite similar to the Matricon exponential equation governing diffusion pump operation.

The analytical development is quite straightforward but rather lengthy, and is fully described in Reference 1. The results can be explained with the following set of figures, which apply to an RTG pressurized with 2 atm of xenon surrounded by 1 atm of air and with leakage holes of various diameters and 5-mm length.

Figure 1 shows the outflow of xenon from the generator as a function of hole diameter. Figure 2 shows the inflow of oxygen that would be obtained if the generator were evacuated, also as a function of diameter. Figure 3 shows the "sweep factor," i.e., the factor by which flow values of Figure 2 have to be reduced by virtue of having a countercurrent diffusion rather than an unimpeded flow situation. In the viscous flow regime the sweeping of the oxygen by the xenon is exceedingly effective; in the free molecular flow regime it is — quite expectably — not. Figure 4 shows a leakage hole spectrum that was postulated quite arbitrarily. Figure 5 shows the resultant xenon leakage, a combination of Figures 1 and 4. The integrated value of leakage resulting from the postulated hole spectrum is approximately equal to preliminary leakage specifications of the MHW-RTG. Figure 6 shows the oxygen inflow that would have occurred without the xenon, and that which is obtained with the xenon sweeping.

In this specific example the xenon is only about 70% effective in excluding the oxygen. In practice, the effectiveness will depend on the distribution of hole sizes. If a xenon fill is to be depended upon to prevent oxygen inflow into the generator, then it appears essential to investigate the leakage hole diameter spectrum involved.

Diffusion Suppression to be Expected Through the Use of Modest Xenon Pressures in the RTG

In a test performed at JPL (Reference 2) it appeared that sublimation of SiGe in an evacuated generator was approximately at free sublimation rates.

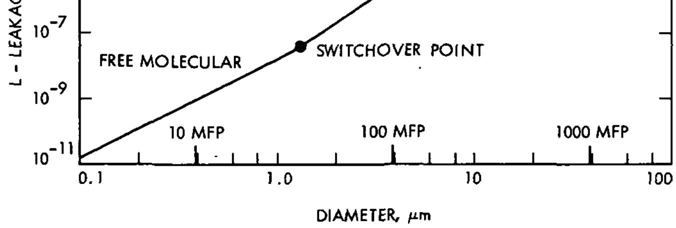

Figure 1. Xenon leakage vs hole diameter

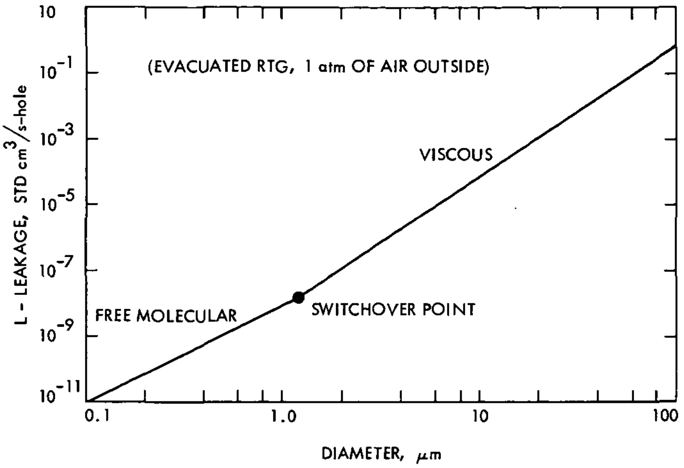

Figure 2. Oxygen in-leakage vs hole diameter

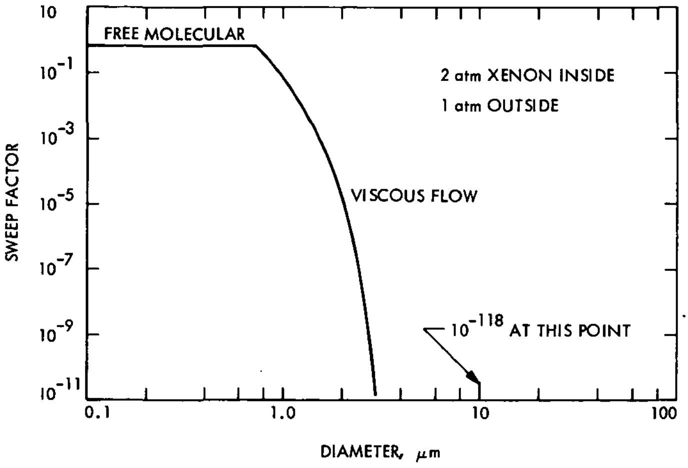

Figure 3. Sweep factor vs hole diameter

It is of interest to determine the extent to which sublimation can be reduced under modest xenon pressures, since it might be feasible to provide modest xenon pressures for extended periods (in the absence of meteoroid damage). The gas-filled incandescent lamp (invented by Langmuir) depends on this mechanism. Low pressure xenon atmospheres might offer sublimation protection without lowering power output excessively. Some lowering of power at BOL might be beneficial since there is an excess of power available, and since a lowering of the hot-side temperature at BOL will result in longer life.

Any xenon baffling effect will work by increasing the pressure of the subliming species next to the solid in question, and by blanketing the solid

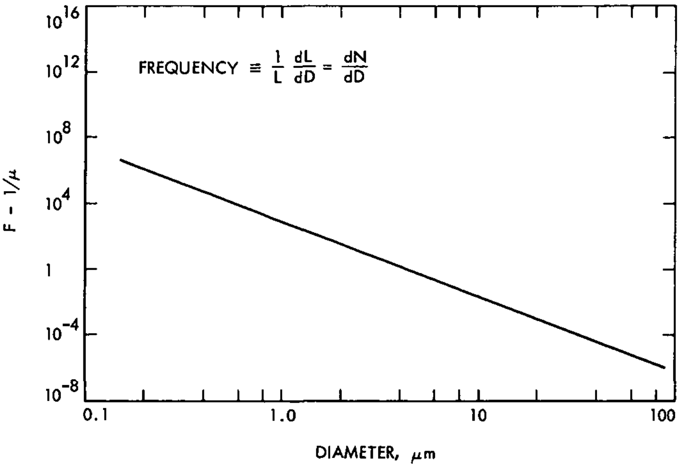

Figure 4. "Frequency" vs hole diameter postulated for example

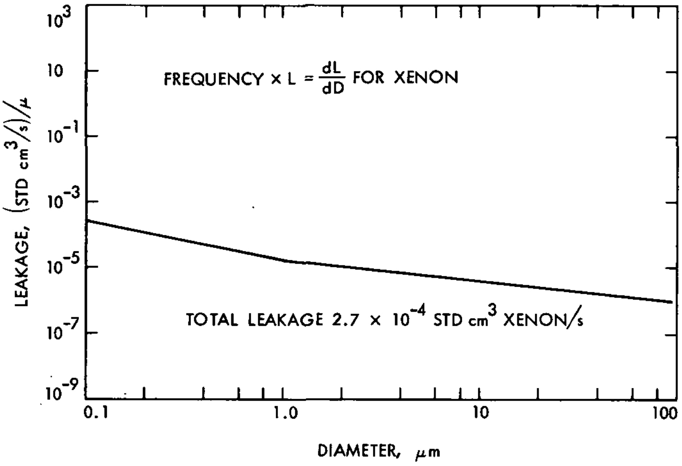

Figure 5. Leakage plot for xenon

with a gaseous diffusion layer that produces a resistance to flow. To estimate the effectiveness of the gaseous diffusion layer requires the determination of the effective thickness of this layer. Two ways of estimating this film thickness are discussed in the next two subsections.

Condensation as a Means of Determining Gradients (Nonreacting Insulation)

From the hot shoe to the cold side of the generator a temperature drop of about 20°C is encountered in the region of interest. If supersaturation is ruled out, this will establish an exponential pressure profile that leads to an effective film thickness of roughly 1.5 mm. If the insulation pore size is large

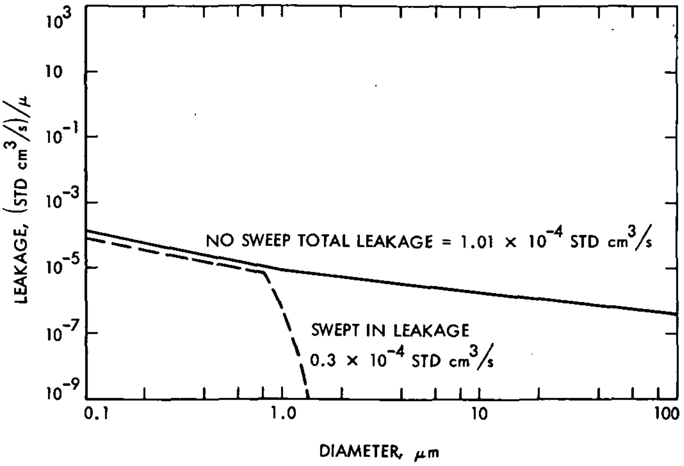

Figure 6. Leakage plot for oxygen

compared to the mean free path of the subliming gas species in the xenon gas, and if the insulation density is very low and the tortuousity in the insulation system is low, then gas diffusivities can probably be safely used to describe the vapor transport. Otherwise a gas flow "conductivity" must be determined for the fibrous insulation.

Reaction with Insulation as a Means of Establishing Gradients

If there is SiO_2 insulation close to the couple, it can take Si vapors and convert them to SiO vapors, which can diffuse away. Only a given amount of insulation can be permitted to corrode away and still have a viable RTG. Probably the film thickness of 1.5 mm determined earlier is a good estimate to use from the "sink" point of view also.

Baffling Effect of Xenon Layer of Effective Thickness *t*

If a subliming material is surrounded by a gas blanket of thickness t through which the species must diffuse, the subliming gas species will assume a pressure at the solid surface somewhere between the equilibrium (saturation) pressure and zero pressure. The rate of diffusion away from the solid (through the gas layer) will be

$$S_d = \frac{D}{t}(P_{act} - 0) \tag{1}$$

where D is the diffusion coefficient of the Si vapor in xenon, t the effective thickness of the gas layer, and P_{act} is the pressure established at the solid/ vapor interface.

A material that has a saturation pressure P_{sat}, and is surrounded by a pressure P_{act} of its own species will have a sublimation rate (if we assume a sublimation coefficient of unity) that can be found from Langmuir sublimation with a driving force of $(P_{sat} - P_{act})$.

$$S_\ell = \sqrt{\frac{RT}{2\pi M}}\,(P_{sat} - P_{act}) \tag{2}$$

Equating the mass fluxes S_ℓ and S_d, we get

$$\sqrt{\frac{RT}{2\pi M}}\,(P_{sat} - P_{act}) = \frac{D}{t}\,(P_{act} - 0) \tag{3}$$

Defining as a baffling (sublimation suppression) factor

$$B \equiv \frac{P_{sat}}{P_{sat} - P_{act}} \tag{4}$$

we obtain, by combining Equations 3 and 4

$$B = \frac{t}{D}\sqrt{\frac{RT}{2\pi M}} + 1 \tag{5}$$

Interestingly enough, no pressure terms appear in Equation 5. There is of course a dependence on the *inert gas pressure*, since the diffusivity D is inversely proportional to it. The baffling (sublimation suppression) factor seems, however, unrelated to the sublimation behavior of the solid in question, so long as the inert gas pressure is higher than the solid saturation pressure.

The first term on the right hand side of Equation 5 is a dimensionless number, the ratio of the Langmuir sublimation flux to the diffusion mass flux (using the same driving forces). Perhaps this is a new dimensionless number. It may be of great usefulness in the understanding of the mechanisms of suppression of sublimation in RTGs. There is no question about the value of R, T, or M. The diffusivity D can be calculated. The only thing in the *dimensionless equation that requires judgment is the estimation of the* effective film thickness t. This follows the "stagnant film" concept pioneered by Langmuir, and now widely used in heat and mass transfer.

Sample Calculations

The most important number to obtain is the diffusivity. The Gilliland equation is probably as good a basis as any.

At 1000°C for Ge/Xe, we get $D_{Ge} = 569/P$ with D in cm^2/s, P in torr. At 1000°C for Si/Xe, we get $D_{Si} = 870/P$.

The baffling factors at 1000°C, using the diffusivities shown earlier, and a thickness t of 0.15 cm, are shown in Table 1. For 1100°C and 1200°C the values are quite close to the ones shown.

These estimates are quite encouraging. A charge of 10 torr of xenon may be quite maintainable, provided there are no leaks caused by meteoroid impacts.

There are several reasons why results are not really of interest for the pressures higher than about 10 torr. Xenon leakage increases with system pressure. At higher pressures thermal shorting will come into play significantly, and it is likely that the baffling factors of 10–15 or so that can be obtained at moderate pressures are high enough to make it unnecessary to bring the temperatures down very much. It also seems unwise to depend on *very* high baffling factors. If one made a design, relying totally on an enormous baffling factor, a leak would be catastrophic. It seems more advisable to design so that a leak will lead only to partially compromised mission objectives.

Mechanization Possibilities of Xenon Systems

It is of interest to postulate methods of ensuring a sufficient supply of xenon to the generator when required, and of depleting it when it is no longer necessary.

It is possible to use individual RTGs that are filled with xenon, with no external plumbing. This has several disadvantages:

(1) There is no xenon reserve except the amount that exists due to the xenon compression.

(2) If RTGs are to be exhausted after launch, each RTG requires an explosive valve.

(3) If, because of mishaps in the launch phase a leak develops in an RTG, the limited reserve could be troublesome since the components of the RTG might oxidize.

One can also connect all the RTGs to a common xenon supply line kept at a given pressure. This has a number of advantages:

(1) The xenon reserve can be made as large as required to prevent troubles with small leaks or launch phase mishaps.

Table 1. Predicted sublimation suppression factor at 1000°C for xenon

Materials	P = 1 torr	P = 10 torr	P = 100 torr	P = 1000 torr
Ge/Xe	2.24	13.4	125	1241
Si/Xe	2.3	14	131	1301

(2) Only one set of valves is required to exhaust the RTGs after launch.

(3) It might become practical to operate the RTGs throughout at least the early part of the mission with some xenon inside to minimize sublimation problems of hot RTG materials.

Xenon lends itself well to compact storage and handling. It can be stored close to its critical point, which is at 58 atm, 17°C. A perfect gas compressed to 58 atm would only be 58 times as dense as at standard temperature and pressure (STP). At the critical point xenon is 184 times as dense as at STP, and it is virtually at room temperature (17°C).

A very lightweight tank will suffice to hold xenon at 58 atm. The tanks JPL uses on the Mariner spacecraft for pressurized nitrogen (attitude control) hold 6.25 l at 190 atm and weigh 2 kg. A tank such as this would hold 6.5 kg of xenon (1000 l at STP), evidently an enormous supply. A schematic of a possible piping arrangement is shown in Figure 7. The helium produced by the radioisotope fuel is shown leaving through glass diffusion barriers, impervious to xenon. High pressure and low pressure regulating systems are shown for ground/flight operation.

Except for the last few hours prior to launch, the tank could be recharged as needed. A regulated manifold can be connected to the individual RTGs. Before launch and after launch, this manifold can be regulated at different pressures as needed. If the RTGs are to be evacuated on purpose for operation in space, explosive valves for evacuation can be tied to the common manifold. Probably two valves are required: first a slow one to get rid of most of the xenon slowly enough to avoid damaging the generators, and second a high throughput valve to provide a large vacuum conductance for the complete evacuation.

In conclusion, the design of a xenon supply system can be done in a straightforward way. It should be noted that unlike other gases, neither the

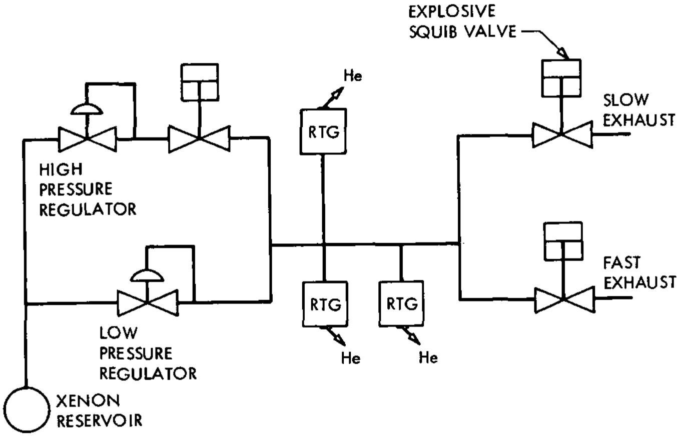

Figure 7. Possible control scheme for xenon supply

xenon weight (6 g/l at STP) nor the cost ($4/l at STP for pure material) is completely negligible.

References

1. de Winter, F., *Use of Protective Xenon Atmospheres in Silicon Germanium Thermoelectric Generators*, Report 900-546 (EM 342-169), Mar. 1972, (JPL internal document).
2. de Winter, F., and G. Stapfer, "Silicon Germanium Technology Program of the Jet Propulsion Laboratory," in *Proceedings of the IECEC*, San Diego, Calif., Sept., 1972.

JPL Quarterly Technical Review Volume 2, Number 3 October 1972

Index: chemistry, nonmetallic materials

Long-Term Aging of Elastomers: Chemorheology of Viton B Fluorocarbon Elastomer

S. H. Kalfayan, R. H. Silver, A. A. Mazzeo, and S. T. Liu

Propulsion Division

Elastomers have extensive aerospace applications. They are used as bladder materials for liquid propellant expulsion systems, propellant binders, and fuel tank sealants for high-speed aircraft. Predicting the long-term behavior of these materials is of primary importance. This article is the continuation of a study to ascertain the nature, extent, and the rate of chemical changes that take place in certain selected elastomers. Under discussion is Viton B, regarded as a temperature and fuel resistant fluorocarbon rubber. The kinetic analysis of the chemical stress relaxation, and infrared and gel permeation chromatography analysis results are discussed.

Introduction

Previously, as part of studies on high-temperature and fuel-resistant elastomers, results of chemical stress relaxation and other measurements for the peroxide vulcanizate of LS 420, a fluorosilicone gum, were reported (Reference 1). Presently, investigations carried out with Viton B are discussed. The fluorocarbon elastomers known under the trade name Viton are copolymers of vinylidene fluoride and perfluoropropylene. Viton B is reported to contain also a third component, tetrafluoroethylene (Reference 2, p. 280). The detailed structure assigned to the polymer as a result of nuclear magnetic resonance studies was as follows (Reference 2, p. 282):

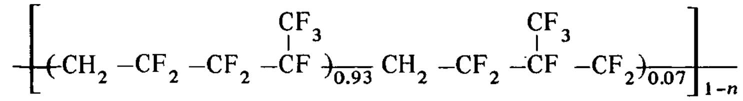

$$-\left[\left(\mathrm{CH_2-CF_2-CF_2-\overset{\overset{\displaystyle CF_3}{|}}{C}F} \right)_{0.93} \mathrm{CH_2-CF_2-\overset{\overset{\displaystyle CF_3}{|}}{C}F-CF_2} \right)_{0.07} \right]_{1-n}-$$

$$-\left[\left(\mathrm{CH_2-CF_2-CH_2-CF_2} \right)_{0.95} \left(\mathrm{CH_2-CF_2-CF_2-CH_2} \right)_{0.05} \right]_{n}-$$

Vulcanization with diamines is the commercial method. In the present study, *N,N*-dicinnamylidene-1,6-hexanediamine (Diak No. 3) was used with magnesium oxide as the acid acceptor. Chemical stress relaxation was the method most extensively used to determine the network changes taking place in the heat-aged Viton fluoroelastomer. Swelling, gel permeation chromatography (GPC), infrared (IR) spectroscopy, and thermogravimetric analyses were also used to obtain supporting information.

IR Studies

Figure 1 shows the IR spectrum of uncured Viton B gum, before and after a thin film of the polymer was heated in air at 300°C. A new peak at 1580 cm^{-1} appeared, which was assigned to conjugated double bonds. Conjugation is likely to be caused by the elimination of HF from the polyvinylidene fluoride block of the Viton B chain, in particular from the head-to-tail portion of the structure. Peaks existing originally at 1710 and 3220 cm^{-1} disappeared. The bond at 1710 cm^{-1} is assigned to carbonyl from the carboxyl group, and the one at 3220 cm^{-1} is assigned to the OH group. It is possible that the carboxyl and hydroxyl groups originally present as end groups in the polymer (Reference 2, p. 282) are eliminated at the elevated temperatures by dehydration and decarboxylation. The peak at 1750 cm^{-1} is assigned to terminal $-CH=CF_2$ groups.

The peaks at 1580 and 1750 cm^{-1} increased in area during the first hour of heating at 300°C, but no changes took place thereafter. Kinetic data could not be obtained from the IR studies.

Gel Permeation Chromatography Studies

Gel permeation chromatography studies of unheated and uncured Viton B gumstock showed a monomodal distribution having an average molecular

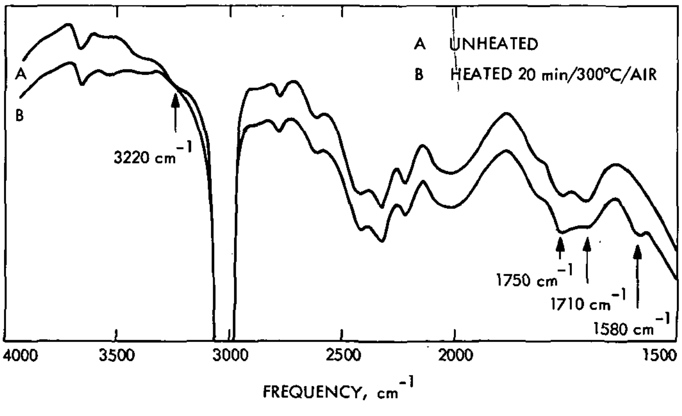

Figure 1. Infrared spectra of Viton B gum

weight, corresponding to the distribution maximum, of 250,000. The gum heated at 325–375°C for three hours gave a molecular weight of 96,000, indicating chain scission. Part of the sample (about 7–10%) could not be dissolved in tetrahydrofuran, showing that crosslinking was taking place, as well.

Swelling Measurements

Three batches of Viton B, molded at 149°C (300°F) for 1 hour with 1, 3, and 4.5% Diak No. 3, were swollen in acetone before and after postcuring 24 hours at 260°C to determine the crosslink density ν_e. Values obtained by using the Flory–Rehner equation along with the interaction constant $\chi_1 = 0.232$ (Reference 3) are shown in Table 1.

The values in the table show that postcuring reduces the number of network chains (crosslink density), and that the ratio of ν_e's of the postcured batches is close to the ratio of Diak No. 3 used, namely, 1:3:4.5%. A more stable network results after postcuring as discussed below.

Stress Relaxation Studies

Stress relaxation measurements on batches 1, 2, and 3 were carried out at temperatures ranging from 150 to 300°C. Experiments were performed in air, nitrogen, and JP-4 aircraft fuel. Samples were about 0.038 cm thick.

The continuous stress relaxation curves obtained in air for batch 3 are shown in Figure 2, where f_t and f_0 are tensile forces at time t and t_0, respectively. Similar curves were obtained for batches 1 and 2 in air and nitrogen.

The data from the chemical stress relaxation experiments were used to calculate energy of activation values (Figure 3) from plots of $-\log t$ (t = time to 30% relaxation) versus $1/T$ (T = temperature in kelvins). Inasmuch as this method for calculating activation energies is strictly applicable for first-order reaction kinetics, the reported activation energies are approximate only. It can be noticed that the activation energies are about the same for runs in air and nitrogen, although chemical relaxation is more rapid in air. This may mean that the mechanism of degradation is the same in air and

Table 1. Crosslink densities from swelling measurements

	ν_e, after molding 1 h at 149°C and aging 1 mo at room temperature		ν_e, after postcuring 24 h at 260°C	
Batch	Moles/g	Moles/m^3	Moles/g	Moles/m^3
1	–	–	4.1×10^{-5}	76.3
2	15.4×10^{-5}	286.4	11.5×10^{-5}	213.9
3	26.2×10^{-5}	487.3	17.4×10^{-5}	323.6

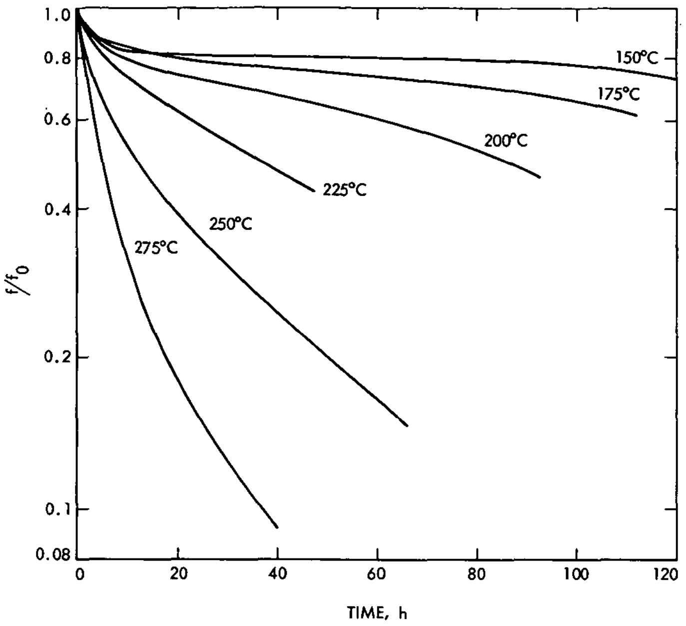

Figure 2. Stress relaxation of Viton B batch 3 in air

nitrogen, and one may suspect that O_2 was not totally excluded from the experiments carried out in nitrogen, although analysis of the effluent nitrogen from the relaxometer gave repeatedly 99.98% N_2 and 0.02% argon by mass spectroscopy. One cannot exclude the possibility of some oxygen combined to the cured polymer, particularly to the amine moiety, which could initiate scission by an oxidative mechanism.

Intermittent relaxation measurements were also performed in air and nitrogen. The continuous and intermittent relaxation curves would be identical if only scission were occurring. If, on the other hand, the stress at a given time in the intermittent experiment is larger than in the continuous experiment, the difference represents the contribution of the crosslinking reaction (Reference 4).

Examination of the curves shown in Figure 4a indicates that Viton B undergoes crosslinking as well as scission during thermal aging in air. Intermittent and continuous stress relaxation experiments conducted in nitrogen at 200°C also show simultaneous crosslinking and scission taking place in an inert atmosphere (Figure 4a). The results from stress relaxation measurements were supported by the thermal aging of uncured Viton B in air, nitrogen, and vacuum (10^{-5} torr). In all three cases the samples darkened, indicating conjugation in the chain, and the aged samples did not dissolve in tetrahydrofuran, as did the original gum.

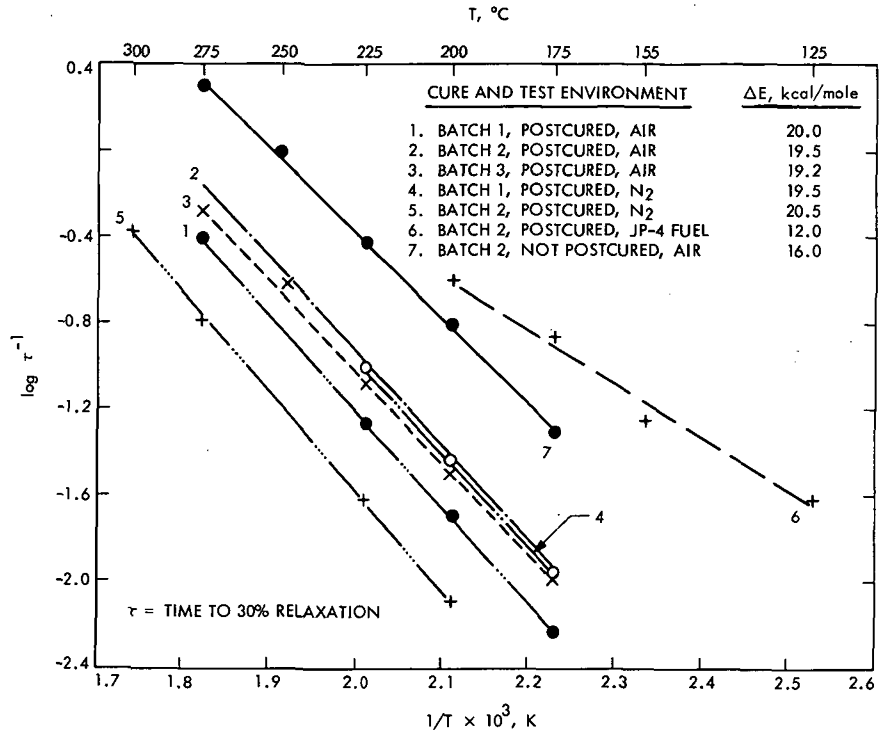

Figure 3. Temperature dependence of (fractional life) obtained from stress relaxation measurements

Plots of ν_e versus time showed that crosslinking of postcured Viton B batches increases initially, and then levels off, in both air and nitrogen. Exceptions were postcured batch 2 tested in air and nitrogen, which showed an initial decrease in the number of crosslinks.

Stress relaxation curves obtained for runs carried out in pure nitrogen lie above those carried out in air (Figure 4a), showing that relaxation due to chemical changes is caused more by atmospheric oxygen than by thermal effects at the experimental conditions used.

When the rate of relaxation is independent of crosslink density, scission at the crosslink is indicated, rather than random scission in the polymer chain (Reference 4). Figure 5 suggests that scission is taking place at the crosslinks in the Diak No. 3 cured Viton B network, at least during the initial period of aging at 275°C. Similar results were obtained at other temperatures.

Although postcuring at 260°C reduces the number of network chains (see Table 1), the rate and extent of stress relaxation of the postcured batches is still less than those cured at lower temperatures. Figure 4b shows that 80%

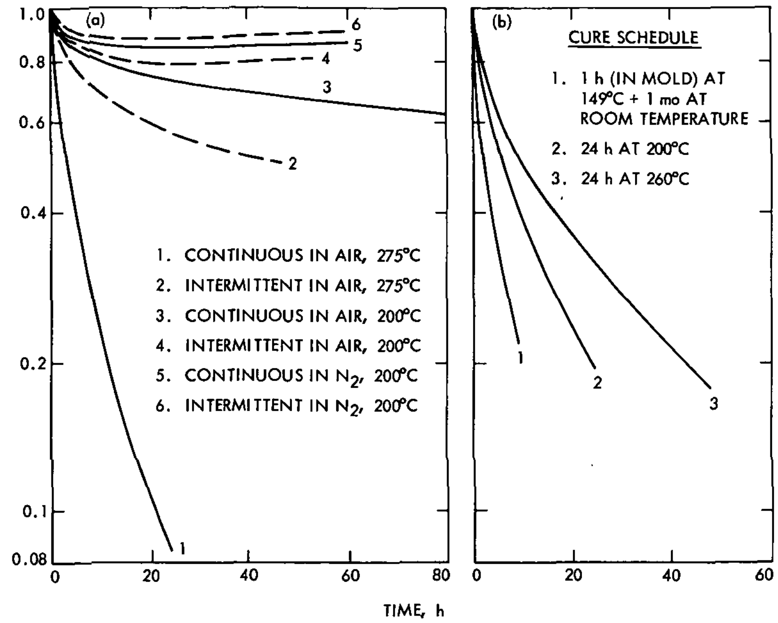

Figure 4. Stress relaxation of Viton B batch 2: (a) intermittent and continuous in air, and N_2; (b) in air at 250°C after various cure schedules

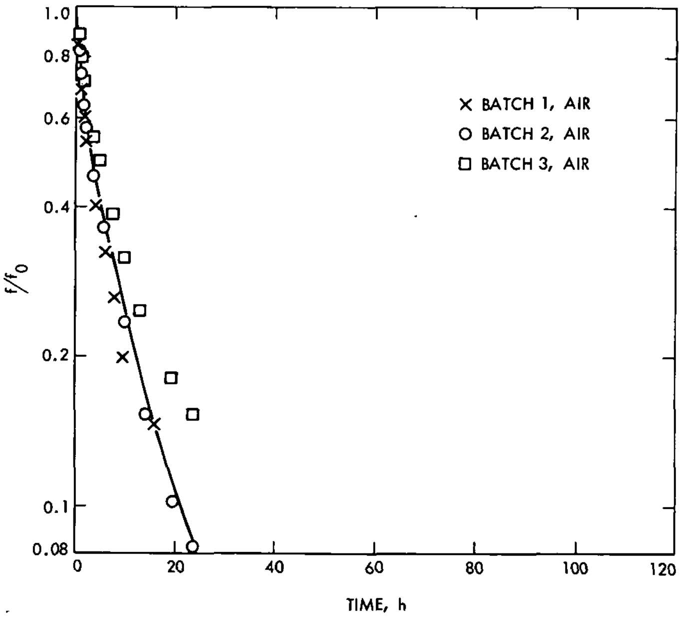

Figure 5. Stress relaxation of Viton B of various crosslink densities in air at 275°C

of the network chains of the unpostcured batches are broken in 24 hours or less. New network chains (crosslinks) are formed on postcuring which are more stable thermally than the original crosslinks. The somewhat higher activation energy found for the postcured batch 2 samples suggests the same contention (Figure 3, compare No. 2 with No. 7).

It has been shown (Reference 5) that diamine cures of Viton occur as follows:

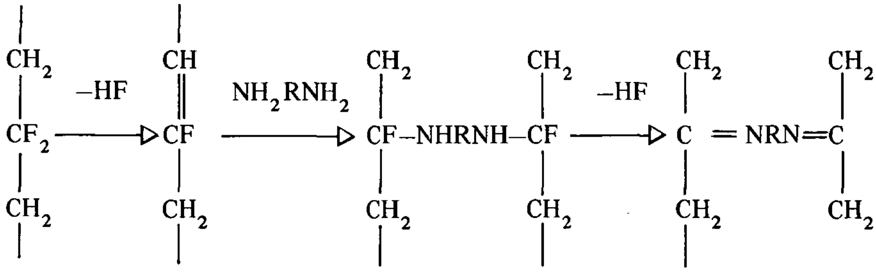

Postcuring probably enhances another type of crosslinking (Reference 6). A conjugated center formed by dehydrofluorination may react with a double bond in an adjacent chain by a Diels-Alder type addition, and subsequently a benzenoid ring forms, which explains the stability of the new network (crosslinks):

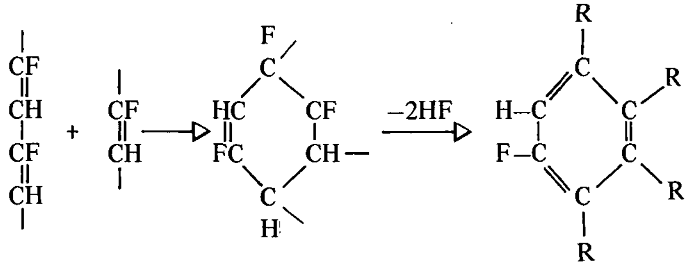

Viton B samples were found to relax faster in JP-4 fuel and gave lower activation energy of degradation than those relaxing in air (Figure 3, No. 6)

Conclusions

The results of these experiments permit the following conclusions:

(1) The fluorocarbon rubber, uncured Viton B gum, loses HF when heated in air, inert atmosphere (N_2), and vacuum to give both conjugated double bonds and random unsaturation.

(2) Scission in the polymer chain predominates when the uncured gum is heated above 325–350°C.

(3) The uncured gum undergoes crosslinking reaction on heating, and the crosslinks are stable below 275–300°C.

(4) The original amine (Diak No. 3) vulcanizate network breaks down almost completely in a day or so at 250°C, but a new more thermally stable network is formed.

(5) Scission in the new network takes place preferably at the crosslinks.

(6) Network breakdown is faster in air, suggesting an oxidative mechanism.

(7) The lower activation energy for the Viton B amine-cured elastomer, as compared to the peroxide-cured LS 420 fluorosilicone (Reference 1), shows a lower stability for this Viton system in air at room conditions. The weak links in the latter are at the crosslink sites. Some other crosslink system, such as that brought about by γ irradiation or peroxides should lead to improved thermal stability in presence of oxygen.

(8) The amine-cured Viton B network is less stable in JP-4 fuel than in air at comparable temperatures.

References

1. Kalfayan, S. H., Mazzeo, A. A., and Silver, R. H., "Long-Term Aging of Elastomers: Chemical Stress Relaxation of Fluorosilicone Rubber and Other Studies," in *JPL Quarterly Technical Review*, Vol. 1, No. 3, pp. 38-47. Jet Propulsion Laboratory, Pasadena, Calif., Oct. 1971.
2. Cooper, J. R., "Fluorine Containing Elastomers," in *Polymer Chemistry of Synthetic Elastomers*, Part 1, pp. 280 and 282. Edited by J. P. Kennedy and E. G. M. Tornquist. Interscience Publishers, Inc., New York, 1968.
3. Flory, P. J., and Rehner, J., Jr., *J. Chem. Phys.*, Vol. 11, p. 521, 1943.
4. Tobolsky, A. V., *Properties and Structure of Polymers*, p. 223. John Wiley & Sons, Inc., New York, 1960.
5. Smith, J. F., and Perkins, C. T., "The Mechanism of Post Cure of Viton A Fluorocarbon Elastomer," *J. Appl. Polym. Sci.*, Vol. 5, p. 460, 1961.
6. Smith, J. F., *Rubber World*, Vol. 142, No. 3, p. 102, 1960.

JPL Quarterly Review Volume 2, Number 3 October 1972

Index: nonmetallic materials, solid-state physics

Extensional Flow of Bulk Polymers

T. J. Peng

Propulsion Division

A study was made of the behavior of polyisobutylene under motion at a constant stretch history for both strip biaxial extensional flow and simple extensional flow. Steady-state non-Newtonian viscosities were observed at various constant stretch histories. Newtonian viscosities for both strip biaxial and simple extensional flow were found to be in agreement with the classical theory.

The results of this study provide an essential part of the experimental background necessary for the development of a new general stress-strain-time relation for uncrosslinked and lightly crosslinked polymers.

Introduction

An experimental investigation of the behavior of uncrosslinked polymers subjected to a constant stretch history has been conducted for both pure shear extensional flow and simple extensional flow.

A standard Instron testing machine, in which crosshead displacement varies linearly with time was modified so that crosshead displacement varies exponentially with time. This change permits testing at constant Hencky strain rate ($\dot{\epsilon} = \dot{\ell}/\ell$), which provides a constant stretch history for both simple extensional flow and strip biaxial extensional flow. This results in a visualization of the steady flow for both types of deformation and enables one to derive the non-Newtonian viscosity from the steady-state region.

It has been shown (Reference 1) previously that in steady-state flow under constant stretch history, the stress functional of a non-Newtonian fluid reduces to a function of the three Rivlin-Ericksen tensors $\underset{\sim}{A}^{(1)}$, $\underset{\sim}{A}^{(2)}$, $\underset{\sim}{A}^{(3)}$, i.e.,

$$\underset{\sim}{\tau} = \underset{\sim}{f}(\underset{\sim}{A}^{(1)}, \underset{\sim}{A}^{(2)}, \underset{\sim}{A}^{(3)}) \tag{1}$$

where $\underset{\sim}{\tau}$ is an extra stress tensor.

Since f is an isotropic tensor function, one may obtain explicit expression for f from the representation theorem of three tensors. By restricting the discussion to slow motion, one may represent the function by a first, second, third, and higher order approximation. In a later report, we will attempt to represent the function by the fourth-order approximation and to determine the material constants from measurement of flow in both extension and strip biaxial extensional flow.

In the present study, the steady-state non-Newtonian viscosities of uncrosslinked polyisobutylene were determined at various constant stretch histories. It was found that for slow strain rates (i.e., the region of Newtonian flow) the viscosity of strip biaxial extensional flow, η_{st}, is equal to 4/3 the simple extensional viscosity, η_E; this result is consistent with the classical theory of Newtonian flow.

Experiment

The test setup is shown schematically in Figure 1. The main part of the setup is a Barber-Coleman Model 7401 "Chronotrol" (c), which is a program controller that uses the meter movement of a Model 401P millivolt input chassis (c). Programming is accomplished by changing the position of the millivoltmeter control set point by means of a slowly rotating disc or cam. The cam is rotated by a motor driven gear train, with the cam follower linked to the control set point through a cable drive. The Chronotrol provides a linear or nonlinear program control from any predetermined time-variable cycle. During any given cam cycle, an appropriate dc voltage is provided from the power supply (f) to the variable crosshead speed control accessory (b) of the Instron tester (a) through a servosystem. The servosystem consists of a reversible motor (d), a polarity reversing relay (g) and two ten-turn potentiometers. Using this setup, the crosshead speed is controlled by the shape of the cam.

Consider a rod-shaped sample of initial length ℓ_0 fixed at one end and extended in the direction of the principal extension. The velocity field v_i of the steady extensional flow is given by

$$v_i = \dot{\epsilon}_i x_i \qquad (i \text{ not summed}) \tag{2}$$

The following relationships for the displacement ℓ and the crosshead speed v can be derived:

$$\ell = \ell_0 e^{\dot{\epsilon} t} \text{ and } v = \dot{\epsilon} \ell_0 e^{\dot{\epsilon} t} \tag{3}$$

The correspondence of actual strain regime to that programmed depends on fluctuation of the motor speed, of the variable crosshead drive accessory, and on the accuracy of the programmed cam. Thus, during the run, the actual displacement of the crosshead as a function of time is continually

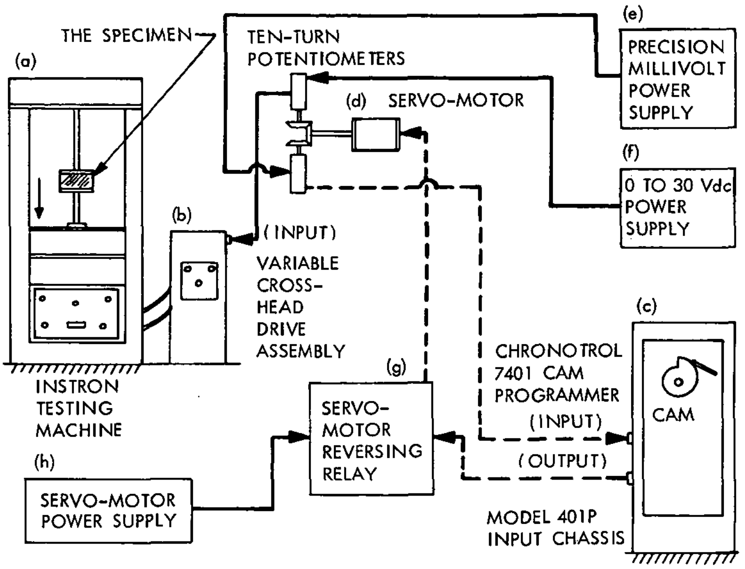

(a) INSTRON FLOOR MODEL TT-D TESTING MACHINE
(b) INSTRON MODEL A-35 VARIABLE SPEED CROSSHEAD DRIVE ACCESSORY
(c) BARBER-COLMAN MODEL 7401 CHRONOTROL WITH A BARBER-COLMAN MODEL 401P MILLIVOLT INPUT CHASSIS
(d) dc SERVO-MOTOR, CONNECTED TO TWO BOURNS TEN-TURN POTENTIOMETERS BY A COMMON SHAFT
(e) ELECTRONIC DEVELOPMENT CORP., PRECISION MILLIVOLT POWER SUPPLY
(f) HEWLETT-PACKARD MODEL 721A POWER SUPPLY
(g) ADVANCE MODEL AM2C115 A.C. RELAY
(h) TRANPAC MODEL SR81 POWER SUPPLY

Figure 1. Schematic diagram of apparatus

compared to that programmed. If there exists any discrepancy, the position of the cam is carefully adjusted to bring them into agreement. The estimated maximum difference between the actual and programmed crosshead displacement is about 1%. Figure 2 illustrates the linearity between $\ln\lambda$ and time for several rates.

Results and Discussion

The material studied was uncrosslinked high molecular weight polyisobutylene (Vistanex L-80, Enjay Chemical Co.). All measurements were carried out at room temperature. Figure 3 shows the relationship of the true stress T_{11} to the stretch ratio λ for simple extensional flow at various strain rates while Figure 4 shows the corresponding behavior for strip biaxial flow. Since the stretch ratio at the constant strain rate $\dot{\epsilon}$ depends on time according to the relation $\lambda = e^{\dot{\epsilon}t}$, Figures 3 and 4 represent the relation of true stress vs time, and show the existence of a steady flow region (i.e., asymptotic region) for both simple and strip biaxial extension flow.

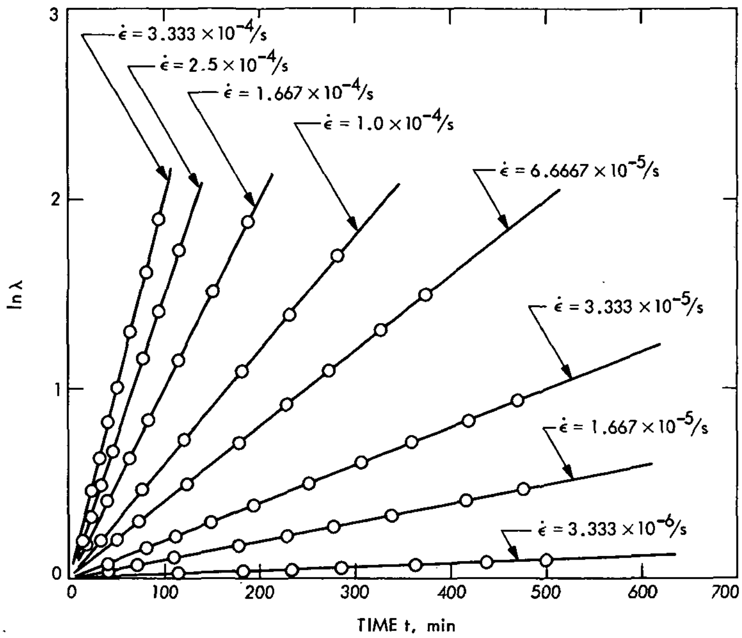

Figure 2. Dependence of lnλ on time for several strain rates

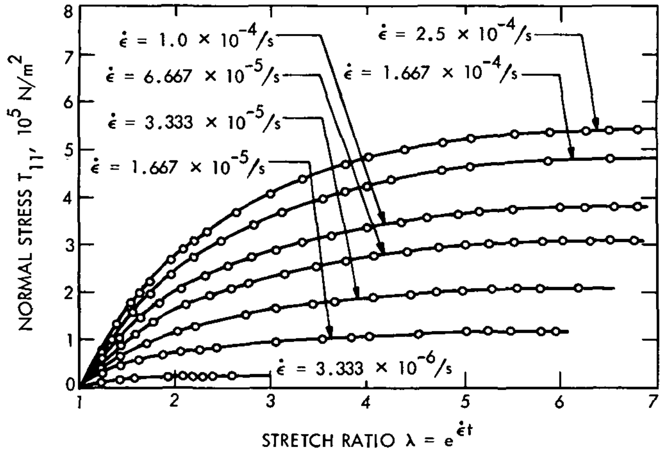

Figure 3. True stress vs total deformation in simple extension for various constant strain rates

The existence of steady flow for simple extension has been reported previously (Reference 2). But this is the first time that steady flow has been experimentally shown for strip biaxial flow.

Figure 5 shows the apparent non-Newtonian viscosity as a function of the normal stress at various strain rates for both simple extensional flow and

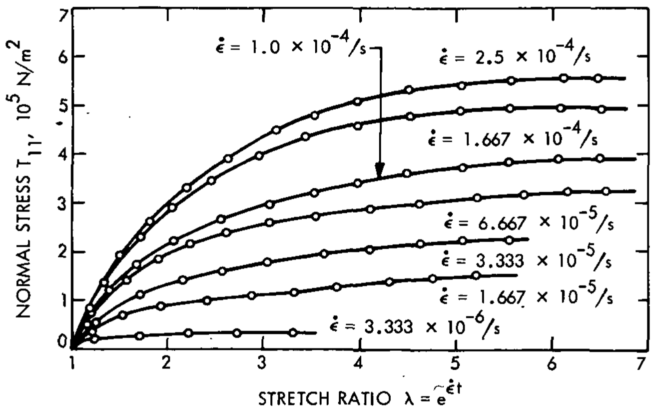

Figure 4. True stress vs total deformation in strip biaxial extension for various constant strain rates

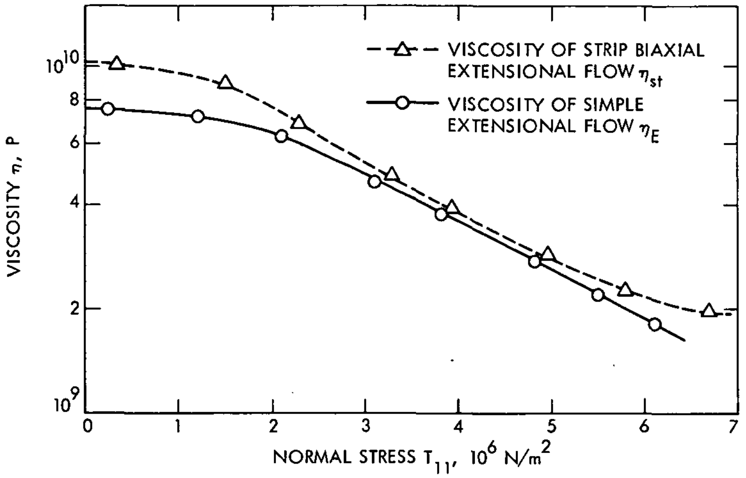

Figure 5. Dependence of simple extension viscosity η_E and strip biaxial extension viscosity η_{st} on the normal stress T_{11}

strip biaxial extensional flow. It shows clearly that the viscosity decreases with increase in the normal stress for both types of test. Figure 6 shows the dependence of the non-Newtonian viscosity on the constant strain rate. It may be seen that the viscosity is a monotonically decreasing function of the strain rate. It is interesting to note that at higher strain rates, the difference between the viscosity in simple extensional flow and in strip biaxial extensional flow decreases.

For the transient region (i.e., the initial parts of the curves in Figures 3 and 4), however, it appears that in contrast to steady-state, the differences between the simple and biaxial case increase at high strain rates. The reason for this behavior is not understood. Perhaps at high $\dot{\epsilon}$ elastic effects

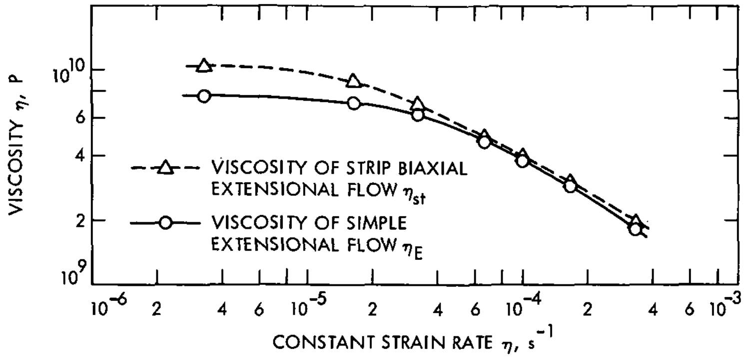

Figure 6. Dependence of simple extension viscosity η_E and strip biaxial viscosity η_{st} on constant strain rate $\dot{\epsilon}$

predominate because of polymer network entanglements. The two modes of deformation for a nonlinear elastic regime have distinctly different characters as shown in studies on finite deformation of highly crosslinked rubberlike materials. On the other hand, in the region of steady flow, the material is liquidlike, and, as expected, exhibits the same character of rectilinear flow for both types of deformation.

In a later report a new model for elastic liquids will be developed to attempt to describe the transient state. This in conjunction with the fourth-order approximation to the steady-state region will aid in obtaining a total picture of the stress-strain-time relation for uncrosslinked and lightly crosslinked polymers for motion with constant stretch history.

Acknowledgment

The author wishes to thank Mr. R. Silver for helping design the apparatus and Mr. C. Solis for his patience in helping with the experiments.

References

1. Wang, C. C., *Arch. Ration. Mech. Anal.*, Vol. 20, No. 23, p. 329, 1965.
2. Ballman, R. L., *Rheologica Acta,* Vol. 4, p. 137, 1965.

JPL Quarterly Technical Review Volume 2, Number 3 October 1972

Index: orbits and trajectories, Pioneer Project

A Summary of the Pioneer 10 Maneuver Strategy

R. B. Frauenholz and J. E. Ball

Mission Analysis Division

The Pioneer Project[1] placed a number of interesting and precise requirements on the navigation of the Pioneer 10 spacecraft flyby mission to Jupiter during 1972–1973. To satisfy these requirements the Pioneer Navigation Team employed a number of versatile computer programs to evaluate the strategies and maneuver sequences required to execute midcourse corrections. This article summarizes the Pioneer 10 mission objectives and the midcourse strategies used to satisfy these *objectives.*

Introduction

Two Pioneer flyby missions to Jupiter during 1972–1975 may have a significant influence on the future exploration of the solar system. These missions will be the first to venture beyond the orbit of Mars, fly through the asteroid belt, and encounter Jupiter, the largest planet in the solar system. If the spacecraft survive the 7-mo journey through the asteroid belt, intense radiation belts at Jupiter may test the spacecraft performance. A hostile environment at Jupiter could influence future missions, either for scientific observation, or for using its gravity to accelerate spacecraft to regions beyond.

The mission objectives are designed to provide scientists with the opportunity to examine the interplanetary region between Earth and Jupiter, in addition to the near-Jupiter environment. The primary mission objectives include exploratory investigations beyond the orbit of Mars, examination of the asteroid belt, and studies of the environmental and atmospheric characteristics of Jupiter (Reference 1). Secondary objectives are to assess the hazards of long duration in interplanetary space and flight through the asteroid belt. Scientific objectives include penetration of the

---

[1] The Pioneer Project is managed for NASA by the Ames Research Center. Jet Propulsion Laboratory responsibilities in the project include preflight navigation analyses and real-time navigation support.

Jupiter radiation belts and provision for good instrument viewing conditions of Jupiter prior to closest approach.

A tertiary objective of the first mission is to attempt spacecraft occultation by Io, a satellite of Jupiter that may possess a tenuous atmosphere. The effects on the radio signals from the spacecraft at entry to, and exit from, occultation will help describe the characteristics of a possible ionosphere, or atmosphere. This objective places the most stringent requirements on the spacecraft navigation to assure both a precise trajectory position and time at Jupiter closest approach.

Pioneer Spacecraft

The two identical Pioneer spacecraft are spin-stabilized and will carry the same experiments. The 256-kg spacecraft, pictured in Figure 1, includes a 29-kg payload for 11 scientific instruments, and 27 kgs of propellant for attitude control and midcourse corrections. The overall length is 2.4 m; its widest dimension is that of the 2.7-m diameter high-gain parabolic dish antenna. Two 2.7-m extendable booms isolate radioisotope thermoelectric generator (RTG) nuclear power sources away from the instrument package. A 6.4-m boom mounts a magnetometer remotely from each RTG and the remainder of the spacecraft.

The liquid hydrazine propulsion system is capable of making velocity changes totaling 200 m/s. Two pairs of thrusters on opposite sides of the antenna dish are used for attitude and velocity changes. For velocity changes, these thrusters operate in either a continuous mode or, when small trims are desired, a pulsed mode. A third pair of thrusters is used for spin rate adjustment.

Two-way communication is provided through the high-gain dish antenna (38 dB) and a medium-gain horn antenna (12 dB). The horn antenna is used near the Earth where two midcourse corrections were scheduled. The high-gain antenna, with a narrow 3-deg beam width, is used after the spacecraft is nearly 47 million km (60 days) from Earth.

The four RTG units, fueled with uranium-238 dioxide, replace the solar panels that have been used on other interplanetary spacecraft for power generation. Solar panels for Pioneer would be prohibitively large, since Jupiter is over 5 AU from the Sun. At launch, the RTGs are expected to produce 160 W of electrical power, at least 134 W at Jupiter, and nearly 120 W 5 yr after launch.

A description of the 11 scientific instruments, and the experiments each will perform, is summarized below. These instruments, shown on the spacecraft in Figure 1, are:

(1) Helium vector magnetometer, to measure magnetic field components along three axes.

(2) Plasma analyzer, to map the solar wind.

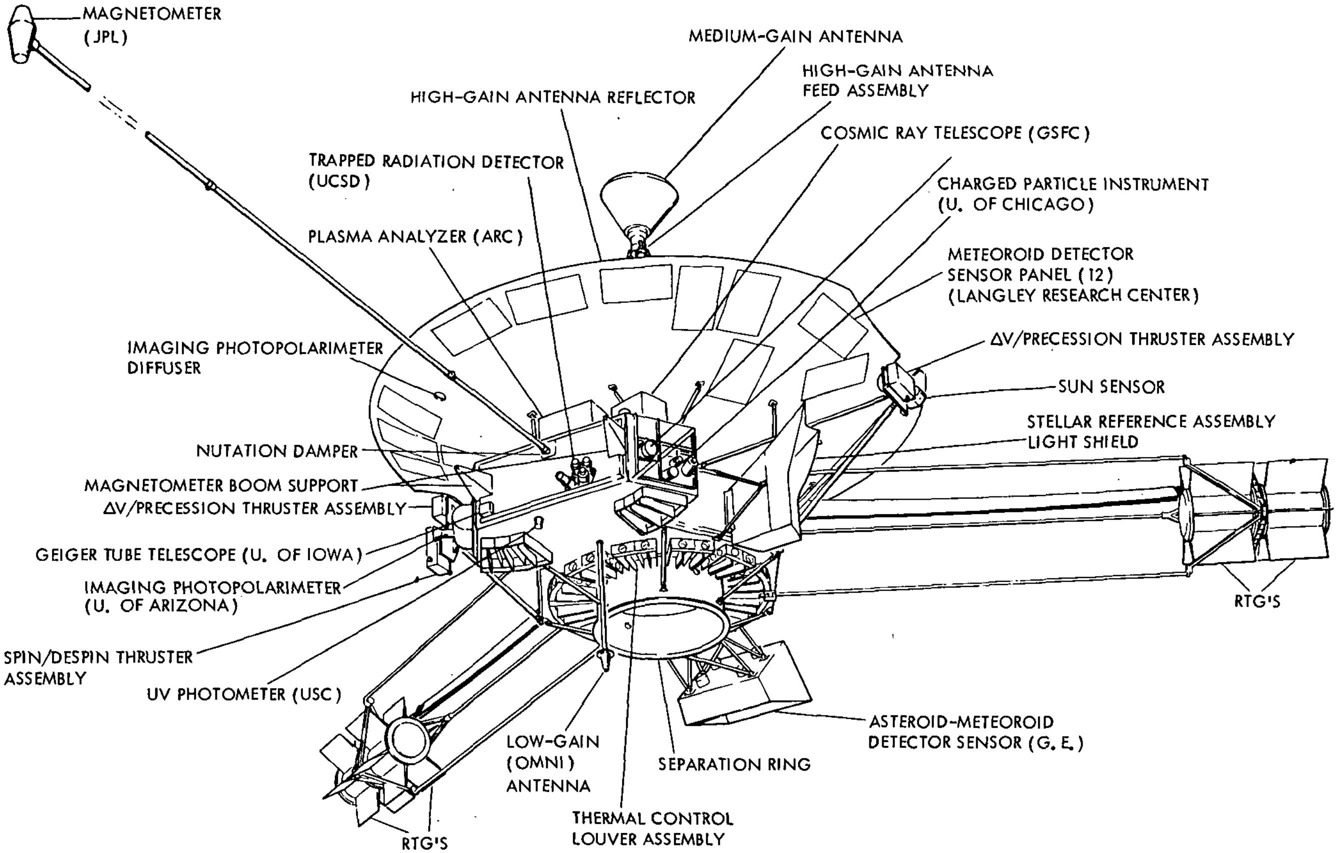

Figure 1. Pioneer spacecraft

(3) Charged-particle detector, to identify 8 of the first 16 elements of the periodic table.

(4) Cosmic ray telescope, to monitor solar and galactic cosmic ray particles.

(5) Geiger tube telescope, to survey electrons and protons in Jupiter's magnetosphere.

(6) Trapped radiation detector, to help correlate trapped particle data with Jovian radio signals.

(7) Asteriod–meteoroid detector, to survey solid material between Earth-orbit and 15 AU.

(8) Meteoroid detector, to detect the distribution in space of particles too small to be seen by light scattering.

(9) Ultraviolet photometer, to determine the ratio of molecular hydrogen to helium in Jupiter's atmosphere and measure the amount of neutral hydrogen in the heliosphere.

(10) Imaging photopolarimeter, to obtain two-color images of light from Jupiter and zodiacal light from interplanetary space.

(11) Infrared radiometer, to measure Jupiter thermal balance, temperature distribution in outer atmosphere, and helium/hydrogen ratio.

Mission Profile

Pioneer F was successfully launched from Cape Kennedy, Florida, at 01:49 GMT, on March 3, 1972, and designated Pioneer 10. The Atlas/Centaur/TE364-4 launch vehicle combination placed the spacecraft in a heliocentric orbit to Jupiter with a direct ascent trajectory. Pioneer 10 is expected to encounter Jupiter with closest approach on December 4, 1973, at 02:26 GMT, after a 640-day, one billion-km journey. An identical Pioneer G spacecraft is scheduled to be launched in April 1973, 8 mo before the Jupiter encounter of Pioneer 10, and is intended to explore a different region about Jupiter.

The nominal Earth-to-Jupiter mission profile, consistent with the primary mission objectives, is shown in Figure 2.

Shortly after closest approach, the spacecraft will pass behind Jupiter, interrupting communications with Earth for about 1 h. Jupiter's gravity will strongly deflect the trajectory and accelerate the spacecraft to a velocity that will permit escape from the solar system. If Pioneer 10 continues to return data until it reaches the present predicted limit of communication with Earth, the spacecraft would be more than halfway between the orbits of Saturn and Uranus. At that point, nearly 8 yr after launch, it will be 2.4 billion km (16 AU) from the Sun. Pioneer will pass the orbit of Uranus (20 AU) with a velocity of 15 km/s relative to the Sun. From this point, it will

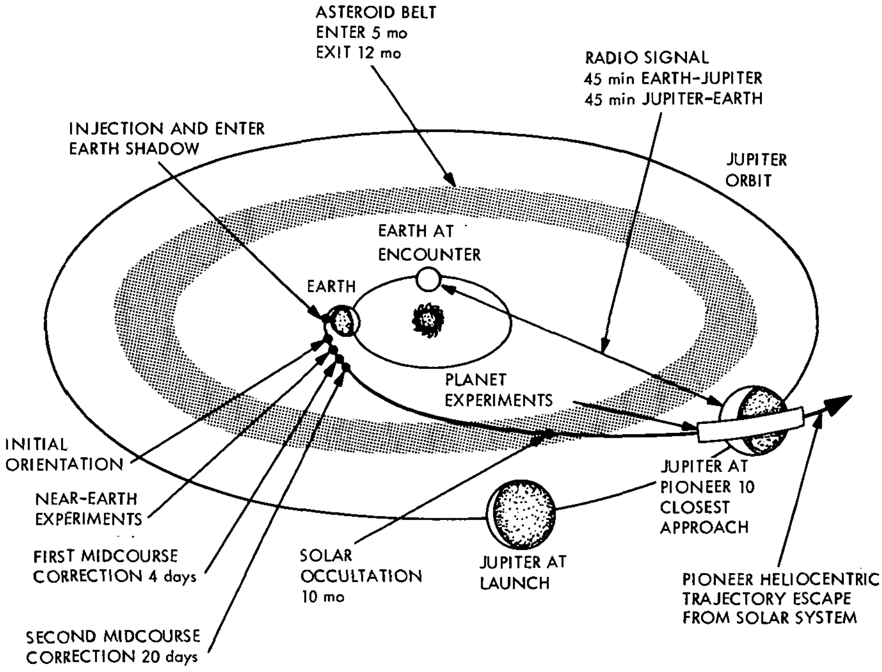

Figure 2. Pioneer 10 mission profile

travel away from the Sun in virtually a straight line, approaching a Sun-relative velocity of 11.5 km/s in the direction of the constellation Taurus. Scientists have placed a pictorial plaque on Pioneer 10 to identify its Earth-origin, should the spacecraft contact another intelligence.

The Pioneer 10 target coordinates at Jupiter were selected to provide arrival conditions best suited for the primary mission objectives, including good instrument viewing conditions prior to closest approach, examination of the radiation belts, and spacecraft occultation by Jupiter. The encounter conditions that satisfy these mission objectives require a closest approach within 3 Jupiter radii of the planet center, and a trajectory plane inclined 14 deg below a parallel to the ecliptic through the planet center. The radius of closest approach consistent with these objectives was to be controlled within ¼ Jupiter radius (Reference 2). There are two secondary navigation requirements. One is to control arrival time within ±½ h of the center of one of the daily 5-h periods when the spacecraft is simultaneously in view of two tracking stations of the Deep Space Network (DSN). The second requirement is for tighter control of closest approach distance (±0.05 Jupiter radii) to control imaging, radiation, and magnetic field survey characteristics near the optimum closest approach of 3 Jupiter radii.

The tertiary objective of spacecraft occultation by the Jupiter satellite, Io requires even tighter control of arrival conditions. The navigation constraints of this objective are discussed later in the article.

Target coordinates at Jupiter were selected to provide an opportunity for achieving each of these objectives. These target coordinates are illustrated in the B-plane hyperbolic encounter coordinate system in Figure 3. For the purposes of evaluating midcourse strategies, the B-plane target coordinates are specified by:

$$\bar{B} \cdot \bar{R} = 209{,}200 \text{ km}$$

$$\bar{B} \cdot \bar{T} = 838{,}900 \text{ km}$$

Time of closest approach (TCA) = December 4, 1973, 02:26 GMT

Pioneer Navigation Team

The Pioneer Navigation Team provides mission analysis support, performs maneuver analyses, determines orbits, evaluates trajectories, and defines navigation alternatives within the constraints and guidelines specified by the Pioneer Project. The Pioneer 10 mission is the first interplanetary mission to require midcourse corrections of a spin-stabilized spacecraft.

The maneuver function of the Pioneer Navigation Team evaluates the spacecraft navigation requirements and identifies maneuver strategies necessary to achieve the mission objectives. A set of computer programs has been developed to aid in this process. The principal program is the Pioneer Maneuver Operations Programming System (PMOPS). This program considers operational constraints, determines a variety of acceptable

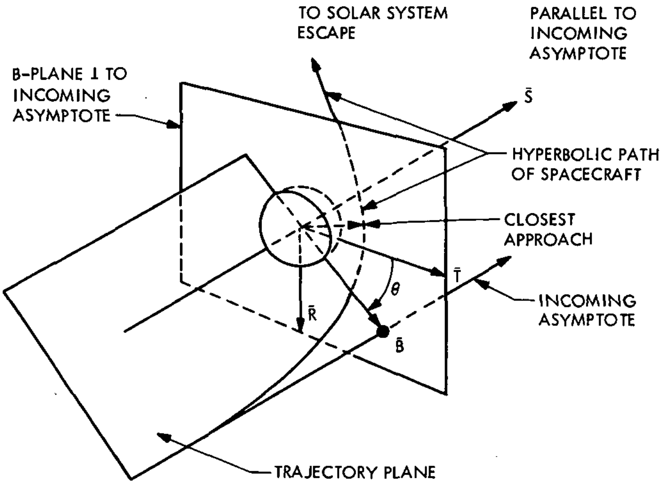

$\bar{B}$ = TARGET PARAMETER
θ = ORIENTATION OF $\bar{B}$
$\bar{S}$ = PARALLEL TO INCOMING ASYMPTOTE
$\bar{T}$ = PARALLEL TO ECLIPTIC PLANE AND ⊥ TO $\bar{S}$
$\bar{R} = \bar{S} \times \bar{T}$

Figure 3. Pioneer hyperbolic encounter coordinate system

maneuver strategies within those constraints, and, after a maneuver is selected, generates command parameters required to maneuver the spacecraft. PMOPS was developed in accordance with the functional and operational requirements set forth in References 3 and 4. An essential input to PMOPS is an accurate estimate of the spacecraft trajectory, provided by the orbit determination function of the Pioneer Navigation Team. Some of the principal Navigation Team analyses prior to launch are reported in References 5 through 8.

Pioneer Maneuver Strategy

The Pioneer spacecraft standard maneuver is achieved by precession of the spin axis to the required direction, followed by the firing of a thruster pair that adds a velocity increment along the spin axis. The spin axis is initially pointed toward the Earth with a nominal spin rate of 4.8 rpm. When performing a precession, a reference direction to the Sun is established by an on-board sensor as the Sun crosses its field-of-view. The spin axis is then precessed to the desired pointing direction by pulsing coupled precession thrusters at a fixed time increment after the Sun crosses the sensor field-of-view. The spin axis is thus stepped in small increments in a direction fixed relative to that of the Sun. The spacecraft thruster pairs can provide velocity changes in either direction along the spin axis. This capability requires turns of no more than 90 deg from Earth-alignment.

The maneuver parameters that specify the Pioneer precession sequence are the geometric rhumb angle, α, and the precession magnitude, ψ. As used in Pioneer navigation terminology, the geometric rhumb angle is the angle between the Sun's projection onto a plane perpendicular to the spin axis and the desired precession direction. The precession magnitude is the total arc length traversed by the spin axis during the rhumb-line precession. The geometric rhumb angle and the precession magnitude are illustrated in Figure 4.

A Pioneer maneuver is subject to execution errors. These errors are modelled as a combination of pointing and velocity magnitude errors. The pointing error has components that are a function of initial pointing accuracy, quantization, and systematic and random errors. The pointing errors are a strong function of the precession magnitude and comprise the dominant maneuver execution error. The velocity magnitude error has both proportional and fixed characteristics. The proportional error is a function of the velocity magnitude, and the fixed error is a function of the thruster shutoff characteristics. The velocity thrusters operate in either a continuous or pulse mode. The pulse mode operation provides much more accurate shutoff characteristics than the continuous mode. The pulse mode is particularly effective when the spacecraft is in an Earth-pointing attitude and the Earth-line component can be directly observed in the tracking data during velocity addition. This trimming feature of the Pioneer 10 spacecraft provides very accurate control of velocity magnitude.

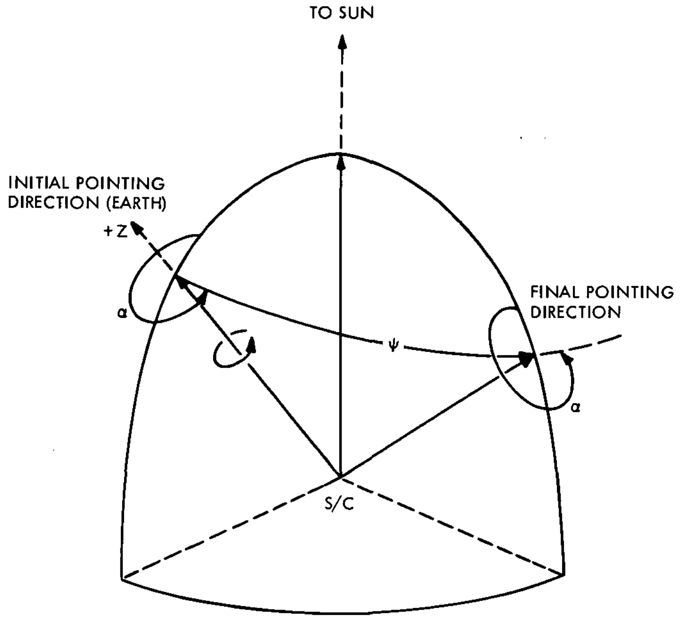

Figure 4. Standard rhumb-line maneuver geometry

The Pioneer maneuver strategy is influenced by a number of spacecraft operational constraints. One is the Sun look angle (SLA) constraint, defined as the angle between the spacecraft-Sun direction and the spacecraft spin axis. This constraint has both an upper and lower limit. The upper limit is a function of spacecraft backside heating and was established as 120 deg for the first and second maneuvers of the Pioneer 10 mission. The lower limit, a function of spacecraft Sun sensor reference accuracy, was established as 10 deg.

Another spacecraft constraint is the maximum Earth look angle (ELA), defined as the angle between the spacecraft–Earth direction and the spacecraft spin axis. This constraint is imposed to maintain adequate signal strength from the medium-gain antenna during maneuvers. For the first maneuver, 4 days after launch, the maximum ELA constraint was established as 45 deg. The second maneuver, 20 days after launch, had a reduced maximum ELA constraint of 24 deg.

The Sun and Earth look angle constraints are illustrated on the surface of a sphere centered at the spacecraft (S/C) in Figure 5. The region A, inside the maximum ELA constraint boundary, but outside the maximum SLA boundary, is an unconstrained pointing direction for the spacecraft spin axis. Also shown in Figure 5 is a region B that is diametrically opposite to region A. When the required velocity vector direction lies in region A, the velocity correction is applied along the positive spin axis. Velocity corrections requiring pointing directions inside region B are achieved using thruster pairs which add velocity along the negative spin axis.

The maneuver strategy must be selected to produce the required encounter conditions at Jupiter without violating these constraints. The selected strategy must also provide a trajectory adjustment within the total multimaneuver capability of 200 m/s allocated for Pioneer 10.

When a single maneuver would violate one or more of the spacecraft constraints, the original required velocity vector is broken into two equivalent unconstrained velocity vectors. Typically, one of the two components is selected along the Earth-line ($\alpha = 0$, $\psi = 0$), while the other is selected near one of the constraining boundaries. An Earth-line maneuver is a highly desirable component, since greatest execution accuracy is attainable in this attitude by making pulsed trim corrections based on the observed change in the doppler tracking signal.

First Maneuver Sequence

The first Pioneer 10 maneuver was scheduled for 4 days after launch to provide an early opportunity to remove injection errors from the trajectory. This epoch, near the Earth, provides flexibility in spacecraft pointing while maintaining adequate spacecraft communication, but is at a sufficient time after launch to permit accurate trajectory estimates. A mean first maneuver of 30 m/s is required to remove the predicted launch vehicle injection errors

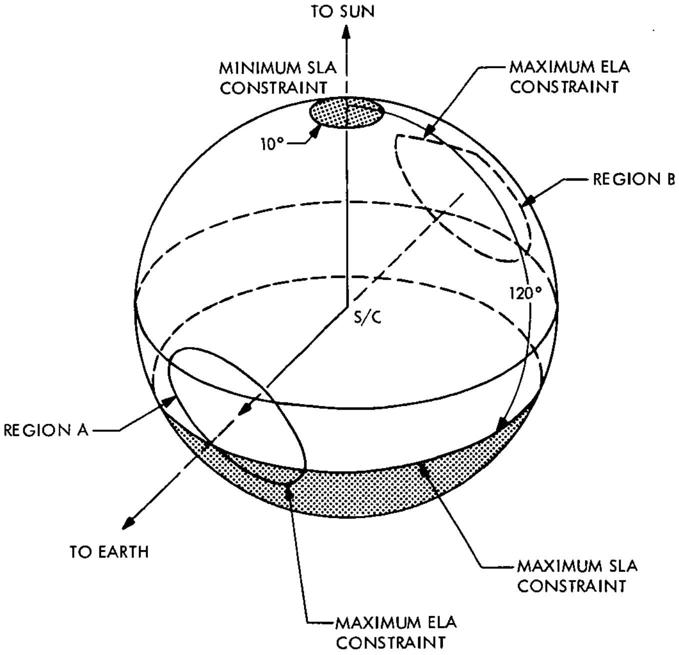

Figure 5. Spacecraft maneuver constraints

(Monte Carlo analysis, Reference 6). The execution errors of this maneuver map to the B-plane as an ellipse with a semi-major axis of approximately 25,000 km (one sigma). A second maneuver of approximately 1 m/s, scheduled for 20 days after launch, is required to remove this error.

A preliminary maneuver analysis using PMOPS, and an orbit solution obtained at launch plus 3 h, indicated that a 14.45-m/s maneuver would deliver the spacecraft to the specified target. This maneuver, with a rhumb angle of 251 deg and a precession magnitude of 75.7 deg, had a pointing direction with an ELA of 76 deg and an SLA of 106 deg.

During spacecraft reorientation to Earth-alignment after injection, telemetry dropouts were experienced in the ELA region where interference between the forward and aft spacecraft antennas exists. This condition, predicted in prelaunch analysis, confirmed the decision to restrict the maneuver to an ELA of less than 45 deg. Although the required single-maneuver direction did not violate the SLA constraints, it did violate the 45-deg ELA constraint. An equivalent two-component first maneuver strategy was developed within this constraint. In addition, it was decided to bias the aimpoint for this maneuver to leave a 0.5-m/s maneuver along the Earth-line for the second maneuver, 20 days after launch, on March 23, 1972. The planned Earth-line component would tend to reduce the pointing direction off the Earth-line and result in improved execution accuracy for the March 23 maneuver. The biased aimpoint for the first maneuver sequence was:

$$\bar{B}\cdot\bar{R} = 216{,}444 \text{ km}$$

$$\bar{B}\cdot\bar{T} = 842{,}564 \text{ km}$$

TCA = December 4, 1973, 00:16:34 GMT

and is shown together with the nominal aimpoint in the B-plane diagram in Figure 6.

The spacecraft sequences for the two-component first maneuver were generated using PMOPS and an updated trajectory estimate based on all doppler tracking data available 12 h before the scheduled maneuver. The required maneuver was reduced in magnitude to 13.45 m/s as a result of the updated trajectory estimate, but the adopted maneuver strategy was not affected.

The first component was initiated by precessing 45 deg from the Earth-line into a plane containing the required velocity (13.45 m/s) and the Earth-line, and adding 18.46 m/s to the spacecraft velocity. Following execution of the initially commanded sequence, the velocity projection along the Earth-line was trimmed to within 0.033 m/s of the desired value using the pulse mode operation of the velocity thrusters, and observing the change in the doppler tracking signal. The expected encounter conditions resulting from this maneuver alone were:

$$\bar{B}\cdot\bar{R} = 353{,}844 \text{ km}$$

$$\bar{B}\cdot\bar{T} = 967{,}188 \text{ km}$$

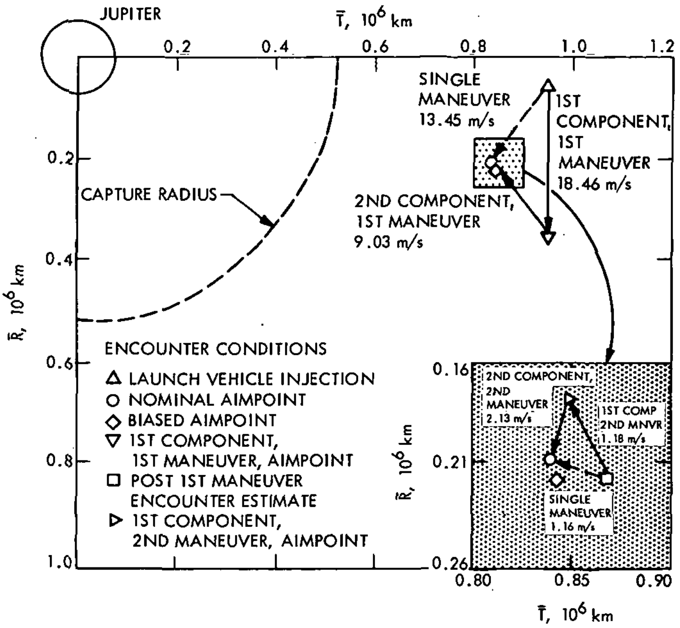

Figure 6. B-plane encounter conditions

TCA = December 2, 1973, 02:48:44 GMT

as shown in Figure 6. These encounter conditions provide for Jupiter arrival within the tracking overlap capabilities of the DSN.

The second component was initiated 7 h after completion of the first component by returning to Earth-alignment and adding 9.03 m/s toward Earth. The desired Earth-line component of velocity change was exceeded by 0.05 m/s but was not trimmed since a residual Earth-line velocity was consistent with the strategy selected for the second maneuver sequence scheduled on March 23.

The total velocity required for both components was 27.49 m/s, compared to 13.45 m/s for the single maneuver. This increase in maneuver velocity magnitude permitted a trajectory adjustment to the biased aimpoint without violation of the 45-deg ELA constraint.

Prior to the first maneuver, the spacecraft battery temperature was observed to be above its preflight prediction. A decision was made to precess the spacecraft backside away from the Sun after the first maneuver to better shade and protect the battery. A cruise attitude with the spacecraft spin axis 24 deg off the nominal Earth-line orientation was selected to maintain the desired signal strength using the medium-gain antenna (Reference 9). This orientation was maintained until re-alignment toward Earth at the second maneuver epoch.

Second Maneuver Sequence

During the period following the first maneuver, the spacecraft was tracked continuously by the DSN. Trajectory estimates were updated as new tracking data became available, and the trajectory changes resulting from the first maneuver were estimated. The 24-deg cruise attitude made data interpretation more difficult because of increased doppler noise caused by the antenna offset from the center of rotation, and an off-nominal solar pressure sailing effect. Solar sailing effects are translations of the spacecraft induced by solar radiation pressure (Reference 8). Torques about the spacecraft center of gravity are also induced by solar pressure, resulting in precession of the spin axis. The effects of solar pressure must be accurately modelled during orbit determination.

The second maneuver sequence was initiated on March 23 at 10:30 GMT. A trajectory estimate based on all doppler tracking data available 12 h before the scheduled maneuver indicated the spacecraft to have the following Jupiter encounter conditions:

$\bar{B}\cdot\bar{R}$ = 218,648 km

$\bar{B}\cdot\bar{T}$ = 869,643 km

TCA = December 3, 1973, 23:33:35 GMT

PMOPS was used to estimate the maneuver required to return the trajectory to the nominal aimpoint. A single maneuver of 1.16 m/s, with a rhumb angle of 1.9 deg, a precession magnitude of 48.6 deg, and a pointing direction with an ELA of 48 deg and an SLA of 13 deg, would provide this adjustment. While the 10- and 120-deg SLA constraints were not violated, the 48-deg ELA required for this maneuver was not acceptable because spacecraft communication requirements restricted the maneuver to an ELA of less than 24 deg. To accommodate the maneuver constraints, an equivalent two-component maneuver strategy was selected.

The first component was executed along the Earth-line by adding 1.18 m/s away from Earth. This orientation was determined to within ¼ deg using the spacecraft high-gain conical scanning capability. The magnitude of the initially commanded velocity change was less than the desired value by approximately 0.024 m/s. A single 1-s pulse was added which resulted in a net overshoot of approximately 0.008 m/s. Although a shorter pulse could be commanded, a decision was made not to trim further, but to account for this overshoot in the computations of the second component.

The second component followed 14 h later by precessing 24 deg from Earth-alignment and applying a velocity of 2.14 m/s to the spacecraft. Computations for this component were updated following the first component execution, and accounted for velocity increments to the spacecraft attributable to:

(1) The unbalanced thrusters used during the 24-deg precession to Earth-alignment prior to the first component.

(2) The first component velocity magnitude as observed in the tracking data, including the 0.008-m/s overshoot.

(3) The unbalanced thrusters used during the 24-deg precession from Earth-alignment to the second component pointing direction.

(4) The unbalanced thrusters used during the 24-deg precession back to Earth-alignment after second component velocity addition.

(5) The unbalanced thrusters used during precession to a 10-deg cruise attitude after completion of the second maneuver sequence.

This strategy allowed for known velocity perturbations.

The Earth-line component of the initially commanded second component velocity magnitude exceeded the desired value by 0.013 m/s. This residual was reduced to 0.004 m/s by trimming in the pulse mode. At the time of this trimming, the Earth direction was 9.3 deg from the direction of maximum flight time sensitivity. This geometry provided for excellent control of flight time, the most sensitive parameter affecting the possible occultation by the Jupiter satellite, Io.

The velocity added during the second maneuver sequence totalled 3.32 m/s, twice the velocity magnitude required for the equivalent single maneuver. The additional velocity provided a trajectory adjustment to the nominal aimpoint without violation of the 24-deg ELA constraint imposed at the time of the March 23 maneuver sequence.

A total of 30.81 m/s of the available 200 m/s was utilized to execute the first and second maneuver sequences.

Spacecraft Occultation by Io

The 12 known satellites of Jupiter can be subdivided into inner and outer groups. The inner group includes five bodies, four of which are quite large, and are called Galilean satellites after their discoverer (1610). One of the smaller of these satellites is Io, about the size of the Earth's Moon and nearly as dense. It revolves in a nearly circular, nearly equatorial, orbit with a period of approximately 42 h, at a distance of approximately 6 Jupiter radii from the center of Jupiter (Reference 10).

Gravitational forces associated with Io have suggested the presence of an atmosphere, although present spectroscopic analyses provide no confirmation. Scientists have noticed a brightening of Io after eclipse by Jupiter, with a return to normal brightness some 15 min later. This brightening has been interpreted to be the result of a temporary deposit of ice on the surface, caused by the lowering of temperature during the eclipse (Reference 10). The occultation of Beta-Scorpii C by Io on May 14, 1971, has allowed scientists to place an upper limit on the atmospheric pressure at 2×10^{-7} atm (Reference 11). Occultation of Pioneer 10 by Io would change the spacecraft radio signals, thus helping to determine possible atmospheric characteristics. The success of the first and second midcourse corrections has placed Pioneer 10 on a trajectory that may provide an occultation opportunity.

Pioneer 10 occultation by Io will occur when the spacecraft passes behind Io, as viewed from Earth. To maximize the probability of an occultation, a trajectory passing behind the full diameter of Io is desired. A center of Io occultation can be achieved by aiming at a point where the magnitude of $\bar{B}$ is 864,385 km (3 Jupiter radii at closest approach), with a θ of 14 deg, and a TCA of December 4, 1973, 02:26 GMT. A variation in any one of these parameters can degrade the occultation geometry. According to preliminary analyses by Kliore (Reference 12), occultation is most sensitive to the time of closest approach. Further analyses by the Navigation Team (Reference 13) indicated that a variation in TCA of ±7 min can cause a total miss of occultation, whereas variations along or perpendicular to $\bar{B}$ of ±25,000 km are required. As of May 28, 1972, trajectory estimates indicated the spacecraft to be headed for the following Jupiter encounter conditions:

$\bar{B}\cdot\bar{T}$ = 208,672 km

$\bar{B}\cdot\bar{R}$ = 837,285 km

TCA = December 4, 1973, 02:35:13 GMT

$|\bar{B}|$ = 862,896 km

θ = 13.99 deg

This trajectory will arrive at Jupiter 1489 km short of the nominal aimpoint in $|\bar{B}|$, 150 km high in the θ direction, and 9.2 min late in TCA. The one-sigma uncertainties in these conditions are 1000 km in spatial miss and 6.4 min in TCA, based on current trajectory estimates and Jupiter and Io ephemeris uncertainties. Based on these data, the probability of achieving an occultation by Io is about 40%.

A trim maneuver could be performed to adjust the current trajectory for an occultation across the center of Io. Present estimates indicate a maneuver in the cruise orientation along the Earth-line of approximately 0.12 m/s, on September 21, 1972, would provide this adjustment (Reference 14). This maneuver epoch has been selected to provide an opportunity to reduce the uncertainty in the trajectory estimate with the acquisition of additional tracking data and improved solar radiation modelling. This maneuver is expected to increase the probability of a successful occultation by Io to about 72%.

The execution accuracy of the Earth-line trim maneuver can be controlled to approximately 0.0004 m/s using the pulse mode. This error in velocity magnitude would project to a TCA error of much less than 1 min, well below the current trajectory estimate and Jupiter and Io ephemeris uncertainties.

The Earth-line maneuver could be delayed until much later in the mission when ephemeris uncertainties may be reduced, permitting improvement of the current trajectory estimate relative to Jupiter. The reduced uncertainties in this estimate would improve the accuracy of evaluating the required maneuver and further increase the probability of an occultation. A delayed maneuver would require a larger velocity correction and may also be less attractive from an operational standpoint.

The encounter geometry for an occultation by Io is shown in Figure 7. Occultation would occur 16 min after closest approach to Jupiter, with a maximum duration of 90 s. An hour after occultation by Io, Pioneer 10 will be occulted by Jupiter. The duration of Jupiter occultation is about 1 h.

Future Plans

The present Io occultation analyses are preliminary. Updating the trajectory estimate as additional tracking data become available will make maneuver strategy more certain and improve the probability of a successful occultation by Io.

Recently, the Io occultation geometry has been examined using computer-generated motion pictures representing the appearance of other bodies as seen from the spacecraft as it moves along the flight path. These film sequences have revealed the possibility of a Pioneer 10 occultation by a second Galilean satellite, Ganymede. It may be possible to adjust the current trajectory in both time and position at closest approach such that a dual occultation of the spacecraft by both Io and Ganymede results (Reference 15). This objective is currently being examined in some detail by the Navigation Team to determine possible trajectory adjustments and assess the impact of such changes on the primary mission objectives. These studies will be reported in future Pioneer documentation.

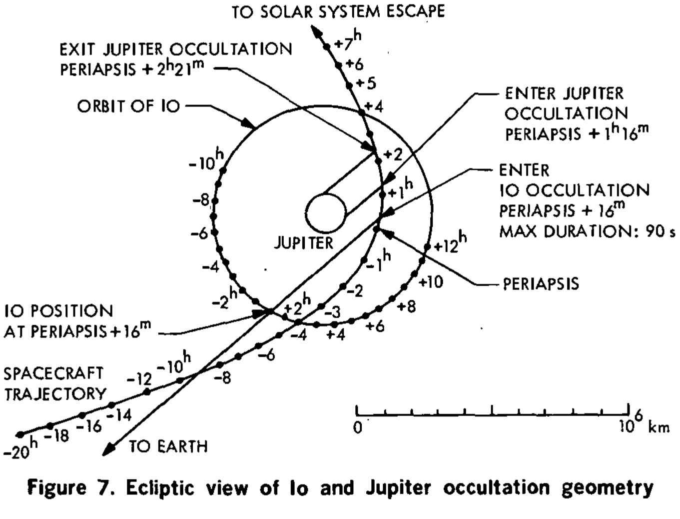

Figure 7. Ecliptic view of Io and Jupiter occultation geometry

References

1. *Pioneer F Mission Operations Plan,* NASA Document No. PC-230, Ames Research Center, Moffett Field, Calif., Apr. 27, 1971.
2. Hall, C. F., "Pioneer F Midcourse Maneuver Accuracy," NASA Letter No. PAL-2-9(244-8), Ames Research Center, Moffett Field, Calif., Feb. 2, 1972.
3. *Pioneer F Computer Program for Midcourse Maneuver-Functional Requirements,* NASA Document No. PC-263, Ames Research Center, Moffett Field, Calif., Oct. 13, 1970.
4. *Pioneer F Midcourse Maneuvers Operations Plan,* NASA Document No. PC-233, Ames Research Center, Moffett Field, Calif., Aug. 9, 1971.
5. Frauenholz, R. B., *Pioneer F Jupiter Flyby 1972 Maneuver Analysis: Part I. Maneuver Capability,* Document No. 616-15, Sept. 1, 1971 (JPL internal document).
6. Frauenholz, R. B., *Pioneer F Jupiter Flyby 1972 Maneuver Analysis: Part II. Maneuver Accuracy,* Document No. 616-15, Jan. 1, 1972 (JPL internal document).
7. Liu, A. S., *Pioneer F Jupiter Flyby 1972 Orbit Determination Strategy and Accuracy Study,* Document No. 616-23, Oct. 4, 1971 (JPL internal document).
8. Campbell, J. K., *Effects of Solar Pressure on Pioneer F Trajectories,* TM 392-70, Jan. 17, 1972 (JPL internal document).
9. Dyer, J. W., "Pioneer 10 (F) Midcourse Maneuver Narrative Summary Report and Critique," NASA Memo No. PAL-2-19, Ames Research Center, Moffett Field, Calif., Apr. 4, 1972.
10. *Handbook of the Physical Properties of the Planet Jupiter,* NASA SP-3031. Office of Technology Utilization, National Aeronautics and Space Administration, Washington, D. C., 1967.
11. "The Occultation of Beta Scorpii by Jupiter and Io," *Astron. J.*, Vol. 77, No. 1, Feb. 1972.
12. Kliore, A. J., "A Preliminary Error Analysis of an Occultation of Pioneer F by Io," IOM 391.9-38, Mar. 31, 1971 (JPL internal document).
13. Ball, J. E., *Pioneer 10 Io Occultation Data and Analysis,* TM 392-90, June 21, 1972 (JPL internal document).
14. Frauenholz, R. B., *Preliminary Pioneer 10 Trim Maneuver Requirements,* TM 392-86, June 12, 1972 (JPL internal document).
15. Penzo, P. A., *Retargeting Pioneer 10 to Include Earth Occultation of Ganymede,* TM 393-107, May 16, 1972 (JPL internal document).

Bibliography of Current Reporting

Author Index With Abstracts

AKYUZ, F. A.

A01 **VISCEL—A General-Purpose Computer Program for Analysis of Linear Viscoelastic Structures: User's Manual**

K. K. Gupta, F. A. Akyuz, and E. Heer

Technical Memorandum 33-466, Vol. I, Rev. 1,
October 1, 1972

For abstract, see Gupta, K. K.

A02 **VISCEL—A General-Purpose Computer Program for Analysis of Linear Viscoelastic Structures: Program Manual**

K. K. Gupta and F. A. Akyuz

Technical Memorandum 33-466, Vol. II, July 15, 1972

For abstract, see Gupta, K. K.

ANENBERG, G. L.

A03 **Spacecraft Ion Beam Noise Effects**

G. L. Anenberg

JPL Quarterly Technical Review, Vol. 2, No. 2, pp. 61–71,
July 1972

An estimate of the antenna noise temperature and the uplink signal-to-noise ratio (S/N) has been made for Bremsstrahlung radiation emitted by a spacecraft ion beam; a worst-case situation in which the spacecraft antenna is located in the exit plane of the ion beam and directed at varying angles into the ion beam is assumed. Numerical results of the antenna noise temperature versus antenna pointing angle are given for a typical set of ion-beam and antenna-pattern parameters. The uplink S/N due to the ion-beam noise alone is given in terms of a critical range in AU at which a typical ranging transmission is received with S/N = 0 dB. The effects of the ion-beam divergence angle and antenna distance on the ion beam are also presented. Results of the study show typical increases in the antenna noise temperature of about 0.2 K and critical ranges of the order of 3–5 AU. An ion engine thus generally introduces an undetectable level of noise into a spacecraft receiver.

ATKINSON, G.

A04 Dissipation Mechanisms in a Pair of Solar-Wind Discontinuities

T. W. J. Unti, G. Atkinson (Communications Research Center), C.-S. Wu (University of Maryland), and M. Neugebauer

J. Geophys. Res., Space Physics, Vol. 77, No. 13, pp. 2250–2263, May 1, 1972

For abstract, see Unti, T. W. J.

AUE, D. H.

A05 Mechanisms of Ion–Molecule Reactions of Propene and Cyclopropane

M. T. Bowers (University of California, Santa Barbara), D. H. Aue (University of California, Santa Barbara), and D. D. Elleman

J. Am. Chem. Soc., Vol. 94, No. 12, pp. 4255–4261, June 14, 1972

For abstract, see Bowers, M. T.

BACK, L. H.

B01 Very High Temperature Laminar Flow of a Gas Through the Entrance Region of a Cooled Tube—Numerical Calculations and Experimental Results

L. H. Back

Int. J. Heat Mass Transfer, Vol. 15, No. 5, pp. 1001–1021, May 1972

The laminar flow equations in differential form are solved numerically on a digital computer for flow of a very high temperature gas through the entrance region of an externally cooled tube. The solution method is described and calculations are carried out in conjunction with experimental measurements. The agreement with experiment is good, with the result indicating relatively large energy and momentum losses in the highly cooled flows considered where the pressure is nearly uniform along the flow and the core flow becomes non-adiabatic a few diameters downstream of the inlet. The effects of a large range of Reynolds number and Mach number (viscous dissipation) are also investigated.

BERMAN, P. A.

B02 Solar Cell Contact Pull Strength as a Function of Pull-Test Temperature

R. K. Yasui and P. A. Berman

Technical Report 32-1563, September 1, 1972

For abstract, see Yasui, R. K.

BOWERS, M. T.

B03 Mechanisms of Ion–Molecule Reactions of Propene and Cyclopropane

M. T. Bowers (University of California, Santa Barbara),
D. H. Aue (University of California, Santa Barbara), and
D. D. Elleman

J. Am. Chem. Soc., Vol. 94, No. 12, pp. 4255–4261,
June 14, 1972

Ion–molecule reaction of the $C_3H_6\cdot^+$ ion from propene proceeds via a "four-center" mechanism to a $C_6H_{12}\cdot^+$ ion capable of 1,2- and 1,4-hydrogen migrations but not 1,3-hydrogen migration. The $C_6H_{12}\cdot^+$ ion can rearrange via the various structures shown. Decomposition to ethylene proceeds via a "four-center" cleavage of the dimethylcyclobutane ion. The $C_3H_6\cdot^+$ ion from cyclopropane can be distinguished from that formed from propene. The $C_6H_{12}\cdot^+$ ion formed on reaction of propene and cyclopropane is different from that formed from propene alone; it undergoes facile cleavage with loss of ethylene. By study of ion–molecule reactions of $CD_3CHCH_2\cdot^+$ formed at energies below the appearance potential of fragment ions a small amount of isotopic scrambling has been observed in the $CD_3CHCH_2\cdot^+$ ion in accord with predictions based on quasi-equilibrium theory. Part of the $C_3H_3^+$ ions formed from propene are unusually unreactive at high pressures with propene and may have the cyclopropenium ion structure.

BROWN, W. E., JR.

B04 Lunar Subsurface Exploration With Coherent Radar

W. E. Brown, Jr.

The Moon, Vol. 4, pp. 113–127, April 1972

The Apollo Lunar Sounder Experiment that is scheduled to orbit the Moon on Apollo 17 consists of a three-frequency coherent radar system and an optical recorder. The coherent radar can be used to measure both phase and amplitude characteristics of the radar echo. Measurement methods that are related to the phase and amplitude will be used to determine the surface profile, locate subsurface features, and ascertain near-surface electrical properties of the lunar surface. The key to the coherent radar measurement is a highly stable oscillator that preserves an accurate phase reference (2 or 3 electrical degrees) over a long period of time. This reference provides a means for reducing surface clutter so that subsurface features are more easily detected and also provides a means of measuring range to the surface to within a fraction of a wavelength.

BURKE, E. S.

B05 DSN Progress Report for May–June 1972: DSN Telemetry Predicts Generation and Distribution

C. W. Harris and E. S. Burke

Technical Report 32-1526, Vol. X, pp. 210–212, August 15, 1972

For abstract, see Harris, C. W.

BUTMAN, S.

B06 Interplex—An Efficient Multichannel PSK/PM Telemetry System

S. Butman and U. Timor

IEEE Trans. Commun., Vol. COM-20, No. 3, pp. 415–419, June 1972

This article describes a new phase-shift-keyed/phase-modulation (PSK/PM) scheme, called Interplex, which improves the performance of multichannel telemetry systems by reducing the cross-modulation loss. In the case of two-channel systems, the improvement in data power efficiency relative to a conventional system can be as much as 3 dB. A major feature of Interplex is that it can be implemented with very minor modification of existing conventional PSK/PM systems.

CAMERON, R. E.

C01 **Farthest South Algae and Associated Bacteria**

R. E. Cameron

Phycologia, Vol. 11, No. 2, pp. 133-139, June 1972

A new record is reported for algae collected from the highest latitude, a frozen pond in the La Gorce Mountains, Antarctica (86°45′S, 146°00′W). Culturable algae included *Neochloris aquatica* Starr and *Schizothrix calcicola* (Ag.) Gom. *Porphyrosiphon Notarisii* (Menegh.) Kütz. was not recoverable in culture. Associated bacteria were soil diphtheroids of the genus *Arthrobacter.* The occurrence of high latitude photosynthetic organisms is important in the search for possible extra-terrestrial life because environmental conditions, in some aspects, approach those of Mars.

C02 **Microbiology of the Dry Valleys of Antarctica**

N. H. Horowitz (California Institute of Technology),
R. E. Cameron, and J. S. Hubbard

Science, Vol. 176, No. 4032, pp. 242-245, April 21, 1972

For abstract, see Horowitz, N. H.

CANNOVA, R. D.

C03 **Development and Testing of the Propulsion Subsystem for the Mariner Mars 1971 Spacecraft**

R. D. Cannova, et al.

Technical Memorandum 33-552, August 1, 1972

In November 1971, the Mariner 9 spacecraft was injected into Mars orbit by a 574-kg (1265-lbm) propulsion system. Design of that system provided for a directed impulse, upon command, to accomplish in-transit trajectory corrections, an orbit-insertion maneuver at encounter to transfer from a flyby to an orbital trajectory about Mars, and a subsequent trim maneuver.

The propulsion system is an integrated, pressure-fed, multi-start, fixed-thrust, storable bipropellant system. The primary subassemblies are a propellant feed system, a 1334-N (300-lbf) thrust rocket engine assembly, and the propulsion module structure. The subsystem was capable of being fueled, pressurized, and monitored before installation on the spacecraft.

This document describes the design, testing, fabrication, and problems associated with the development of the Mariner 9 propulsion system. Also covered are the design and operation of the associated ground support equipment used to test and service the propulsion system.

CHAHINE, M. T.

C04 A General Relaxation Method for Inverse Solution of the Full Radiative Transfer Equation

M. T. Chahine

J. Atmos. Sci., Vol. 29, No. 4, pp. 741-747, May 1972

The relaxation method for the inverse solution of the full radiative transfer equation is generalized to solve for all atmospheric parameters which appear in the integrand as functions or functionals, without any *a priori* information related to the expected solution. The method is illustrated by examples in the Earth's atmosphere for the determination of water vapor mixing ratio profiles from observations in the 6.3-μ band.

CHIRIVELLA, J. E.

C05 Small Rocket Exhaust Plume Data

J. E. Chirivella, P. I. Moynihan, and W. Simon

JPL Quarterly Technical Review, Vol. 2, No. 2, pp. 90-99, July 1972

During recent cryodeposit tests with an 0.18-N (0.04-lbf) thruster in the JPL Molsink facility, the mass flux in the plume back field was measured for the first time for nitrogen, carbon dioxide, and a mixture of nitrogen, hydrogen, and ammonia at various inlet pressures. This mixture simulated gases that would be generated by a hydrazine-plenum attitude propulsion system. The measurements furnish a base upon which to build a mathematical model of plume back flow that will be used in predicting the mass distribution in the boundary region of other plumes. The results are analyzed and compared with existing analytical predictions.

CLAYTON, R. M.

C06 Stability Evaluation of a Rocket Engine for Gaseous Oxygen Difluoride (OF_2) and Gaseous Diborane (B_2H_6) Propellants

R. M. Clayton

Technical Report 32-1561, August 15, 1972

Results of an experimental evaluation of the dynamic stability of a candidate combustor for the space-storable propellants gaseous OF_2/B_2H_6 show that the combustor is unstable without supplementary damping. An analysis using a JPL computer program (TRDL) indicated that the uninhibited engine could be unstable. The experiments, conducted with O_2/C_2H_4 substitute propellants and with 70-30 FLOX/B_2H_6(OF_2 simulated with FLOX), show that the uninhibited combustor has a low stability margin to starting-transient perturbations, but that it is relatively insensitive to bomb disturbances. Damping cavities are shown to provide stability.

COULBERT, C. D.

C07 Survey of Materials for Hydrazine Propulsion Systems in Multicycle Extended Life Applications

C. D. Coulbert and G. Yankura

Technical Memorandum 33-561, September 15, 1972

This report presents an assessment of materials-compatibility data for hydrazine monopropellant propulsion systems applicable to the Space Shuttle vehicle missions. Materials were evaluated for application over a 10-yr/100-mission operational lifetime with minimum refurbishment. A general materials-compatibility rating for a broad range of materials and several propellants based primarily on static liquid propellant immersion testing and an in-depth evaluation of hydrazine decomposition as a function of purity, temperature, material, surface conditions, etc., are presented.

The most promising polymeric material candidates for propellant diaphragms and seals appear to have little effect on increasing hydrazine decomposition rates, but the materials themselves do undergo changes in physical properties which can affect their 10-yr performance in multicycle applications. The available data on these physical properties of elastomeric materials such as EPT-10 and AF-E-332 as affected by exposure to hydrazine or related environments is presented.

The data in this report provides a basis for the preliminary selection of propulsion-system materials. The results of system and component long-term compatibility studies currently being conducted by the Air Force, Martin-Marietta, JPL, and others plus the completion of studies recommended in this report will enable the prediction of 10-yr multicycle performance of the selected materials.

CROW, R. B.

C08 DSN Progress Report for May–June 1972: S-Band Receiver Third-Order Loop Demonstration

R. B. Crow

Technical Report 32-1526, Vol. X, pp. 168–171,
August 15, 1972

In mid-April 1972, the Mariner Mars 1971 spacecraft began encountering high doppler rates under weak signal conditions. The Block III receiver was dropping lock, resulting in lost data. This article describes a third-order tracking filter which was designed for the Block III receiver and successfully demonstrated at the Mars Deep Space Station (DSS 14).

DeGENNARO, L. I.

D01 DSN Progress Report for May–June 1972: Post-Detection Subcarrier Recording Subsystem

L. I. DeGennaro and G. Hamilton

Technical Report 32-1526, Vol. X, pp. 161–163,
August 15, 1972

The Post-Detection Subcarrier Recording Subsystem for the 64-m-diameter antenna stations will be revised from the present configuration at the Mars Deep Space Station (DSS 14). The reasons for the change are to provide for future computer control of the pre/post-calibration process at the new 64-m-diameter antenna stations and to reduce the number of cabinets required to perform the essential functions of the Analog Instrumentation/ Recording Subsystems. This article describes changes from the present configuration, including patching functions, test equipment, and semi-automatic and automatic computer control.

DIVINE, N.

D02 Models for the Atmospheres of Jupiter and Saturn

N. Divine and F. D. Palluconi

JPL Quarterly Technical Review, Vol. 2, No. 2, pp. 1–8,
July 1972

Numerical models of the atmospheres of Jupiter and Saturn have been created for use in the development of design criteria for space vehicles intended to investigate these planets. These models contribute to spacecraft design by providing a basis for the assessment of entry heating, the transmission and emission of radiation, and structural and aerodynamic interactions. The model atmospheres are based on data and analyses published in the literature through 1970. The composition is discussed, and the relative amounts of each molecular species are tabulated for nominal and extreme cases. The structure of the atmospheric regions is discussed, and the principal features of one nominal and two limiting models for each planet are indicated. The models are illustrated by pressure-temperature profiles which also display the major cloud layers. Reference is made to complete descriptions of altitude, pressure, temperature, density, scale height, and cloud relationships for these models which are specified in appropriate NASA publications.

DONNELLY, H.

D03 DSN Progress Report for May–June 1972: Programmed Oscillator Development

H. Donnelly and M. R. Wick

Technical Report 32-1526, Vol. X, pp. 180–185,
August 15, 1972

This article describes the addition of programmed oscillators in the Block III receiver/exciter subsystems at the Mars and Ballima Deep Space Stations (DSSs 14 and 43) for Pioneer 10 support during Jupiter flyby. A brief description of the tracking requirements of the mission and the subsystem modifications to incorporate the programmed oscillators is given.

DOWNS, G. S.

D04 The Distribution of Linear Polarization in Cassiopeia A at Wavelengths of 9.8 and 11.1 cm

G. S. Downs and A. R. Thompson (Stanford University)

Astron. J., Vol. 77, No. 2, pp. 120–133, March 1972

Two series of observations of the brightness distribution of the linearly polarized component of the radiation of Cassiopeia A are described. The first was made at a wavelength of 9.8 cm using a two-element interferometer at Stanford University which provided a synthesized beamwidth of $1'.6 \times 2'.7$. The second set of observations was made with the three-element interferometer of the National Radio Astronomy Observatory (NRAO) at a wavelength of 11.1 cm and a beamwidth of $8''.1 \times 9''.3$ was obtained. Because the increments in the antenna spacing of the NRAO interferometer are greater than the critical interval for Cassiopeia A, part of the brightness distribution is missing from the synthesized map at

11.1 cm. This missing component is estimated to contain only 5% of the polarized flux density. The polarized radiation is concentrated in the main bright ring of the source and at a 11.1-cm wavelength the maxima in the polarized brightness correspond to ≈5% of the unpolarized radiation. A comparison of the observations with published results at other wavelengths shows that Faraday depolarization reduces the polarized radiation to half the intrinsic value at a wavelength of approximately 7.5 cm. The mean values of the rotation of the position angle of the polarization at a number of points indicate a greater rate of rotation as a function of λ^2 at wavelengths shorter than 6 cm than at longer ones.

These data are hardly detailed enough to rule out the possibility of linear rotation with λ^2 but appear to be best interpreted in terms of a nonlinear rotation within the source, together with a linear rotation of about -35 rad-m^{-2} which may be attributed to the interstellar medium. The internal rotation can be explained by a model of the source with a radial magnetic field and a thermal electron density of 2 cm^{-3}. The Appendix discusses the effect on synthesis observations of the use of increments in the antenna spacing which are too large. Such undersampling results in the presence of grating lobes, the responses of which can only be separated from the main-beam responses for components of the source of dimensions less than the spacing of the grating lobes. Broader components of the source are lost, and to estimate the flux density of the unconfused main-beam responses it is necessary to correct the brightness scale by a factor derived from the beam pattern.

DWIVEDI, N. P.

D05 Aiming Strategies for Quarantined Multi-Planet Missions

N. P. Dwivedi

JPL Quarterly Technical Review, Vol. 2, No. 2, pp. 9–17, July 1972

An important flight-path constraint for current and future interplanetary missions arises from planetary quarantine restrictions. Each planet is assigned a maximum allowable probability of contamination which must not be exceeded. A portion of this probability is suballocated among the trajectory correction maneuvers. The remaining portion is allocated to the small ejecta/efflux sources released from the spacecraft that could possibly reach the planetary atmosphere and surface. For each maneuver, the suballocation is translated into an allowable probability of planetary impact. At the time of making a maneuver, the allowable probability of impact may dictate biasing the aim point. This study describes the technique of determining preferred biased aim points, given the suballocated probability of contamination for each maneuver.

ELACHI, C.

E01 Dipole Antenna in Space–Time Periodic Media

C. Elachi

IEEE Trans. Anten. Prop., Vol. AP-20, No. 3, pp. 280–287, May 1972

The problem of dipole radiation in sinusoidally space–time periodic media is studied and solved. The space–time periodicity can be considered as due to a strong pump wave and is expressed as a traveling-wave type change in the dielectric constant or the plasma density, i.e.,

$$\epsilon(z,t) = \epsilon_0 \epsilon_r [1 + \epsilon_1 \cos (Kz - \Omega t)]$$

$$N(z,t) = N_0 [1 + N_1 \cos (Kz - \Omega t)]$$

The solution also covers the limit case of a sinusoidally stratified medium ($\Omega = 0$). The solution is formulated in a matrix form, such that the basic results and diagrams apply, with minor changes, to the different cases studied: electric and magnetic dipole in a dielectric, plasma, and uniaxial plasma. The wave-vector diagram is used extensively in studying and presenting the different properties of the solution: caustics, effect of the disturbance (pump wave) motion, harmonics, radiation outside the allowed cone in a uniaxial plasma. Many dipole radiation patterns are given and their features explained physically. Finally, the solution and results are extended to the generally space–time periodic media where $\epsilon(z,t)$ and $N(z,t)$ behave as

$$\eta(z,t) = \eta_0 [1 + \eta_1 f(Kz - \Omega t)]$$

where $f(\xi)$ is any periodic function.

E02 Electromagnetic Wave Propagation and Wave-Vector Diagram in Space–Time Periodic Media

C. Elachi

IEEE Trans. Anten. Prop., Vol. AP-20, No. 4, pp. 534–536, July 1972

The electromagnetic wave propagation and wave-vector diagram in generally space–time periodic dielectric, plasma, and uniaxial plasma are studied for transverse electric and transverse magnetic waves. The case of a sinusoidal periodicity is solved numerically. Special properties due to the inhomogeneity are presented.

ELLEMAN, D. D.

E03 Mechanisms of Ion–Molecule Reactions of Propene and Cyclopropane

M. T. Bowers (University of California, Santa Barbara), D. H. Aue (University of California, Santa Barbara), and D. D. Elleman

J. Am. Chem. Soc., Vol. 94, No. 12, pp. 4255–4261, June 14, 1972

For abstract, see Bowers, M. T.

FINNIE, C.

F01 DSN Progress Report for May–June 1972: Tracking and Ground Based Navigation: Performance of Hydrogen Maser Cavity Tuning Servo

S. Petty and C. Finnie

Technical Report 32-1526, Vol. X, pp. 113–115, August 15, 1972

For abstract, see Petty, S.

FRANZGROTE, E. J.

F02 Use of a Solid-State Detector for the Analysis of X-Rays Excited in Silicate Rocks by Alpha-Particle Bombardment

E. J. Franzgrote

Advances in X-Ray Analysis, Vol. 15, pp. 388–406, Plenum Publishing Corporation, New York 1972

The analysis of alpha-excited X-rays has been studied as a possible addition to the alpha-scattering technique used on the Surveyor spacecraft for the first *in situ* chemical analyses of the lunar surface. Targets of pure elements, simple compounds, and silicate rocks have been exposed to alpha particles and other radiation from a curium-244 source and the resulting X-ray spectra measured by means of a cooled lithium-drifted silicon detector and pulse-height analysis.

The study shows that the addition of an X-ray mode to the alpha-scattering analysis technique would result in a significant improvement in analytical capability for the elements. In particular, important indicators of geochemical differentiation between certain elements (that are only marginally separated in an alpha-scattering and alpha-proton analysis) may be determined quantitatively by measuring the alpha-excited X-rays. An X-ray detector is under consideration as an addition to an alpha-scattering instrument now under development for possible use on a Mars-lander mission.

FRASER, S. J.

F03 **A Re-evaluation of Material Effects on Microbial Release From Solids**

D. M. Taylor, S. J. Fraser (The Boeing Company), E. A. Gustan (The Boeing Company), R. L. Olson (The Boeing Company), and R. H. Green

Life Sciences and Space Research X, Vol. 10, pp. 23–28, Akademie-Verlag, Berlin, 1972

For abstract, see Taylor, D. M.

GOLDER, J.

G01 **Thermal Noise in Space-Charge-Limited Hole Current in Silicon**

A. Shumka, J. Golder, and M.-A. Nicolet

JPL Quarterly Technical Review, Vol. 2, No. 2, pp. 72–76, July 1972

For abstract, see Shumka, A.

GOODWIN, P. S.

G02 **DSN Progress Report for May–June 1972: Helios Mission Support**

P. S. Goodwin

Technical Report 32-1526, Vol. X, pp. 14–19, August 15, 1972

Project Helios, named after the ancient Greek God of the Sun, is a joint undertaking by the Federal Republic of West Germany and the United States of America, who divide the project responsibilities. Each country has a Project Manager who is responsible for his own country's contribution as determined by the International Agreement. In addition, the two Project Managers act as co-Chairmen of the internationally structured Helios Joint Working Group Meetings which are held semi-annually and alternate between the two countries. The project objective is to launch into heliocentric orbits two unmanned scientific spacecraft that will come closer to the Sun than any known or planned spacecraft to date for the purpose of obtaining further knowledge about the Sun and its influence upon life on Earth. The plan is to launch the first spacecraft in mid-1974 and the second in late 1975.

Prior articles of this series described the history and organization of this program, the spacecraft configuration and trajectory, its telecommunications system, and the results of Joint Working Group Meetings. This article deals with the activities and highlights of the Sixth Helios Joint Working Group Meeting which was held at JPL in April–May 1972.

GRAULING, C. R.

G03 DSN Progress Report for May–June 1972: Performance Capabilities of the Data Decoder Assembly Through the Viking Era

C. R. Grauling and N. J. Jones

Technical Report 32-1526, Vol. X, pp. 164–167, August 15, 1972

The Data Decoder Assembly will be performing several different telemetry processing functions at various antenna sites through the Mariner Venus–Mercury 1973, Helios, and Viking eras. These include sequential decoding, block decoding, and high-rate formatting of telemetry data. This article describes how these functions have been implemented by either test or operational software.

GREEN, R. H.

G04 A Re-evaluation of Material Effects on Microbial Release From Solids

D. M. Taylor, S. J. Fraser (The Boeing Company), E. A. Gustan (The Boeing Company), R. L. Olson (The Boeing Company), and R. H. Green

Life Sciences and Space Research X, Vol. 10, pp. 23–28, Akademie-Verlag, Berlin, 1972

For abstract, see Taylor, D. M.

GRUMM, R.

G05 **Mariner Mars 1971 Data Storage Subsystem Final Report**

R. Grumm

Technical Memorandum 33-554, September 15, 1972

A digital tape recorder was used on the Mariner Mars 1971 spacecraft to record television and scientific data. Data was recorded at 132 kbits/s and reproduced at one of five available rates (16.2, 8.1, 4.05, 2.025, or 1.0125 kbits/s) selected by ground command to be congruous with the spacecraft-to-Earth communications link performance. The transport mechanism contained 167 m of 1.2-cm magnetic recording tape. A single motor was used to drive the peripheral drive transport.

During development of the design, "stick-slip" problems were encountered and the selection of 3M 20250 tape, made by Minnesota Mining and Manufacturing, was an important part of the solution to this problem. The design life of 2400 tape passes was achieved during the mission.

GUPTA, K. K.

G06 **VISCEL—A General-Purpose Computer Program for Analysis of Linear Viscoelastic Structures: User's Manual**

K. K. Gupta, F. A. Akyuz, and E. Heer

Technical Memorandum 33-466, Vol. I, Rev. 1,
October 1, 1972

This revised user's manual describes the details of a general-purpose computer program VISCEL (VISCoELastic analysis) which has been developed for an analysis of equilibrium problems of linear thermoviscoelastic structures. The program, an extension of the linear equilibrium problem solver ELAS, is an updated and extended version of its earlier form (written in FORTRAN II for the IBM 7094 computer). A synchronized material property concept utilizing incremental time steps and the finite-element matrix displacement approach has been adopted for the current analysis. Resulting recursive equations incorporating memory of material properties are solved at the end of each time step of the general step-by-step procedure in the time domain. A special option enables employment of constant time steps in the logarithmic scale, thereby reducing computational efforts resulting from accumulative material memory effects. A wide variety of structures with elastic or viscoelastic material properties can be analyzed by VISCEL.

The program is written in FORTRAN V language for the UNIVAC 1108 computer operating under the EXEC 8 system. Dynamic storage allocation is automatically effected by the program, and the user may request up to 195K core memory in a 260K UNIVAC 1108/EXEC 8 machine. The physical program VISCEL, consisting of about 7200 instructions, has four distinct links (segments), and the compiled program occupies a maximum of about 11711-word decimal core storage. VISCEL is stored on magnetic tape and is available from the Computer Software Management and Information Center (COSMIC).

G07 VISCEL—A General-Purpose Computer Program for Analysis of Linear Viscoelastic Structures: Program Manual

K. K. Gupta and F. A. Akyuz

Technical Memorandum 33-466, Vol. II, July 15, 1972

VISCEL is a general-purpose computer program developed for the equilibrium analysis of linear viscoelastic structures. The program is written in FORTRAN V language to operate on the UNIVAC 1108 computer under the EXEC 8 operating system. VISCEL, an extension of the linear equilibrium problem solver ELAS, is an updated and extended version of its earlier form written for the IBM 7094 computer. The users may change the size of labeled COMMON to accommodate the particular problem to be solved without recompilation; it is possible to utilize up to 195K core memory in a 260K UNIVAC 1108/EXEC 8 machine. The physical program, consisting of approximately 7200 instructions, is stored on magnetic tape and is available from the Computer Software Management and Information Center (COSMIC), the NASA agency for the distribution of computer programs.

Finite-element matrix displacement approach coupled with the synchronized material property concept, utilizing incremental time steps, has been adopted for the present solution. The step-by-step procedure involves solution of recursive equations in the time domain, which takes into account the memory of material properties. Incremental and accumulative displacements and stresses are obtained at the end of each such time step. In order to minimize the extent of computations resulting from accumulative effects of material memory, the program provides an option which enables the employment of constant time steps in the logarithmic scale. Vol. I, Rev. 1, of this memorandum describes the user's manual, whereas the present volume is concerned with program documentation.

GUSTAN, E. A.

G08 **A Re-evaluation of Material Effects on Microbial Release From Solids**

D. M. Taylor, S. J. Fraser (The Boeing Company), E. A. Gustan (The Boeing Company), R. L. Olson (The Boeing Company), and R. H. Green

Life Sciences and Space Research X, Vol. 10, pp. 23–28, Akademie-Verlag, Berlin, 1972

For abstract, see Taylor, D. M.

HADEK, V.

H01 ***Superconductivity in the Alkali Metal Intercalates of Molybdenum Disulphide***

R. B. Somoano, V. Hadek, and A. Rembaum

JPL Quarterly Technical Review, Vol. 2, No. 2, pp. 83–89, July 1972

For abstract, see Somoano, R. B.

HAMILTON, G.

H02 **DSN Progress Report for May–June 1972: Post-Detection Subcarrier Recording Subsystem**

L. I. DeGennaro and G. Hamilton

Technical Report 32-1526, Vol. X, pp. 161–163, August 15, 1972

For abstract, see DeGennaro, L. I.

HARDY, J.

H03 **Gain Calibration of a Horn Antenna Using Pattern Integration**

A. C. Ludwig, J. Hardy, and R. Norman

Technical Report 32-1572, October 1, 1972

For abstract, see Ludwig, A. C.

HARRIS, C. W.

H04 **DSN Progress Report for May–June 1972: DSN Telemetry Predicts Generation and Distribution**

C. W. Harris and E. S. Burke

Technical Report 32-1526, Vol. X, pp. 210–212,
August 15, 1972

The DSN Telemetry System Analysis Group is responsible for generating and/or disseminating the predicted uplink signal levels at the spacecraft, and the predicted downlink signal levels at the deep space stations. Also included in the predictions are the telemetry signal-to-noise ratios. Two different Univac 1108 programs are used to generate these data. The JPL spacecraft-oriented predicts are generated by the Telecommunications Prediction and Analysis Program. The non-JPL spacecraft-oriented predicts are generated by the DSN Telecommunications Prediction Program which is operated by the Telemetry Group of the Network Analysis Team. These predicts are distributed throughout the DSN and to specified project personnel.

HARTLEY, R. B.

H05 **DSN Progress Report for May–June 1972: Apollo Mission Support**

R. B. Hartley

Technical Report 32-1526, Vol. X, pp. 41–48,
August 15, 1972

This article describes the support provided by the DSN to the Spaceflight Tracking and Data Network during the Apollo 16 mission. Support was provided by three 26-m- (85-ft-) antenna deep space stations, the 64-m- (210-ft-) antenna Mars Deep Space Station (DSS 14), the Ground Communications Facility, and the Space Flight Operations Facility. Pre-mission and mission activities of the DSN are discussed, and the mission is described.

HASBACH, W. A.

H06 **Summary Report on the Development, Design and Test of a 66-W/kg (30-W/lb) Roll-Up Solar Array**

W. A. Hasbach and R. G. Ross, Jr.

Technical Report 32-1562, September 15, 1972

This report summarizes the results of a program to develop a 23-m^2 (250-ft^2) roll-up solar array with a power-to-weight ratio exceeding 66 W/kg (30 W/lb). Descriptions of the system design and fabrication of a full-scale engineering development unit are included, the system and development test program results are described, and conclusions are drawn. Special test equipment and test procedures are included, together with comparisons of experimental and analytical results.

HAVENS, W. F.

H07 Scan Pointing Calibration for the Mariner Mars 1971 Spacecraft

W. F. Havens, G. I. Jaivin, G. D. Pace, and R. A. Virzi

Technical Memorandum 33-556, August 1, 1972

This report describes the methods used to calibrate the pointing direction of the Mariner Mars 1971 spacecraft scan platform. Accurate calibration was required to meet the pointing accuracy requirements of the scientific instruments mounted on the platform. A detailed ground calibration was combined with an in-flight calibration utilizing narrow-angle television pictures of stars. Results of these calibrations are summarized.

HEER, E.

H08 VISCEL—A General-Purpose Computer Program for Analysis of Linear Viscoelastic Structures: User's Manual

K. K. Gupta, F. A. Akyuz, and E. Heer

Technical Memorandum 33-466, Vol. I, Rev. 1,
October 1, 1972

For abstract, see Gupta, K. K.

HILDEBRAND, C. E.

H09 DSN Progress Report for May–June 1972: Preliminary Evaluation of Radio Data Orbit Determination Capabilities for the Saturn Portion of a Jupiter–Saturn–Pluto 1977 Mission

V. J. Ondrasik, C. E. Hildebrand, and G. A. Ransford

Technical Report 32-1526, Vol. X, pp. 59–75,
August 15, 1972

For abstract, see Ondrasik, V. J.

H10 DSN Progress Report for May–June 1972: Determining the

Mass and Ephemeris of Saturn by Radio Tracking of a Jupiter–Saturn–Pluto 1977 Spacecraft

V. J. Ondrasik, C. E. Hildebrand, and G. A. Ransford

Technical Report 32-1526, Vol. X, pp. 76–81,
August 15, 1972

For abstract, see Ondrasik, V. J.

HOGGAN, H. R.

H11 **DSN Progress Report for May–June 1972: Experimental S- and X-Band Feed System Ellipsoid Reflector**

H. R. Hoggan and W. Kissane

Technical Report 32-1526, Vol. X, pp. 186–190,
August 15, 1972

To support the Mariner Venus–Mercury 1973 X-band experiment, the S/X feed system has been designed and is currently under fabrication for installation on the Mars Deep Space Station (DSS 14) 64-m-diameter antenna. The system will allow both S- and X-band signals to be received along the same bore-sight direction. Basic elements of the system are the ellipsoid reflector over the S-band horn and a dichroic reflector plate over the X-band cone. The first parts to be manufactured are the ellipsoid reflector and its backup structure. This article describes the ellipsoid reflector, the method used to form it, the measured accuracy of the finished part, and its connection to the backup structure.

HOLCOMB, L. B.

H12 **Satellite Auxiliary-Propulsion Selection Techniques: Application of Selection Techniques to the ATS-H Satellite**

L. B. Holcomb

Technical Report 32-1505, Suppl. 1, October 1, 1972

JPL Technical Report 32-1505 and the addendum thereto described auxiliary-propulsion systems applicable to unmanned satellites and documented an approach for satellite designers to use in selecting systems that are the most effective for their mission. This supplement discusses the analysis required to estimate auxiliary-propulsion system requirements for a mission. These requirements include tipoff rate reduction, acquisitions, disturbance torques, orbital disturbances, and spacecraft-commanded maneuvers. A comparison of several candidate auxiliary-propulsion systems and system combinations for an Advanced Applications Technology

Satellite (ATS-H) is presented. A generalized auxiliary propulsion system tradeoff, based on mission cost effectiveness criteria, is described. The specific mission assumptions for the ATS-H spacecraft are included, along with a discussion of the sensitivity of the final selection to these assumptions.

H13 European Auxiliary Propulsion—1972

L. B. Holcomb

Technical Memorandum 33-555, September 1, 1972

During the last half decade, low-thrust auxiliary-propulsion technology has experienced rapid growth in Europe due to the development of new and more complex satellites. To gain insight into the auxiliary-propulsion technology state-of-the-art in Europe, the survey presented in this report was undertaken. The chemical and electric auxiliary-propulsion technology of the United Kingdom, France, and West Germany is discussed in detail, and the propulsion technology achievements of Italy, India, Japan, and Russia are reviewed. A comparison of Shell 405 catalyst and a European spontaneous hydrazine catalyst called CNESRO I is also presented. Finally, conclusions are drawn regarding future trends in European auxiliary-propulsion technology development.

HOROWITZ, N. H.

H14 Microbiology of the Dry Valleys of Antarctica

N. H. Horowitz (California Institute of Technology),
R. E. Cameron, and J. S. Hubbard

Science, Vol. 176, No. 4032, pp. 242–245, April 21, 1972

The dry valleys of South Victoria Land, Antarctica, together with a few other ice-free areas on the perimeter of the Antarctic continent, form what is generally considered to be the most extreme cold-desert region of the Earth. During the past 5 years, the dry valleys have served as a model environment for investigating questions connected with the biological exploration of Mars. The extraordinary aridity of the region, its low temperature, and its geographical isolation give it a quasi-Martian character, although it is to be understood that the actual Martian environment is still more hostile than that of the valleys.

The kinds, numbers, and distribution of soil microorganisms in the valleys have been investigated in order to gain insight into the practical problems of searching for life in an extreme environment. Detailed results of these studies have been reported elsewhere. This article reviews the major findings in this region, especially as they apply to Martian exploration.

HUBBARD, J. S.

H15 Microbiology of the Dry Valleys of Antarctica

N. H. Horowitz (California Institute of Technology),
R. E. Cameron, and J. S. Hubbard

Science, Vol. 176, No. 4032, pp. 242–245, April 21, 1972

For abstract, see Horowitz, N. H.

HUNT, G. E.

H16 Laboratory Simulation of Diffuse Reflectivity From a Cloudy Planetary Atmosphere

J. S. Margolis, D. J. McCleese, and G. E. Hunt

Appl. Opt., Vol. 11, No. 5, pp. 1212–1216, May 1972

For abstract, see Margolis, J. S.

H17 Formation of Spectral Lines in Planetary Atmospheres: III. The Use of Analytic Scattering Diagrams in Computations of Synthetic Spectra for Cloudy Atmospheres

G. E. Hunt

J. Quant. Spectrosc. Radiat. Transfer, Vol. 12, No. 6,
pp. 1023–1028, June 1972

In order to interpret planetary spectra formed in a cloudy atmosphere in a meaningful way, it is necessary to compute synthetic spectra from realistic models where the physical processes are accurately taken into account. Anisotropic scattering diagrams for the cloud particles must be used. This article presents the results of some comparisons that have been made of line profiles and equivalent widths computed from atmospheric models where the scattering has been represented by the Mie theory and a simple analytic expression, the Heyney–Greenstein function. These results show that the spectroscopic features for these models are indistinguishable and demonstrate the value of using this simple analytic function in terms of the enormous saving in computer time, when computing synthetic spectra for any cloudy planetary atmosphere.

HUNTRESS, W. T., JR.

H18 An ESCA Study of Lunar and Terrestrial Materials

W. T. Huntress, Jr., and L. Wilson (Varian Associates)

Earth Planet. Sci. Lett., Vol. 15, pp. 59-64, May 1972

The electron spectroscopy for chemical analysis (ESCA) technique is used to obtain rapid, nondestructive, elemental analysis of selected lunar samples. The chemical shift of the Fe(2*p*) line in lunar material is found characteristic of iron in the Fe^{2+} state. A difference in binding energy of approximately 0.5 eV is observed between the 0(1*s*) levels of the terrestrial minerals fayalite and quartz, and effects due to surface oxidation and adsorption are also observed in terrestrial materials.

HURD, W. J.

H19 DSN Progress Report for May–June 1972: DSN Station Clock Synchronization by Maximum Likelihood VLBI

W. J. Hurd

Technical Report 32-1526, Vol. X, pp. 82–95,
August 15, 1972

The clocks at the deep space stations can be accurately synchronized by very-long-baseline interferometry (VLBI) at lower operational cost than by the existing Moon bounce system. More than an order of magnitude improvement in accuracy can be attained using existing DSN hardware, and ultimate accuracies on the order of 10 ns are possible. The purpose of the analysis described in this article is to optimize the acquisition and processing of the VLBI data subject to hardware constraints, in order to achieve the best possible time synchronization estimate for a given amount of data and the most efficient usage of the DSN facilities.

JACKSON, E. B.

J01 DSN Progress Report for May–June 1972: DSN Research and Technology Support

E. B. Jackson

Technical Report 32-1526, Vol. X, pp. 149–152,
August 15, 1972

This article summarizes the activities of the Development Support Group, including the Microwave Test Facility, during the two-month period ending June 15, 1972. Activities include operational clock synchronization, precision antenna gain measurements, weak source observations, pulsar observations, demonstration of the Scan and Correct Using Receiver computer program for automatic antenna tracking, planetary radar experiments, dual-carrier measurements, and shipment of the tricone support structure. Activities at the Microwave Test Facility include DSN klystron testing and general machine shop and other support for the Venus Deep Space Station. Significant maintenance activities include replacement of an azimuth drive gear reducer and rework of the elevation ball screw nuts on the 26-m-diameter antenna.

JAIVIN, G. I.

J02 Scan Pointing Calibration for the Mariner Mars 1971 Spacecraft

W. F. Havens, G. I. Jaivin, G. D. Pace, and R. A. Virzi

Technical Memorandum 33-556, August 1, 1972

For abstract, see Havens, W. F.

J03 A General Purpose Maneuver Turns Computer Program

G. I. Jaivin

Technical Memorandum 33-558, August 15, 1972

This report presents the theory, functional description, and operating instructions of a general purpose maneuver analysis program. The program computes the maneuver turns required to point a given spacecraft-fixed vector in the direction of a given inertially-fixed vector. Any two-turn maneuver sequence may be arbitrarily chosen. If it is not possible to accomplish the desired orientation with a two-turn sequence, a three-turn sequence can be specified. In addition, the coordinates of an arbitrarily selected inertially-fixed reference vector are computed before and after each turn that is performed. Two program options provide, if desired, the reference vector coordinates at selected points throughout each turn and the reference vector positions before and after each turn of an arbitrarily prescribed set of maneuver turns.

JET PROPULSION LABORATORY

J04 JPL Contributions to Structural Integrity Survey, JANNAF Interagency Propulsion Committee (For Meeting of January 8–12, 1973, at NASA Langley Research Center)

Jet Propulsion Laboratory

Technical Memorandum 33-562, July 31, 1972

The following nine papers, documenting JPL contributions to the Structural Integrity Survey of the JANNAF Interagency Propulsion Committee, are presented:

"Use of Fracture Mechanics To Determine Material Allowables for Propulsion Subsystems" by J. C. Lewis

"Design and Qualification of Pressure Vessels by Use of Fracture Mechanics Concepts" by B. K. Wada and C. N. Larson

"Fabrication and Testing of Full-Scale Advanced Composite Tape-Wound Rocket Motor Cases" by W. M. Jensen and R. L. Bailey

"Design and Analysis of Tape Wound Pressure Cases" by A. C. Knoell and E. Y. Robinson

"Reliability of Composite Vessels and Proof Testing" by J.-N. Yang and A. C. Knoell

"Lifetime Analyses of Fiber Composites Under Static Loads" by E. Y. Robinson

"Application of Acoustic Emission (AE) To Assess Structural Integrity of Advanced Composite Rocket Motor Cases" by E. Y. Robinson

"High Strength Carbon-Carbon Composites for Integrated Solid Rocket Nested Motor Concept" by C. D. Coulbert and J. I. Shafer

"Numerical Analysis of Viscoelastic Structures Using the VISCEL Computer Program" by K. K. Gupta

JOHNS, C. E.

J05 DSN Progress Report for May–June 1972: Block IV Receiver Development

C. E. Johns

Technical Report 32-1526, Vol. X, pp. 175–179, August 15, 1972

This article describes a digital control assembly developed for use in controlling the frequency of a Dana Laboratory Digiphase synthesizer, Model 7010-S-179. The control assembly allows the synthesizer to be used as the oscillator within a phase-locked loop. A brief analysis using the synthesizer control assembly in a third-order loop is included.

JONES, N. J.

J06 DSN Progress Report for May–June 1972: Performance Capabilities of the Data Decoder Assembly Through the Viking Era

C. R. Grauling and N. J. Jones

Technical Report 32-1526, Vol. X, pp. 164–167,
August 15, 1972

For abstract, see Grauling, C. R.

KINDER, W. J.

K01 DSN Progress Report for May–June 1972: End-to-End Medium Rate Telemetry System Test

W. J. Kinder

Technical Report 32-1526, Vol. X, pp. 5–9,
August 15, 1972

An end-to-end test of the operational medium-rate telemetry system was conducted on May 23, 1972. The errors recorded seem to group themselves around three patterns: those errors associated with 360-computer time corrections, those errors concerned with Ground Communications Facility (GCF) transmission, and those errors originating in the GCF/synchronizer/360 interface. Noise on the data-block-detected signal from the GCF decoder to the Space Flight Operations Facility (SFOF) synchronizers is suspected. A recommendation is made for a facility test between the GCF and SFOF to be undertaken to validate the quality of the data-block-detected signal per transfer agreement and assembly specifications.

KISSANE, W.

K02 DSN Progress Report for May–June 1972: Experimental S- and X-Band Feed System Ellipsoid Reflector

H. R. Hoggan and W. Kissane

Technical Report 32-1526, Vol. X, pp. 186–190,
August 15, 1972

For abstract, see Hoggan, H. R.

LEFLANG, J. G.

L01 DSN Progress Report for May–June 1972: Novel 70-MHz Limiting Amplifier

J. G. Leflang and R. N. MacClellan

Technical Report 32-1526, Vol. X, pp. 172–174,
August 15, 1972

A high-speed digital differential comparator has been successfully utilized as the limiting element in an RF module operating in the VHF region. The device exhibits good amplitude and phase characteristics. This article describes the design and test results of the device, which uses emitter-coupled logic as a limiting amplifier.

LEIBOWITZ, L. P.

L02 Measurements of the Structure of an Ionizing Shock Wave in a Hydrogen–Helium Mixture

L. P. Leibowitz

Technical Memorandum 33-563, September 1, 1972

Shock structure during ionization of a hydrogen–helium mixture has been studied using hydrogen line and continuum emission measurements. A reaction scheme is proposed which includes hydrogen dissociation and a two-step excitation–ionization mechanism for hydrogen ionization by atom–atom and atom–electron collisions. Agreement has been achieved between numerical calculations and measurements of emission intensity as a function of time for shock velocities from 13 to 20 km/sec in a 0.208 H_2—0.792 He mixture. The electron temperature was found to be significantly different from the heavy-particle temperature during much of the ionization process. Similar time-histories for Hβ and continuum emission indicate upper level populations of hydrogen in equilibrium with the electron concentration during the relaxation process. The expression for the rate constant for excitation of hydrogen by atom–atom collisions, that best fit the data was

$$k_{AA} = 4.0 \times 10^{-17} \left(\frac{8kT}{\pi\mu}\right)^{1/2} \exp\,(-10/kT)\,\mathrm{cm}^3\,\mathrm{sec}^{-1},$$

where it has been assumed that the excitation cross section is the same for hydrogen and helium collision partners. The electron–atom excitation rate constant,

$$k_3 = 7.5 \times 10^{-16} \left(\frac{8kT_e}{\pi\mu_e}\right)^{1/2} \exp\,(-10/kT_e)\,\mathrm{cm}^3\,\mathrm{sec}^{-1},$$

determined from this investigation, was in agreement with recent electron-beam cross section measurements.

LESH, J. R.

L03 **DSN Progress Report for May–June 1972: Accuracy of the Signal-to-Noise Ratio Estimator**

J. R. Lesh

Technical Report 32-1526, Vol. X, pp. 217–235,
August 15, 1972

In this article the effects of external and internal noise, finite sample size, and transition estimation errors are included in an analysis of the signal-to-noise ratio estimator used in the symbol-synchronizer assembly. Expressions for the estimator mean and variance are developed, from which their dependence on the above effects are determined. The results of this study show that the estimator mean depends almost entirely on the external and internal signal-to-noise ratios while the estimator variance depends almost exclusively on the sample size.

LEVY, R.

L04 **DSN Progress Report for May–June 1972: Repositioning of Parabolic Antenna Panels Onto a Shaped Surface**

R. Levy

Technical Report 32-1526, Vol. X, pp. 199–206,
August 15, 1972

Optimal parameters for shifting existing parabolic-reflector surface panels for re-use within shaped antenna configurations are determined from theory and equations given in this article. The panels are reset to minimize the rms half-pathlength differences between their surface and the ideal, shaped surface. Input, output, and results are described for a computer program that implements the equations. Results for typical 26- and 64-m-diameter antennas indicate that, if all or most of the existing parabolic panels are re-used and repositioned according to the procedure, the consequent rms differences will be small.

LEWICKI, G.

L05 **Barrier Energies in MIM Structures From Photoresponse: Effect of Scattering in the Insulating Film**

G. Lewicki, J. Maserjian, and C. A. Mead (California Institute of Technology)

J. Appl. Phys., Vol. 43, No. 4, pp. 1764–1767, April 1972

Scattering of electrons photoexcited into the insulator conduction band prevents photoresponse from following the Fowler relation in metal-insulator-metal (MIM) structures. However, barrier energies can be obtained without specific knowledge of the scattering process either by measuring the threshold for photoresponse directly, or by applying sufficiently large voltages across the insulator.

LINDSEY, W. C.

L06 Carrier Synchronization and Detection of Polyphase Signals

W. C. Lindsey (University of Southern California) and
M. K. Simon

IEEE Trans. Commun., Vol. COM-20, No. 3, pp. 441–454,
June 1972

Digital communication networks used for the distribution of high-speed digital information are currently the subject of design studies for many civil and military applications. This article presents results that are useful in such studies as well as in network planning. In particular, the article is concerned with the problems of carrier synchronization and noisy reference detection of polyphase signals. Reconstruction of coherent references for the detection of polyphase (*N*-ary phase-shift-keyed) signals is considered and analyzed for three carrier reconstruction loops, namely, *N*th power (multiply-and-divide) loops, generalized Costas (*I*–*Q*) loops, and extensions of data-aided (modulation wipeoff) loops. General expressions for the error probability are developed when the reconstructed reference signals are noisy. These expressions are evaluated numerically for cases of practical interest and compared with differentially coherent reception.

LINNES, K. W.

L07 DSN Progress Report for May–June 1972: Radio Science Support

K. W. Linnes

Technical Report 32-1526, Vol. X, pp. 52–58,
August 15, 1972

Since 1967, radio scientists have used the DSN 26- and 64-m-diameter antenna stations to investigate pulsars, to study the effect of solar corona on radio signals, and to observe radio emissions from X-ray sources. More recently, very-long-baseline interferometry

(VLBI) techniques have been used for high-resolution studies of quasars. During the reporting period, VLBI observations were made of quasars and pulsars. Support was also provided by the 64-m-diameter antenna for the measurement of cosmic background noise, mapping of nearby spiral galaxies, searching for ionized hydrogen in interstellar globular clusters, searching for interstellar molecules, and observing radiation from Jupiter.

LUDWIG, A. C.

L08 Gain Calibration of a Horn Antenna Using Pattern Integration

A. C. Ludwig, J. Hardy, and R. Norman

Technical Report 32-1572, October 1, 1972

A cooperative program between JPL and the National Bureau of Standards will result in the gain measurement of a horn antenna using three different techniques: a two-antenna insertion loss measurement, a pattern-integration method, and a near-field measurement method. This article describes the application of the pattern-integration method and the evaluation of the near-field gain correction factors for the horn, which are determined by a new method based directly on measured data. This method involves a spherical-wave expansion of the experimental radiation pattern of the specific antenna being tested, rather than evaluation of an assumed analytical model. The spherical-wave expansion is compared to experimental near-field pattern data.

The gain of the antenna is determined by the pattern-integration method to be 22.02 dB within a 3σ tolerance (or 99.7% confidence interval) of ±0.1 dB. It is concluded that the pattern-integration method is a valuable technique with a potential of even better accuracies with further development.

LUNDY, C. C.

L09 DSN Progress Report for May–June 1972: New Probes for Tracing Electrical Noise

C. C. Lundy

Technical Report 32-1526, Vol. X, pp. 194–198,
August 15, 1972

Stations of the DSN are vulnerable to many kinds of noise. This article describes three new designs of probes to discover and measure potentially harmful noise. The article also suggests design practices that defend the station against noise.

MacCLELLAN, R. N.

M01 **DSN Progress Report for May–June 1972: Novel 70-MHz Limiting Amplifier**

J. G. Leflang and R. N. MacClellan

Technical Report 32-1526, Vol. X, pp. 172–174, August 15, 1972

For abstract, see Leflang, J. G.

MacCONNELL, J.

M02 **DSN Progress Report for May–June 1972: L-Band Frequency Multipliers: Phase Noise, Stability, and Group Delay**

J. MacConnell and R. Meyer

Technical Report 32-1526, Vol. X, pp. 104–109, August 15, 1972

In this article, three 100- to 1400-MHz frequency multipliers are evaluated for use in the hydrogen-maser receiver–synthesizer, with the conclusion that significant advancements have been made in the design of step-recovery diode multipliers. In addition, while it appears that the group delay performance in multipliers can be quite good, there are substantial problems that prevent resolving group delays of <1 ns in frequency multipliers.

MARGOLIS, J. S.

M03 **Laboratory Simulation of Diffuse Reflectivity From a Cloudy Planetary Atmosphere**

J. S. Margolis, D. J. McCleese, and G. E. Hunt

Appl. Opt., Vol. 11, No. 5, pp. 1212–1216, May 1972

For the first time measurements in the multiple scattering regime of the diffuse reflectivity as a function of single scattering albedo have been made in a geometry that may be simulated by a plane parallel atmosphere of large optical depth. A comparison between the measurements and a theoretical computation of the diffuse reflectivity is presented. The measurements are within 1% agreement with the theoretical calculations for two different sizes of scattering particles which are larger than and smaller than the wavelength of the incident light, corresponding to the Mie and Rayleigh regimes, respectively.

M04 **Intensity and Half Width Measurements of the (00°2–00°0) Band of N_2O**

J. S. Margolis

J. Quant. Spectrosc. Radiat. Transfer, Vol. 12, No. 4, pp. 751–757, April 1972

Measurements of the intensities and half-widths of the lines of the (00°2–00°0) band of N_2O have been made with a spectral resolution $\leqslant 0.06$ cm^{-1}. The band intensity has been determined to be 1.29 cm^{-2} atm^{-1} at 296°K. The half-widths have been measured for both N_2- and self-broadened lines.

MASEK, T. D.

M05 ***Solar–Electric Propulsion Breadboard Thrust Subsystem***

T. D. Masek

JPL Quarterly Technical Review, Vol. 2, No. 2, pp. 100–112, July 1972

A solar–electric propulsion, breadboard, thrust subsystem has been designed, built, and tested. A 1500-h test was performed to demonstrate the functional capabilities of the subsystem. This report describes the subsystem functions and testing process. The results show that the ground work has been established for development of an engineering model of the thrust subsystem.

MASERJIAN, J.

M06 **Barrier Energies in MIM Structures From Photoresponse: Effect of Scattering in the Insulating Film**

G. Lewicki, J. Maserjian, and C. A. Mead (California Institute of Technology)

J. Appl. Phys., Vol. 43, No. 4, pp. 1764–1767, April 1972

For abstract, see Lewicki, G.

MASSIER, P. F.

M07 **An Anechoic Chamber Facility for Investigating Aerodynamic Noise**

P. F. Massier and S. P. Parthasarathy

Technical Report 32-1564, September 15, 1972

The aerodynamic-noise facility at JPL was designed to be used primarily for investigating the noise-generating mechanisms of high-temperature supersonic and subsonic jets. It can, however, be used for investigating other sources of noise as well. The facility consists of an anechoic chamber, an exhaust-jet silencer, instrumentation equipment, and an air heater with associated fuel and cooling systems. Compressed air, when needed for jet-noise studies, is provided by the wind tunnel compressor facility on a continuous basis.

The chamber is 8.1 m long, 5.0 m wide, and 3.0 m high. Provisions have been made for allowing outside air to be drawn into the anechoic chamber in order to replenish the air that is entrained by the jet as it flows through the chamber. Also, openings are provided in the walls and in the ceiling for the purpose of acquiring optical measurements. The chamber was calibrated for noise reflections from the wall in octave bands between 31.2 Hz and 32 kHz.

MATHUR, F. P.

M08 A Brief Description and Comparison of Programming Languages FORTRAN, ALGOL, COBOL, PL/I, and LISP 1.5 From a Critical Standpoint

F. P. Mathur

Technical Memorandum 33-566, September 15, 1972

This report describes and compares several common higher-level programming languages, FORTRAN, ALGOL, COBOL, PL/I, and LISP 1.5. FORTRAN is the most widely used scientific programming language, however ALGOL is a more powerful language. COBOL is used for most commercial programming applications, and LISP 1.5 is primarily a list-processing language. PL/I attempts to combine the desirable features of FORTRAN, ALGOL, and COBOL into a single language.

M09 Phase 1 Report on a Cognitive Operating System (COGNOSYS) for JPL's Robot

F. P. Mathur

Technical Memorandum 33-568, September 15, 1972

The most important software requirement for any robot development is the COGNitive Operating SYStem (COGNOSYS). This memorandum describes the Stanford University Artificial Intelligence Laboratory's Hand/Eye software system from the point of view of developing a cognitive operating system for JPL's Robot. In this Phase I report of the JPL robot COGNOSYS task, the installation of a SAIL compiler and a FAIL assembler on Caltech's PDP-10 are described, and guidelines are given for the implementation of a Stanford-University-type Hand/Eye software system in

JPL-Caltech's computing facility. The alternatives offered by using RAND-USC's PDP-10 Tenex operating system are also considered.

MCCLEESE, D. J.

M10 Laboratory Simulation of Diffuse Reflectivity From a Cloudy Planetary Atmosphere

J. S. Margolis, D. J. McCleese, and G. E. Hunt

Appl. Opt., Vol. 11, No. 5, pp. 1212–1216, May 1972

For abstract, see Margolis, J. S.

McINNIS, J. H., JR.

M11 DSN Progress Report for May–June 1972: DSN/MSFN Antenna-Pointing and Tracking Implementation

J. H. McInnis, Jr.

Technical Report 32-1526, Vol. X, pp. 153–156,
August 15, 1972

The antenna-pointing and tracking-data processing functions at the three DSN/Manned Space Flight Network joint-usage ("wing") tracking stations have been altered to implement a commonality between the two networks. The changes affect both hardware and software and produce station configurations that differ from those of other DSN stations.

MEAD, C. A.

M12 Barrier Energies in MIM Structures From Photoresponse: Effect of Scattering in the Insulating Film

G. Lewicki, J. Maserjian, and C. A. Mead (California Institute of Technology)

J. Appl. Phys., Vol. 43, No. 4, pp. 1764–1767, April 1972

For abstract, see Lewicki, G.

MEEKS, W. G.

M13 DSN Progress Report for May–June 1972: Initial Acquisition Planning

W. G. Meeks

Technical Report 32-1526, Vol. X, pp. 236–242,
August 15, 1972

Each spacecraft supported by the DSN must be acquired and tracked by a deep space station. The first acquisition, generally referred to as initial acquisition, is unique for each spacecraft and presents problems that must be recognized and resolved long before a launch actually takes place. This article describes how plans are developed and implemented to ensure the successful beginning of DSN tracking support.

MENICHELLI, V. J.

M14 Terminated Capacitor-Discharge Firing of Electroexplosive Devices

L. A. Rosenthal (Rutgers University) and V. J. Menichelli

IEEE Trans. Instr. Meas., Vol. IM-21, No. 2, pp. 177–180,
May 1972

For abstract, see Rosenthal, L. A.

MEYER, R.

M15 DSN Progress Report for May–June 1972: L-Band Frequency Multipliers: Phase Noise, Stability, and Group Delay

J. MacConnell and R. Meyer

Technical Report 32-1526, Vol. X, pp. 104–109,
August 15, 1972

For abstract, see MacConnell, J.

MOYNIHAN, P. I.

M16 A Portable Hydrazine Attitude Propulsion Test System

P. I. Moynihan

Technical Memorandum 33-560, September 1, 1972

This report describes the portable hydrazine attitude-propulsion module that was designed and developed to support the attitude-control pitch axis simulation tests that were performed on an air-bearing table in JPL's Celestarium facility for the Thermoelectric Outer-Planet Spacecraft program. The propulsion module was a self-contained, liquid-hydrazine propulsion system from which the exhaust gases were generated within the catalyst bed of either of two nominal 0.22-N (0.05-lbf) opposing thrusters. The module, which was designed for convenient assembly onto and removal from an air-bearing table in the JPL Celestarium, was tested extensively to establish its operational safety. This test history and the very conservative design of the module enabled it to be "man-rated" for operation in the presence of personnel. The report briefly summarizes the system operations during air-bearing table tests, presents a detailed description of the propulsion module hardware, and discusses the system evolution.

M17 Small Rocket Exhaust Plume Data

J. E. Chirivella, P. I. Moynihan, and W. Simon

JPL Quarterly Technical Review, Vol. 2, No. 2, pp. 90–99, July 1972

For abstract, see Chirivella, J. E.

MUDGWAY, D. J.

M18 DSN Progress Report for May–June 1972: Viking Mission Support

D. J. Mudgway

Technical Report 32-1526, Vol. X, pp. 22–26, August 15, 1972

A previous article identified the probable impact of changes in the scope of the DSN to Flight Project interfaces for Viking. In this article the outcome of the changes is described in the areas of DSN configuration, interfaces, schedules, documentation, and organization in order to establish a background against which subsequent articles can report progress in each of these particular areas.

M19 DSN Progress Report for May–June 1972: Mariner Jupiter-Saturn 1977 Mission Support

D. J. Mudgway

Technical Report 32-1526, Vol. X, pp. 35–40, August 15, 1972

The Mariner Jupiter-Saturn 1977 Project has recently been formally established as a Flight Project. The mission calls for the launch of two Mariner-class spacecraft in 1977 to fly by Jupiter and Saturn. Flight times to Jupiter and Saturn are approximately 2 and 4 yr, respectively. The primary scientific objectives of the missions are to explore Jupiter, Saturn, and their satellites, and to investigate the nature of the interplanetary medium. Engineering objectives include the operation of a Mariner-class of spacecraft in space for periods of 4 yr, use of radioisotope thermoelectric generators as the primary power source, and a demonstration of communications and navigational accuracy out to 10 AU.

Support from the 26-m-diameter antenna subnet is required intermittently during the long cruise periods with 64-m-diameter antenna support covering the encounters. Navigation support will require S–X planetary ranging, S–X doppler, and differenced range versus integrated doppler and will be planned around complete "cycles" of data. The number of "cycles" per week will vary with the phases of the mission.

The Office of Computing and Information Systems organization will be responsible for the hardware, software, and simulation needed by the Mission Operations System to carry out the mission. This article provides an introduction to the mission requirements as presently understood.

NEUGEBAUER, M.

N01 Dissipation Mechanisms in a Pair of Solar-Wind Discontinuities

T. W. J. Unti, G. Atkinson (Communications Research Center), C.-S. Wu (University of Maryland), and M. Neugebauer

J. Geophys. Res., Space Physics, Vol. 77, No. 13, pp. 2250–2263, May 1, 1972

For abstract, see Unti, T. W. J.

NICOLET, M.-A.

N02 Thermal Noise in Space-Charge-Limited Hole Current in Silicon

A. Shumka, J. Golder, and M.-A. Nicolet

JPL Quarterly Technical Review, Vol. 2, No. 2, pp. 72–76, July 1972

For abstract, see Shumka, A.

NOGUCHI, H.

N03 Reactions of N,N,N′,N′-Tetramethyl-α,ω-Diaminoalkanes With α,ω-Dihaloalkanes: I. 1–y Reactions

H. Noguchi and A. Rembaum

Macromolecules, Vol. 5, No. 3, pp. 253–260, May–June 1972

The reactions of *N,N,N′,N′*-tetramethyldiaminomethane with a number of α,ω-dihaloalkanes were investigated in dimethylformamide (DMF), DMF–methanol (1:1 by volume), and acetonitrile. The most important products of these reactions consisted of dimethylaminohaloalkanes, dimethylamine hydrohalides, cyclic and linear mono- and diammonium salts, as well as polyelectrolytes. The course of the reaction was influenced by the solvent. The reaction of tetramethyldiaminomethane with 1,4-dibromobutane yielded unexpectedly in DMF–methanol a linear diammonium compound containing two methoxy groups. A mechanism accounting for the reaction products is proposed and experimental evidence for the isolated compounds is presented.

N04 **Reactions of N,N,N′,N′-Tetramethyl-α,ω-Diaminoalkanes With α,ω-Dihaloalkanes: II. x–y Reactions**

A. Rembaum and H. Noguchi

Macromolecules, Vol. 5, No. 3, pp. 261–269, May–June 1972

For abstract, see Rembaum, A.

NORMAN, R.

N05 **Gain Calibration of a Horn Antenna Using Pattern Integration**

A. C. Ludwig, J. Hardy, and R. Norman

Technical Report 32-1572, October 1, 1972

For abstract, see Ludwig, A. C.

OLIVER, R. E.

O01 **Large Spacecraft Antennas: Conical Ring-Membrane Reflectors**

R. E. Oliver, M. R. Trubert, and A. H. Wilson

JPL Quarterly Technical Review, Vol. 2, No. 2, pp. 42–47, July 1972

A 1.83-m- (6-ft-) diameter, furlable, conical, Gregorian antenna based on a novel spoke-supported ring-membrane concept has been successfully demonstrated. Mechanical measurements of the conical reflecting surface, as well as RF gain measurements at Ku-band, show an rms surface deviation from the proper conical surface of 0.3 mm (0.012 in.), and a repeatability after multiple furling-unfurling cycles of ±0.05 mm (0.002 in.). Design features and performance characteristics of this antenna indicate that the spoke-supported ring-membrane concept is a promising approach for producing large, furlable, lightweight, conical reflectors for spacecraft high-gain antennas.

OLSON, R. L.

002 A Re-evaluation of Material Effects on Microbial Release From Solids

D. M. Taylor, S. J. Fraser (The Boeing Company), E. A. Gustan (The Boeing Company), R. L. Olson (The Boeing Company), and R. H. Green

Life Sciences and Space Research X, Vol. 10, pp. 23–28, Akademie-Verlag, Berlin, 1972

For abstract, see Taylor, D. M.

ONDRASIK, V. J.

003 DSN Progress Report for May–June 1972: Preliminary Evaluation of Radio Data Orbit Determination Capabilities for the Saturn Portion of a Jupiter–Saturn–Pluto 1977 Mission

V. J. Ondrasik, C. E. Hildebrand, and G. A. Ransford

Technical Report 32-1526, Vol. X, pp. 59–75, August 15, 1972

This article investigates the navigation accuracies attainable with radio tracking of an outer-planets spacecraft in the vicinity of Saturn. Analysis of the results indicates that navigation-accuracy problems associated with low spacecraft declinations and with batch filtering of conventional radio data when unmodeled accelerations are acting on the spacecraft may be avoided by employing range and range-rate data taken simultaneously by two widely separated stations. With the availability of two-station simultaneous data, the uncertainty in Saturn's ephemeris becomes the error source which limits the accuracy of the pre-encounter navigation.

004 DSN Progress Report for May–June 1972: Determining the Mass and Ephemeris of Saturn by Radio Tracking of a Jupiter–Saturn–Pluto 1977 Spacecraft

V. J. Ondrasik, C. E. Hildebrand, and G. A. Ransford

Technical Report 32-1526, Vol. X, pp. 76–81,
August 15, 1972

This article presents preliminary estimates of the accuracies with which the mass and ephemeris of Saturn may be determined from radio tracking of an outer-planets spacecraft. It is shown that the determination of these parameters should employ radio metric data taken simultaneously from two stations. Indications are that the uncertainties in the mass and the ephemeris may be reduced by approximately three orders of magnitude for the mass and by a factor of two for the ephemeris.

OTOSHI, T. Y.

O05 DSN Progress Report for May–June 1972: Error Analysis of Precision Calibrations of Perforated Plate Mesh Materials on a Tuned Reflectometer System

T. Y. Otoshi

Technical Report 32-1526, Vol. X, pp. 143–148,
August 15, 1972

This article presents an error analysis of a waveguide technique for precision reflectivity-loss measurements of perforated-plate mesh materials useful for antenna surfaces, dichroic plates, or RF shields. It is shown that by use of a prescribed experimental procedure, the maximum reflectivity-loss measurement error due to imperfect system tuning can typically be kept to less than ±0.002 dB.

PACE, G. D.

P01 Scan Pointing Calibration for the Mariner Mars 1971 Spacecraft

W. F. Havens, G. I. Jaivin, G. D. Pace, and R. A. Virzi

Technical Memorandum 33-556, August 1, 1972

For abstract, see Havens, W. F.

PALLUCONI, F. D.

P02 Models for the Atmospheres of Jupiter and Saturn

N. Divine and F. D. Palluconi

JPL Quarterly Technical Review, Vol. 2, No. 2, pp. 1–8,
July 1972

For abstract, see Divine, N.

PARTHASARATHY, S. P.

P03 An Anechoic Chamber Facility for Investigating Aerodynamic Noise

P. F. Massier and S. P. Parthasarathy

Technical Report 32-1564, September 15, 1972

For abstract, see Massier, P. F.

PETTY, S.

P04 DSN Progress Report for May–June 1972: Tracking and Ground Based Navigation: Performance of Hydrogen Maser Cavity Tuning Servo

S. Petty and C. Finnie

Technical Report 32-1526, Vol. X, pp. 113–115,
August 15, 1972

An experimental automatic cavity tuner has been demonstrated with the atomic hydrogen-maser frequency standards developed by JPL. The ability of this tuner to prevent RF-cavity frequency drift in the maser is shown, and the methods used to modulate hydrogen transition line width in the maser during tuner operation are compared.

POTTER, P. D.

P05 DSN Progress Report for May–June 1972: Antenna Study: Performance Enhancement

P. D. Potter

Technical Report 32-1526, Vol. X, pp. 129–134,
August 15, 1972

A study of possible Mars Deep Space Station (DSS 14) 64-m-diameter antenna gain improvement by utilizing existing dual-reflector shaping techniques has been previously published. That study was restricted to the case of axially-symmetric (unicone) initial 64-m-diameter antenna configuration. After installation of the asymmetrical tricone system, studies of shaping techniques were discontinued pending operational experience with the tricone system at S- and X-bands, and development of new analytical tools for design and analysis of asymmetrical-shape reflector systems. The required analytical tools have been developed recently and are described in this article.

P06 **DSN Progress Report for May–June 1972: Network Engineering and Implementation: S- and X-Band Feed System**

P. D. Potter

Technical Report 32-1526, Vol. X, pp. 135–142,
August 15, 1972

In support of the Mariner Venus–Mercury 1973 X-band experiment, it is necessary to implement a dual-frequency microwave feed system for the Mars Deep Space Station (DSS 14) 64-meter-diameter antenna. To fulfill this requirement, a particularly attractive approach, the reflex feed system, is being implemented. The reflex feed configuration and its calculated aperture efficiency performance were described in a previous report. Additionally, calculated RF power dissipation data for the reflex feed were reported. In this article, two questions are analyzed: (1) the S-band effects of possible buckling of the dichroic flat plate caused by RF and solar heating, and (2) the effect of subreflector backscatter on the S-band focus characteristics of the antenna.

PURDUE, R. E.

P07 **Tracking and Data System Support for the Pioneer Project: Pioneers 6–9. Extended Missions: July 1, 1970–July 1, 1971**

A. J. Siegmeth, R. E. Purdue, and R. E. Ryan

Technical Memorandum 33-426, Vol. X, August 15, 1972

For abstract, see Siegmeth, A. J.

RANSFORD, G. A.

R01 **DSN Progress Report for May–June 1972: Preliminary Evaluation of Radio Data Orbit Determination Capabilities for the Saturn Portion of a Jupiter–Saturn–Pluto 1977 Mission**

V. J. Ondrasik, C. E. Hildebrand, and G. A. Ransford

Technical Report 32-1526, Vol. X, pp. 59–75,
August 15, 1972

For abstract, see Ondrasik, V. J.

R02 **DSN Progress Report for May–June 1972: Determining the Mass and Ephemeris of Saturn by Radio Tracking of a Jupiter–Saturn–Pluto 1977 Spacecraft**

V. J. Ondrasik, C. E. Hildebrand, and G. A. Ransford

Technical Report 32-1526, Vol. X, pp. 76–81, August 15, 1972

For abstract, see Ondrasik, V. J.

RAY, R. L.

R03 Long-Term Storage Test of a SYNCOM Solid Rocket Motor

R. L. Ray

JPL Quarterly Technical Review, Vol. 2, No. 2, pp. 77–82, July 1972

After 7.5 yr of storage at ambient temperature, a solid-propellant apogee motor was tested successfully at the Air Force Rocket Propulsion Laboratory. The performance of the motor had not deteriorated as a result of prolonged storage. Tabular performance data and graphic thrust and pressure variations are given.

REA, D. G.

R04 Topical Reviews: Composition of the Upper Clouds of Venus

D. G. Rea

Rev. Geophys. Space Phys., Vol. 10, No. 1, pp. 369–378, February 1972

Recent developments have shed new light on the composition of the upper Venus clouds. An analysis of the Mariner 5 occultation data has led to improved temperature and pressure profiles. When these are combined with transit data, it is concluded that there is an optically thin cloud layer with a top at 81-km altitude where the temperature and pressure are, respectively, 175°K and 3 mb. The inclusion of temperatures derived from the near-infrared CO_2 bands leads to the postulate of a second cloud deck with a top at 61-km altitude, where the temperature is 260°K and the pressure is 240 mb. Additional important constraints on cloud models are imposed by the measured abundances of HCl and H_2O, by the polarization data, and by the reflection and emission spectra. It is concluded that the leading candidate for the uppermost clouds is liquid drops of HCl-H_2O, that there is no recommended candidate for the second cloud deck, and that H_2O ice is at most a minor component of these cloud systems.

REID, M. S.

R05 **DSN Progress Report for May–June 1972: Tracking and Ground Based Navigation: A Description of the Weather Project**

M. S. Reid

Technical Report 32-1526, Vol. X, pp. 116–122,
August 15, 1972

The Weather Project forms part of an overall Radio Systems Development Project which seeks to optimize the spacecraft-to-ground communications link. In order to meet the future requirements of the planetary exploration program, a study of weather-dependent characteristics of X- and K-band propagation through the atmosphere is imperative. The objective of the Weather Project is, therefore, the statistical prediction of the performance of the DSN at X-band, and in the future at K-band.

This article discusses the general approach of the Weather Project, the measurements, the calibrations, the equipment, and the methods. Problems encountered are also discussed as well as the proposed future work.

R06 **DSN Progress Report for May–June 1972: Improved RF Calibration Techniques: System Operating Noise Temperature Calibrations**

M. S. Reid

Technical Report 32-1526, Vol. X, pp. 123–128,
August 15, 1972

System operating noise temperatures and other calibration data of the S-band radar operational cone at the Venus Deep Space Station (DSS 13) and the tricone system at the Mars Deep Space Station (DSS 14) are reported for the period February 1 through May 31, 1972. During this reporting period the tricone system consisted of the polarization-diversity S-band (PDS) cone, the S-band megawatt transmit (SMT) cone and the multifrequency X- and K-band (MXK) cone. S-band calibration data for various configuration modes of the PDS and SMT cones are reported as well as X-band calibration data for the MXK cone.

REMBAUM, A.

R07 **Superconductivity in the Alkali Metal Intercalates of Molybdenum Disulphide**

R. B. Somoano, V. Hadek, and A. Rembaum

JPL Quarterly Technical Review, Vol. 2, No. 2, pp. 83–89, July 1972

For abstract, see Somoano, R. B.

R08 **Reactions of N,N,N′,N′-Tetramethyl-α,ω-Diaminoalkanes With α,ω-Dihaloalkanes: I. 1–y Reactions**

H. Noguchi and A. Rembaum

Macromolecules, Vol. 5, No. 3, pp. 253–260, May–June 1972

For abstract, see Noguchi, H.

R09 **Reactions of N,N,N′,N′-Tetramethyl-α,ω-Diaminoalkanes With α,ω-Dihaloalkanes: II. x–y Reactions**

A. Rembaum and H. Noguchi

Macromolecules, Vol. 5, No. 3, pp. 261–269, May–June 1972

The reactions of *N,N,N′,N′*-tetramethyl-1,2-diaminoethane, -1,3-diaminopropane, -1,4-diaminobutane, and -1,6-diaminohexane with a number of α,ω-dibromoalkanes were investigated in solution. The main products of these reactions consisted of cyclic diammonium compounds (1:1 addition), linear diammonium compounds (1:2 addition), and ionene polymers (polyaddition). The conditions under which these products are formed as well as the information described in Part I permit one to conclude that the reactions of tetramethyldiaminoethane with dibromobutane and of tetramethyldiaminopropane with dibromopropane yield ionene polymers with the highest known density of positive charges in a polymer backbone. The reaction of tetramethyldiaminobutane with dibromomethane in dimethylformamide–methanol (1:1 by volume) yielded unexpectedly tetramethyldiaminobutane dihydrobromide, indicating participation of methanol in the reaction. Elucidation of these results as well as experimental evidence for the isolated products is presented.

RENZETTI, N. A.

R10 **DSN Progress Report for May–June 1972: DSN Functions and Facilities**

N. A. Renzetti

Technical Report 32-1526, Vol. X, pp. 1–4,
August 15, 1972

The Deep Space Network (DSN), established by the NASA Office of Tracking and Data Acquisition and under the system management and technical direction of JPL, is designed for two-way communications and unmanned spacecraft traveling approximately 16,000 km (10,000 mi) from earth to planetary distances. The objectives, functions, and organization of the DSN are summarized, and its three facilities—the Deep Space Instrumentation Facility, the Ground Communications Facility, and the Space Flight Operations Facility—are described.

RHO, J. H.

R11 Direct Fluorometric Determination of Urea in Urine

J. H. Rho

Clinical Chem., Vol. 18, No. 5, pp. 476–478, 1972

In this quantitative fluorometric method, diacetylmonoxime is used for the determination of the urea. The products of the reaction of urea with diacetylmonoxime in acid solution exhibit two fluorescence maxima, at 410 and 525 nm. The intensity of the 525-nm maximum is linear over a wide range of urea concentration and the reaction is shown to be practically specific for urinary urea.

ROBINSON, E. Y.

R12 A Basic Model for Acoustic Emission From Fiber-Reinforced Material

E. Y. Robinson

Technical Memorandum 33-564, September 1, 1972

Acoustic emission from fiber-reinforced composites can often be conveniently interpreted by use of normalized coordinates in graphical data display. Many aspects of the shape of the acoustic-emission pattern are invariant with the signal-amplification ratio, and the use of normalized coordinates allows simultaneous comparison of acoustic-emission pattern shapes from different experiments. In this paper, the first order model of acoustic emission from fiber composites, based on filament breaking rates, is cast into a normalized form useful for correlating experimental data. The general features of the normalized model are shown and compare favorably with available data.

R13 On the Elastic Properties of Fiber Composite Laminates With Statistically Dispersed Ply Orientation

E. Y. Robinson

JPL Quarterly Technical Review, Vol. 2, No. 2, pp. 48–60, July 1972

Structural application of advanced composite filamentary materials requires lamination of the basic orthotropic plies into "angle-ply" laminates. The resulting elastic and strength properties depend on the pattern of orientation and are influenced by inevitable errors and inaccuracy in placement of the angle plies. Misorientation results also from irregular displacements following processing at elevated temperatures.

This article reviews the effect of orientation dispersion on laminate elastic properties. The conventional constitutive relations are recast in a homologous form to account for orientation dispersion by addition of a single parameter. Graphical results are presented to show the behavior of the most important advanced composite materials. These results are useful for estimating effects of manufacturing inaccuracy and for design of partially oriented reinforced structures.

ROSCHKE, E. J.

R14 Experimental Investigation of Heat Transfer From Partially Ionized Argon With an Applied Transverse Magnetic Field

E. J. Roschke

Trans. ASME, Ser. C: J. Heat Transf., Vol. 94, No. 2, pp. 174–180, May 1972

Wall heat transfer measurements were obtained for laminar flow of partially ionized argon flowing within the conducting walls of a square channel, with and without an applied transverse magnetic field. Tests were conducted for subsonic flows and for flows which were supersonic before a magnetic field was applied. Increases in Stanton number by a factor of as much as six were observed at field strengths approaching 10 kG as compared to values at zero magnetic field. These large increases in heat transfer are believed to have been due to (1) a small amount of joule heating augmented or accompanied by (2) magnetically induced ionization. Heat transfer and flow data were used to estimate effective values of the joule heating parameter, Hall coefficient, and current density. The experimental data have been compared to theoretical predictions for several limiting cases.

ROSENTHAL, L. A.

R15 Terminated Capacitor-Discharge Firing of Electroexplosive Devices

L. A. Rosenthal (Rutgers University) and V. J. Menichelli

IEEE Trans. Instr. Meas., Vol. IM-21, No. 2, pp. 177–180, May 1972

By terminating the discharge of energy into an insensitive electroexplosive device, firing-energy parameters can be determined. A simple capacitor-discharge system providing exponential pulses terminated at an adjustable width is described. Basic theory and application to testing are discussed.

ROSS, R. G., JR.

R16 Summary Report on the Development, Design and Test of a 66-W/kg (30-W/lb) Roll-Up Solar Array

W. A. Hasbach and R. G. Ross, Jr.

Technical Report 32-1562, September 15, 1972

For abstract, see Hasbach, W. A.

RYAN, R. E.

R17 Tracking and Data System Support for the Pioneer Project: Pioneers 6–9. Extended Missions: July 1, 1970–July 1, 1971

A. J. Siegmeth, R. E. Purdue, and R. E. Ryan

Technical Memorandum 33-426, Vol. X, August 15, 1972

For abstract, see Siegmeth, A. J.

SHUMKA, A.

S01 Thermal Noise in Space-Charge-Limited Hole Current in Silicon

A. Shumka, J. Golder, and M.-A. Nicolet

JPL Quarterly Technical Review, Vol. 2, No. 2, pp. 72–76, July 1972

Present theories on noise in single-carrier space-charge-limited currents in solids have not been quantitatively substantiated by experimental evidence. To obtain such experimental verification, the noise in specially fabricated silicon structures is being measured and analyzed. The first results of this verification effort are reported in this article.

SIEGMETH, A. J.

S02 **DSN Progress Report for May–June 1972: Pioneer 6–9 Mission Support**

A. J. Siegmeth

Technical Report 32-1526, Vol. X, pp. 10–13,
August 15, 1972

To meet the specific scientific objectives of the Pioneer 10 and G missions, the importance of the simultaneous support of the still-active Pioneers 6–9 has increased. The Pioneer Project requires tracks during the radial- and spiral-type configurations of the Pioneer 8, 9, and 10 missions. Fields and particles data acquired by DSN will make possible the measurement of distribution gradients. This article gives a description of the radial and spiral configurations and opportunities and the support requirements.

S03 **DSN Progress Report for May–June 1972: Pioneer 10 and G Mission Support**

A. J. Siegmeth

Technical Report 32-1526, Vol. X, pp. 27–34,
August 15, 1972

The DSN has already furnished more than four months of continuous data acquisition and command support for Pioneer 10, launched on March 3, 1972. After the description of the new DSN/Flight Project interface, a brief review of the qualitative and quantitative performance of the DSN's data recovery support is presented.

S04 **DSN Progress Report for May–June 1972: Pioneer Venus Mission Support**

A. J. Siegmeth

Technical Report 32-1526, Vol. X, pp. 49–51,
August 15, 1972

The DSN has advanced capabilities which can be used for spaceflight missions to Venus. This article summarizes a presentation given to the Pioneer Venus study team on the ranging and S/X-band systems, which can enhance the navigational accuracy of deep-space missions.

S05 **Tracking and Data System Support for the Pioneer Project: Pioneers 6–9. Extended Missions: July 1, 1970–July 1, 1971**

A. J. Siegmeth, R. E. Purdue, and R. E. Ryan

Technical Memorandum 33-426, Vol. X, August 15, 1972

The Tracking and Data System supported the deep space phases of the Pioneer 6, 7, 8, and 9 missions, with two spacecraft in an inward trajectory and two spacecraft in an outward trajectory from the Earth in heliocentric orbits. During the period of this report, scientific instruments aboard each of the spacecraft continued to register information relating to interplanetary particles and fields, and radio metric data generated by the network continued to improve our knowledge of the celestial mechanics of the solar system. In addition to network support activity detail, network performance and special support activities are covered.

SIMON, M. K.

S06 **On the Selection of a Sampling Filter Bandwidth for a Digital Data Detector**

M. K. Simon

IEEE Trans. Commun., Vol. COM-20, No. 3, pp. 438–441, June 1972

This article discusses the problem of selecting the low-pass sampling bandwidth for a digital mechanization of a matched-filter bit-synchronizer combination. In particular, if digital data at a rate R bits/s plus gaussian noise is passed through a filter of bandwidth KR and then sampled at the Nyquist rate, i.e., $2KR$, then how small can K be without paying an appreciable penalty in the signal-to-noise ratio performance of the data detector?

S07 **Carrier Synchronization and Detection of Polyphase Signals**

W. C. Lindsey (University of Southern California) and M. K. Simon

IEEE Trans. Commun., Vol. COM-20, No. 3, pp. 441–454, June 1972

For abstract, see Lindsey, W. C.

SIMON, W.

S08 **Small Rocket Exhaust Plume Data**

J. E. Chirivella, P. I. Moynihan, and W. Simon

JPL Quarterly Technical Review, Vol. 2, No. 2, pp. 90–99, July 1972

For abstract, see Chirivella, J. E.

SOMOANO, R. B.

S09 Superconductivity in the Alkali Metal Intercalates of Molybdenum Disulphide

R. B. Somoano, V. Hadek, and A. Rembaum

JPL Quarterly Technical Review, Vol. 2, No. 2, pp. 83–89, July 1972

The complete series of alkali metals, lithium through cesium, has been intercalated into molybdenum disulphide, using both the liquid-ammonia and vapor techniques. All the intercalates, with the exception of lithium, yielded full superconducting transitions with onset temperatures of 6 K for $A_x\mathrm{MoS}_2$ (A_x = K,Rb,Cs) and 4 K for $B_x\mathrm{MoS}_2$ (B_x = Li,Na). The superconducting transition for lithium was incomplete down to 1.5 K. Stoichiometries and unit-cell parameters have been determined for the intercalation compounds. Both rhombohedral and hexagonal polymorphs of MoS_2 have been intercalated and found to exhibit the same superconductivity behavior. The nature of the extraneous superconducting transition of some intercalated samples on exposure to air was elucidated.

STEARNS, J. W.

S10 Elements of Cost Comparison for Planetary Missions With Advanced Propulsion

J. W. Stearns

Technical Memorandum 33-553, July 1, 1972

Cost and performance comparisons are made between chemical propulsion and nuclear-electric propulsion for planetary missions to Jupiter and beyond. Nuclear rocket comparisons are made for performance only. Titan, Saturn, and Space Shuttle launches, utilizing advanced propulsion upper stages, are evaluated. Appendixes include a performance analysis of multiple Shuttle launches with assembly in Earth orbit and a discussion of nonrecurring costs.

STEIN, C. K.

S11 DSN Progress Report for May–June 1972: DSN System Testing: A Critical Review of the Pioneer 10 Test Program

C. K. Stein

Technical Report 32-1526, Vol. X, pp. 207–209,
August 15, 1972

The Pioneer 10 test program was unique since the majority of DSN testing was conducted during the Mariner 9 encounter and orbiting. The importance of both programs to the NASA effort required special emphasis to assure that successful programs can be supported simultaneously. This critique lists the major problems encountered and the solutions used for a successful Pioneer 10 launch, while fully supporting all Mariner Mars 1971 requirements.

STICKFORD, G. H., JR.

S12 Detailed Measurements of the Hβ Line Shape in a Transient Plasma Using a Fiber Optics Slit System

G. H. Stickford, Jr.

Preprint 72-106, AIAA Tenth Aerospace Sciences Meeting,
San Diego, California, January 17–19, 1972

Through the use of fiber optics, a series of very narrow slits have been constructed and placed at the exit plane of a spectrograph. Plasma radiation which is dispersed by the spectrograph is incident on the slits and is transmitted to separate phototubes via the quartz fibers. With this technique, time resolved measurements of the spectral shape of the hydrogen Hβ line have been made and used to determine the electron density of a transient plasma. Data obtained in a shock tube indicated that the thermodynamic conditions behind the reflected shock in a mixture of 20% H_2 and 80% He, at incident shock speeds of 12 to 14 km/s and pressures of 66.6 to 133.3 N/m^2 (0.5 to 1.0 mm Hg), correspond to theoretically predicted conditions. Immediately behind the incident shock at speeds of 17 to 24 km/s the data indicate that the plasma reached equilibrium and then demonstrated a drop in intensity which has been attributed to radiative cooling.

S13 Total Radiative Intensity Calculations for 100% H_2 and 87% H_2–13% He

G. H. Stickford, Jr.

J. Quant. Spectrosc. Radiat. Transfer, Vol. 12, No. 4,
pp. 525–529, April 1972

Isothermal radiative intensity calculations for 100% H_2 and 87% H_2–13% He are presented for temperatures of 10,000–25,000°K, density ratios of 10^{-4}–10^{-1}, and path lengths of 1.0–30.0 cm. The actual spectral details of the absorption coefficient were computed for 16,000 points from 240 to 30,000 Å by summing the various line and continuum radiative processes at each point. This method should result in a very accurate calculation of radiative emission, including an accurate accounting for re-absorption due to overlapping lines.

STINNETT, W. G.

S14 DSN Progress Report for May–June 1972: DSN Command System Performance Evaluation

W. G. Stinnett

Technical Report 32-1526, Vol. X, pp. 213–216,
August 15, 1972

This article presents a general performance description of the DSN Command System as configured for support of the Mariner Mars 1971 and Pioneer 10 missions. Included are statistics related to system reliability and availability. A comparison of command activity is presented for previous Mariner- and Pioneer-type missions.

STIRN, R. J.

S15 Junction Characteristics of Silicon Solar Cells: Nonilluminated Case

R. J. Stirn

Technical Memorandum 33-557, Pt. I, August 15, 1972

This report presents precise values of the reverse saturation currents in 2- and 10-Ω-cm silicon solar cells and magnitudes of the diffusion and recombination components. The recombination current as well as leakage current due to shunting are shown to be nonuniform across the cell. The diffusion lengths calculated from the diffusion current components agree well with diffusion lengths measured independently in similar material. Models are presented demonstrating the effect of recombination and shunting currents on the dark current–voltage characteristics of solar cells.

TAHERZADEH, M.

T01 The Response of a 0.03-cm Silicon Detector to a Mixed Neutron and Gamma Field as a Function of Shield Material and Thickness

M. Taherzadeh

JPL Quarterly Technical Review, Vol. 2, No. 2, pp. 25–41, July 1972

The neutron and gamma radiation from a multi-hundred-watt radioisotope thermoelectric generator was used to evaluate the total response of a shielded 0.3-mm silicon detector. The generator employs a 2200-W(th) PuO_2 heat source concept known as the Helipak. The total integrated neutron and gamma ray fluxes at 100 cm away from the source along the radial direction were 1.67×10^3 n/cm^2/s and 1.49×10^4 γ/cm^2/s, respectively. Experimental values of the response function of the shielded silicon detector were used to determine the total counting rates due to photons at bias energies ranging from 50 to 200 keV. For neutrons, analytically computed response functions were used to determine the total counting rates at the same bias energies.

It was found that for an aluminum shield the neutrons are not significant, regardless of the thickness of the shield. However, the magnitude of the total counting rate due to neutrons increases with increased atomic number of the shield and becomes comparable to the counting rate due to photons for a platinum-shield thickness of 5 cm.

TAUSWORTHE, R. C.

T02 Simplified Formula for Mean Cycle-Slip Time of Phase-Locked Loops With Steady-State Phase Error

R. C. Tausworthe

IEEE Trans. Commun., Vol. COM-20, No. 3, pp. 331–337, June 1972

Previous work has shown that the mean time from lock to a slipped cycle of a phase-locked loop is given by a certain double integral. Accurate numerical evaluation of this formula for the second-order loop has proved extremely vexing because the difference between exponentially large quantities is involved. This article simplifies the general formula to avert this problem, provides a useful approximation to a needed conditional expectation, and produces an asymptotic formula for the mean slip time that is moderately accurate even at low loop signal-to-noise ratios (less than 7 dB) and small steady-state phase errors (less than 0.3 rad). The approximations extend to higher order loops as well.

TAYLOR, D. M.

T03 A Re-evaluation of Material Effects on Microbial Release From Solids

D. M. Taylor, S. J. Fraser (The Boeing Company), E. A. Gustan (The Boeing Company), R. L. Olson (The Boeing Company), and R. H. Green

Life Sciences and Space Research X, Vol. 10, pp. 23-28, Akademie-Verlag, Berlin, 1972

A previous report concerned with the percentage of microbial release from the interior of solid materials after hard impact, raised questions about the possibility that dissimilar materials might have different release properties. Therefore additional studies were conducted to obtain information on the release of micro-organisms from different solid materials impacted onto two types of surfaces. The combined study was performed by inoculating 10^4 *Bacillus subtilis* var. *niger* spores into Eccobond and methyl methacrylate. These materials were then machined into projectiles and fired from guns into stainless steel plates or sand at velocities ranging from 168 to 1554 m-s^{-1}. Bacteriological examination of the fractured particles was conducted to establish the number of viable spores released from the interior of the projectiles.

Analysis of the results from two solid materials, two impact surfaces and four velocities showed that the number of micro-organisms released is less than 1% in all cases. However, statistical evaluation of all data demonstrates a significant difference in percentage microbial release between materials. Since significant differences were observed between materials, broad extrapolations of percentage release data should be avoided until release characteristics of different classes of spacecraft solid materials have been determined.

TAYLOR, F. W.

T04 Methods and Approximations for the Computation of Transmission Profiles in the ν_4 Band of Methane in the Atmosphere of Jupiter

F. W. Taylor

J. Quant. Spectrosc. Radiat. Transfer, Vol. 12, No. 7, pp. 1151-1156, July 1972

This article discusses the validity of certain band models and scaling approximations for computing transmissions in the ν_4 band of methane along inhomogeneous paths in the atmosphere of

Jupiter. It is shown that Goody's random band model approximates the results of a rigorous numerical line-by-line calculation of the transmission profile of a Jovian model atmosphere.

TEXTOR, G. P.

T05 DSN Progress Report for May–June 1972: Mariner Mars 1971 Mission Support

G. P. Textor

Technical Report 32-1526, Vol. X, pp. 20–21,
August 15, 1972

The Mariner Mars 1971 Extended Mission utilizes the Mars Deep Space Station (DSS 14), the 64-m-diameter antenna station at Goldstone, California, for acquiring telemetry and radio metric data. The 26-m-diameter antenna stations at Madrid, Spain and Goldstone, California, however, are playing an important part maximizing the quantity and quality of the data received at DSS 14. This article describes the role of the 26-m-diameter antenna stations presently engaged in the Mariner Mars 1971 Extended Mission.

THOMPSON, A. R.

T06 The Distribution of Linear Polarization in Cassiopeia A at Wavelengths of 9.8 and 11.1 cm

G. S. Downs and A. R. Thompson (Stanford University)

Astron. J., Vol. 77, No. 2, pp. 120–133, March 1972

For abstract, see Downs, G. S.

TIMOR, U.

T07 DSN Progress Report for May–June 1972: Frame Synchronization in Time-Multiplexed PCM Telemetry With Variable Frame Length

U. Timor

Technical Report 32-1526, Vol. X, pp. 96–103,
August 15, 1972

This article presents new methods of parallel and serial synchronization for time-multiplexed phase-coherent telemetry signals. In the parallel case, i.e., when the synchronization code is transmitted on a separate channel, *M* synchronization codes are generated by concatenating a common pseudonoise-like sequence of short length with words from a self-synchronizing code. The frame synchronizer can lock on any of the M codes, which is particularly useful when frames of different lengths have to be transmitted. In the serial case, that is, when each frame starts with an identical synchronization code, false synchronization due to replicas of the code randomly generated by the data is completely eliminated by transferring the synchronization code to the quadrature channel, while the data are transmitted on the in-phase channel.

T08 **Interplex—An Efficient Multichannel PSK/PM Telemetry System**

S. Butman and U. Timor

IEEE Trans. Commun., Vol. COM-20, No. 3, pp. 415–419, June 1972

For abstract, see Butman, S.

T09 **Equivalence of Time-Multiplexed and Frequency-Multiplexed Signals in Digital Communications**

U. Timor

IEEE Trans. Commun., Vol. COM-20, No. 3, pp. 435–438, June 1972

In comparing different techniques for multiplexing N binary data signals into a single channel, time-division multiplexing (TDM) is known to have a theoretic efficiency of 100% (neglecting sync power) and thus seems to outperform frequency-division multiplexing (FDM) systems. By considering more general FDM systems, it will be shown that both TDM and FDM are equivalent and have an efficiency of 100%. The difference between the systems is in the multiplexing and demultiplexing subsystems, but not in the performance or in the generated waveforms.

TRUBERT, M. R.

T10 **Large Spacecraft Antennas: Conical Ring-Membrane Reflectors**

R. E. Oliver, M. R. Trubert, and A. H. Wilson

JPL Quarterly Technical Review, Vol. 2, No. 2, pp. 42–47, July 1972

For abstract, see Oliver, R. E.

UNTI, T. W. J.

U01 **Dissipation Mechanisms in a Pair of Solar-Wind Discontinuities**

T. W. J. Unti, G. Atkinson (Communications Research

Center), C.-S. Wu (University of Maryland), and
M. Neugebauer

J. Geophys. Res., Space Physics, Vol. 77, No. 13,
pp. 2250-2263, May 1, 1972

A pair of sharp, closely-spaced discontinuities in the solar wind was recorded by the high time resolution instruments aboard OGO 5 on March 14, 1968. There is plasma turbulence within the double structure, and there appear to be small-amplitude hydromagnetic waves radiating from the discontinuities. The generation of the plasma turbulence is discussed in terms of magnetic drift waves. Although it seems probable that the surfaces are tangential discontinuities, arguments are also advanced that the double structure may represent the Petschek mechanism in which rapid field-line merging occurs between standing waves.

VIRZI, R. A.

V01 **Scan Pointing Calibration for the Mariner Mars 1971 Spacecraft**

W. F. Havens, G. I. Jaivin, G. D. Pace, and R. A. Virzi

Technical Memorandum 33-556, August 1, 1972

For abstract, see Havens, W. F.

WELCH, L. R.

W01 **DSN Progress Report for May–June 1972: A Minimization Algorithm for a Class of Functions**

L. R. Welch

Technical Report 32-1526, Vol. X, pp. 110-112,
August 15, 1972

Let N be a positive integer and $A_0, \cdots, A_N$ be non-negative numbers with at least one positive. Define

$$G(x) = \frac{N}{x} + \sum_{k=0}^{N} A_k x^k$$

The problem is to compute $z > 0$ with

$$G(z) = \min_{x>0} G(x)$$

This article gives a simple algorithm requiring $[(3/2)(\ln N/\ln 2)] +$ 8 evaluations of a polynomial of degree $N + 1$ and 6 evaluations of its derivative. This algorithm is required to optimize the DSN resource allocation process.

WHANG, M. M.

W02 **DSN Progress Report for May–June 1972: The Use of an Interplex Modulation Technique for the Mariner Venus–Mercury 1973 Mission**

M. M. Whang

Technical Report 32-1526, Vol. X, pp. 157–160,
August 15, 1972

The use of interplex modulation for the Mariner Venus–Mercury 1973 mission necessitates modification of the station ground equipment to effect compatibility. The Simulation Conversion Assembly (SCA) is to be modified to provide a source for generation of simulated telemetry data, using interplex, for system testing, training, and software development. Implementation of the SCA hardware modifications, together with a discussion of the simulation test modes, is presented.

WICK, M. R.

W03 **DSN Progress Report for May–June 1972: Programmed Oscillator Development**

H. Donnelly and M. R. Wick

Technical Report 32-1526, Vol. X, pp. 180–185,
August 15, 1972

For abstract, see Donnelly, H.

WILSON, A. H.

W04 **Large Spacecraft Antennas: Conical Ring-Membrane Reflectors**

R. E. Oliver, M. R. Trubert, and A. H. Wilson

JPL Quarterly Technical Review, Vol. 2, No. 2, pp. 42–47,
July 1972

For abstract, see Oliver, R. E.

WILSON, L.

W05 An ESCA Study of Lunar and Terrestrial Materials

W. T. Huntress, Jr., and L. Wilson (Varian Associates)

Earth Planet. Sci. Lett., Vol. 15, pp. 59–64, May 1972

For abstract, see Huntress, W. T., Jr.

WINKELSTEIN, R.

W06 Precision Signal Power Measurement

R. Winkelstein

JPL Quarterly Technical Review, Vol. 2, No. 2, pp. 18–24, July 1972

Accurate estimation of signal power is an important DSN consideration. Ultimately, spacecraft power and weight is saved if no reserve transmitter power is needed to compensate for inaccurate measurements. Spectral measurement of the received signal has proved to be an effective method of estimating signal power over a wide dynamic range. Furthermore, on-line spectral measurements provide an important diagnostic tool for examining spacecraft anomalies. Prototype equipment installed at the DSN 64-m-diameter antenna site, the Mars Deep Space Station of the Goldstone Deep Space Communications Complex, has been successfully used to make measurements of carrier power and sideband symmetry of telemetry signals received from the Mariner Mars 1971 spacecraft.

WU, C.-S.

W07 Dissipation Mechanisms in a Pair of Solar-Wind Discontinuities

T. W. J. Unti, G. Atkinson (Communications Research Center), C.-S. Wu (University of Maryland), and M. Neugebauer

J. Geophys. Res., Space Physics, Vol. 77, No. 13, pp. 2250–2263, May 1, 1972

For abstract, see Unti, T. W. J.

YANKURA, G.

Y01 Survey of Materials for Hydrazine Propulsion Systems in Multicycle Extended Life Applications

C. D. Coulbert and G. Yankura

Technical Memorandum 33-561, September 15, 1972

For abstract, see Coulbert, C. D.

YASUI, R. K.

Y02 Solar Cell Contact Pull Strength as a Function of Pull-Test Temperature

R. K. Yasui and P. A. Berman

Technical Report 32-1563, September 1, 1972

Four types of solar-cell contacts were given pull-strength tests at temperatures between −173 and +165°C. Contacts tested were (1) solder-coated titanium–silver contacts on *n–p* cells, (2) palladium-containing titanium–silver contacts on *n–p* cells, (3) titanium–silver contacts on 0.2-mm-thick *n–p* cells, and (4) solder-coated electroless-nickel-plated contacts on *p–n* cells. Maximum pull strength was demonstrated at temperatures significantly below the air mass zero cell equilibrium temperature of +60°C. At the lowest temperatures, the chief failure mechanism was silicon fracture along crystallographic planes; at the highest temperatures, it was loss of solder strength. At intermediate temperatures, many failure mechanisms operated. Pull-strength tests give a good indication of the suitability of solar-cell contact systems for space use, and the tests reported here were the first to be carried out under simulated spaceflight temperatures. Procedures used to maximize the validity of the results are described in detail.

ZANTESON, R. A.

Z01 DSN Progress Report for May–June 1972: Improvements to Angle Data System Autocollimators

R. A. Zanteson

Technical Report 32-1526, Vol. X, pp. 191–193,
August 15, 1972

The Angle Data System of the 64-m-diameter antenna utilizes two-axis autocollimators as the optical link between the precision instrument mount and the intermediate reference optical assembly. The accuracy, resolution, and stability of these instruments directly affects the pointing accuracy of the antennas. With an accuracy and resolution of better than one arc second, great care must be taken in each phase of the design and construction.

Subject Index

Subject Categories

Acoustics
Antennas and Transmission Lines
Apollo Project
Atmospheric Entry

Bioengineering
Biology

Chemistry
Computer Programs
Control and Guidance

Earth Atmosphere
Earth Surface
Electricity and Magnetism
Electronic Components and Circuits
Environmental Sciences

Facility Engineering
Fluid Mechanics

Helios Project

Information Distribution and Display
Information Storage Devices

Information Theory

Launch Operations
Launch Vehicles
Lunar Surface

Management Systems
Mariner Jupiter-Saturn 1977 Project
Mariner Mars 1971 Project
Mariner Venus-Mercury 1973 Project
Materials, Metallic
Materials, Nonmetallic
Mathematical Sciences
Mechanics

Optics
Orbits and Trajectories

Particle Physics
Pioneer Project
Planetary Atmospheres
Planetary Exploration, Advanced
Planetary Motion
Planetary Quarantine
Planetary Surfaces
Plasma Physics
Power Sources
Propulsion, Electric
Propulsion, Liquid
Propulsion, Solid
Pyrotechnics

Quality Assurance and Reliability

Radar

Radio Astronomy
Relativity

Safety Engineering
Scientific Instruments
Shielding
Soil Sciences
Solar Phenomena
Solid-State Physics
Spectrometry

Standards, Reference
Structural Engineering

Telemetry and Command
Test Facilities and Equipment
Thermodynamics
Tracking

Viking Project

Wave Propagation

Subjects

Subject **Entry**

Acoustics
- anechoic-chamber facility for investigating aerodynamic noise M07
- model for acoustic emission from fiber-reinforced material R12

Antennas and Transmission Lines
- noise effects of spacecraft ion beam on antenna radio signal A03
- dipole antenna radiation in space–time periodic media E01
- experimental S- and X-band feed system ellipsoid reflector H11
- DSN precision antenna gain measurements J01
- repositioning of parabolic antenna panels L04
- gain calibration of horn antenna using pattern integration L08
- design of conical ring-membrane antenna reflectors O01
- error analysis of precision calibrations of RF properties of perforated plates O05
- analysis of asymmetrical antenna reflectors P05
- S- and X-band RF feed system for 64-m antenna P06
- system operating noise temperature calibrations of feed cones R06
- improvements to antenna-angle data-system autocollimators Z01

Apollo Project
- lunar subsurface exploration with coherent radar B04
- Apollo 16 mission description H05
- DSN support H05

Atmospheric Entry
- models of atmospheres of Jupiter and Saturn D02

Bioengineering
- direct fluorometric determination of urea in urine R11

Subject **Entry**

Biology
Antarctic soil microbial and ecological investigations ... C01
H14
direct fluorometric determination of urea in urine ... R11
release of microbes by materials after impact ... T03

Chemistry
mechanisms of ion–molecule reactions of propene and cyclopropane ... B03
reactions of tetramethyldiaminoalkanes with dihaloalkanes ... N03
R09
direct fluorometric determination of urea in urine ... R11
superconductivity in the alkali metal intercalates of molybdenum disulphide ... S09

Computer Programs
user's manual for VISCEL, a general-purpose program for analysis of linear viscoelastic structures ... G06
general-purpose program for analysis of linear viscoelastic structures ... G07
programs for generating telemetry predicts ... H04
program for spacecraft-maneuver turns ... J03
computer program for properties of viscoelastic structures ... J04
program for calculating the repositioning of parabolic antenna panels ... L04
critical comparison of programming languages ... M08
software for robot cognitive-operating system ... M09
Monte Carlo program used to compute neutron and gamma-ray flux spectra ... T01

Control and Guidance
attitude-control jet exhaust-plume data ... C05
Mariner Mars 1971 scan pointing calibration ... H07
computer program for spacecraft-maneuver turns ... J03
thrust vector control mechanism for solar–electric thruster array ... M05

Earth Atmosphere
study of weather-dependent characteristics of X- and K-band propagation through atmosphere ... R05

Earth Surface
Antarctic soil microbial and ecological investigations ... C01
H14
electron spectroscopy used to study lunar and terrestrial materials ... H18

Subject **Entry**

Electricity and Magnetism
  electromagnetic wave propagation and wave-vector diagram in space–time periodic media E02
  heat transfer from partially ionized argon with applied transverse magnetic field R14
  terminated capacitor-discharge firing of electroexplosive devices R15
  superconductivity in the alkali metal intercalates of molybdenum disulphide S09
  dissipation mechanisms in solar-wind discontinuities U01

Electronic Components and Circuits
  post-detection subcarrier recording subsystem D01
  programmed-oscillator development D03
  data-decoder assembly performance G03
  testing of DSN transmitter klystrons J01
  Block IV receiver development J05
  new 70-MHz limiting amplifier L01
  barrier energies in metal-insulator-metal structures L05
  probes for tracing electrical noise L09
  relation of electrical noise to equipment design L09
  evaluation of frequency multipliers M02
  solar–electric thrust subsystem breadboard M05
  performance of hydrogen maser cavity tuning servo P04
  apparatus for testing electroexplosive devices by terminated capacitor discharge R15
  simulation conversion assembly for simulated interplex telemetry W02
  solar-cell contact pull strength as function of pull-test temperature Y02

Environmental Sciences
  anechoic-chamber facility for investigating aerodynamic noise M07

Facility Engineering
  upgrading of deep space stations J01
  simulation conversion assembly for simulated interplex telemetry W02

Fluid Mechanics
  very high temperature laminar flow of gas through entrance region of cooled tube B01
  small rocket exhaust-plume data C05
  measurements of structure of ionizing shock wave in hydrogen–helium mixture L02
  heat transfer from partially ionized argon with applied transverse magnetic field R14

Subject **Entry**

Helios Project
  DSN support G02

Information Distribution and Display
  DSN telemetry-predicts generation and distribution H04
  gain calibration of horn antenna using pattern integration L08

Information Storage Devices
  post-detection subcarrier recording subsystem D01
  Mariner Mars 1971 data-storage subsystem G05

Information Theory
  Interplex: efficient phase-shift-keyed/phase-modulated telemetry system B06
  maximum likelihood method for deep space station clock synchronization using long-baseline interferometry H19
  carrier synchronization and detection of polyphase signals L06
  selection of sampling filter bandwidth for digital data detector S06
  simplified formula for mean cycle-slip time of phase-locked loops with steady-state phase error T02
  synchronization methods for time-multiplexed phase-coherent telemetry T07
  equivalence of time-multiplexed and frequency-multiplexed signals in digital communications T09

Launch Operations
  cost comparisons for planetary missions with advanced propulsion systems S10

Launch Vehicles
  cost comparisons for planetary missions with advanced propulsion systems S10

Lunar Surface
  lunar subsurface exploration with coherent radar B04
  electron spectroscopy used to study lunar and terrestrial materials H18

Management Systems
  Helios Project organization G02
  DSN Telemetry System tests K01
  integration of DSN/Manned Space Flight Network joint-usage tracking stations M11
  initial spacecraft-signal acquisition planning M13
  DSN organization R10
  DSN systems tests S11
  DSN Command System performance evaluation S14

Subject **Entry**

Mariner Jupiter-Saturn 1977 Project
  mission requirements M19
  DSN support M19
  preliminary evaluation of radio-data orbit-determination capabilities required for vicinity of Saturn O03
  proposed determination of mass and ephemeris of Saturn by radio tracking O04

Mariner Mars 1971 Project
  development and testing of propulsion subsystem C03
  data-storage subsystem G05
  scan pointing calibration H07
  evaluation of DSN Command System performance during missions S14
  DSN support T05

Mariner Venus-Mercury 1973 Project
  simulation conversion assembly for simulated interplex telemetry W02

Materials, Metallic
  survey of materials for hydrazine-propulsion systems in multicycle extended-life applications C07

Materials, Nonmetallic
  survey of materials for hydrazine-propulsion systems in multicycle extended-life applications C07
  composite materials used in solid-propellant rocket motors J04
  model for acoustic emission from fiber-reinforced material R12
  elastic properties of fiber composite laminates with statistically dispersed ply orientations R13

Mathematical Sciences
  analysis and numerical calculations for very high temperature laminar flow of gas through entrance region of cooled tube B01
  general relaxation method for inverse solution of full radiative transfer equation C04
  formal solution for field and radiation patterns of a dipole antenna in space–time periodic media E01
  electromagnetic wave propagation and wave-vector diagram in space–time periodic media E02
  maximum likelihood method for deep space station clock synchronization using long-baseline interferometry H19
  analysis of signal-to-noise ratio estimator L03
  carrier synchronization and detection of polyphase signals L06
  error analysis of precision calibrations of RF properties of perforated plates O05
  analysis of asymmetrical antenna reflectors P05

Subject **Entry**

selection of sampling filter bandwidth for digital data detector S06
calculation of effects of radiation on scientific instruments T01
simplified formula for mean cycle-slip time of phase-locked loops with steady-state phase error T02
methods and approximations for computation of transmission profiles in ν_4 band of methane in atmosphere of Jupiter T04
synchronization methods for time-multiplexed phase-coherent telemetry T07
equivalence of time-multiplexed and frequency-multiplexed signals in digital communications T09
minimization algorithm for a class of functions W01

Mechanics
computer program for properties of viscoelastic structures J04

Optics
laboratory simulation of diffuse reflectivity from a cloudy planetary atmosphere M03
measurements of Hβ line shape in transient plasma using fiber-optics slit system S12
improvements to antenna-angle data-system autocollimators Z01

Orbits and Trajectories
aiming strategies for quarantined multi-planet missions D05
preliminary evaluation of radio-data orbit-determination capabilities required for vicinity of Saturn O03

Particle Physics
solid-state detector for analysis of X-rays excited in silicate rocks by alpha-particle bombardment F02
response of silicon detector to mixed neutron and gamma field as function of shield material and thickness T01

Pioneer Project
Pioneer 10 tracking requirements D03
DSN support S02
S03
S04
S05
S11
evaluation of DSN Command System performance during missions S14

Planetary Atmospheres
models of atmospheres of Jupiter and Saturn D02
formation of spectral lines in planetary atmospheres H17

Subject **Entry**

laboratory simulation of diffuse reflectivity from a cloudy planetary atmosphere M03
composition of upper clouds of Venus R04
methods and approximations for computation of transmission profiles in ν_4 band of methane in atmosphere of Jupiter T04

Planetary Exploration, Advanced
Antarctic soil microbial and ecological investigations in preparation for detection of extraterrestrial life C01
Antarctic soil microbial and ecological investigations in preparation for Mars surface exploration H14
cost comparisons for planetary missions with advanced propulsion systems S10

Planetary Motion
proposed determination of mass and ephemeris of Saturn by radio tracking O04

Planetary Quarantine
aiming strategies for quarantined multi-planet missions D05
Antarctic soil microbial and ecological investigations: implied non-survival of Earth organisms in Martian environment H14
release of microbes by materials after impact T03

Planetary Surfaces
Antarctic soil microbial and ecological investigations in preparation for Mars surface exploration H14

Plasma Physics
noise effects of spacecraft ion beam on antenna radio signal A03
electromagnetic wave propagation and wave-vector diagram in space–time periodic media E02
measurements of structure of ionizing shock wave in hydrogen–helium mixture L02
heat transfer from partially ionized argon with applied transverse magnetic field R14
measurements of Hβ line shape in transient plasma using fiber-optics slit system S12
radiative intensity calculations for hydrogen–helium plasmas S13

Power Sources
development, design, and test of roll-up solar array H06
junction characteristics of silicon solar cells S15
effects of radioisotope thermoelectric generator radiation on scientific instruments T01

Subject **Entry**

solar-cell contact pull strength as function of pull-test temperature Y02

Propulsion, Electric
noise effects of spacecraft ion beam on antenna radio signal A03
techniques for selection of spacecraft auxiliary propulsion H12
international auxiliary-propulsion development H13
thrust subsystem breadboard M05
cost comparisons for planetary missions with advanced propulsion systems S10

Propulsion, Liquid
development and testing of Mariner Mars 1971 propulsion subsystem C03
small rocket exhaust-plume data C05
stability evaluation of rocket engine using gaseous OF_2 and gaseous B_2H_6 .... C06
survey of materials for hydrazine-propulsion systems in multicycle extended-life applications C07
techniques for selection of spacecraft auxiliary propulsion H12
international auxiliary-propulsion development H13
propulsion-subsystem structural-integrity survey J04
portable hydrazine attitude-propulsion test system M16
cost comparisons for planetary missions with advanced propulsion systems S10

Propulsion, Solid
techniques for selection of spacecraft auxiliary propulsion H12
international auxiliary-propulsion development H13
composite materials used in solid-propellant rocket motors J04
nested rocket motors J04
propulsion-subsystem structural-integrity survey J04
long-term-storage test of solid-propellant rocket motor R03
cost comparisons for planetary missions with advanced propulsion systems S10

Pyrotechnics
terminated capacitor-discharge firing of electroexplosive devices R15

Quality Assurance and Reliability
statistics of DSN Command System reliability S14
solar-cell contact pull strength as function of pull-test temperature Y02

Radar
lunar subsurface exploration with coherent radar B04
DSN planetary radar experiments J01

Subject **Entry**

Radio Astronomy
  distribution of linear polarization in Cassiopeia A at 9.8 and 11.1 cm ... D04
  DSN radio science support ... J01, L07

Relativity
  electromagnetic wave propagation and wave-vector diagram in space–time periodic media ... E02

Safety Engineering
  RF-level pocket monitor ... J01
  error analysis of precision calibrations of RF properties of perforated plates ... O05

Scientific Instruments
  solid-state detector for analysis of X-rays excited in silicate rocks by alpha-particle bombardment ... F02
  effects of radioisotope thermoelectric generator radiation on scientific instruments ... T01

Shielding
  response of silicon detector to mixed neutron and gamma field as function of shield material and thickness ... T01

Soil Sciences
  Antarctic soil microbial and ecological investigations ... C01, H14
  solid-state detector for analysis of X-rays excited in silicate rocks by alpha-particle bombardment ... F02
  electron spectroscopy used to study lunar and terrestrial materials ... H18

Solar Phenomena
  dissipation mechanisms in solar-wind discontinuities ... U01

Solid-State Physics
  user's manual for VISCEL, a general-purpose computer program for analysis of linear viscoelastic structures ... G06
  use of fracture mechanics to determine material allowables for propulsion subsystems ... J04
  barrier energies in metal-insulator-metal structures ... L05
  elastic properties of fiber composite laminates with statistically dispersed ply orientations ... R13
  thermal noise in space-charge-limited hole current in silicon ... S01
  superconductivity in the alkali metal intercalates of molybdenum disulphide ... S09
  junction characteristics of silicon solar cells ... S15

Subject **Entry**

Spectrometry
  general relaxation method for inverse solution of full radiative transfer equation C04
  solid-state detector for analysis of X-rays excited in silicate rocks by alpha-particle bombardment F02
  formation of spectral lines in planetary atmospheres H17
  electron spectroscopy used to study lunar and terrestrial materials H18
  measurements of structure of ionizing shock wave in hydrogen–helium mixture L02
  laboratory simulation of diffuse reflectivity from a cloudy planetary atmosphere M03
  intensity and half-width measurements of (00°2–00°0) band of N_2O M04
  composition of upper clouds of Venus R04
  measurements of $H\beta$ line shape in transient plasma using fiber-optics slit system S12
  radiative intensity calculations for hydrogen–helium plasmas S13
  methods and approximations for computation of transmission profiles in ν_4 band of methane in atmosphere of Jupiter T04

Standards, Reference
  deep space station clock synchronization by long-baseline interferometry H19
  DSN clock synchronization transmissions J01

Structural Engineering
  user's manual for VISCEL, a general-purpose computer program for analysis of linear viscoelastic structures G06
  general-purpose computer program for analysis of linear viscoelastic structures G07
  propulsion-subsystem structural-integrity survey J04
  design of conical ring-membrane antenna reflectors O01
  elastic properties of fiber composite laminates with statistically dispersed ply orientations R13

Telemetry and Command
  Interplex: efficient phase-shift-keyed/phase-modulated telemetry system B06
  third-order tracking filter C08
  DSN support of Helios Project G02
  data-decoder assembly performance G03
  DSN telemetry-predicts generation and distribution H04
  DSN support of Apollo Project H05
  DSN Telemetry System tests K01
  carrier synchronization and detection of polyphase signals L06

Subject **Entry**

DSN support of Viking Project M18
DSN support of Mariner Jupiter-Saturn 1977 Project M19
DSN functions and facilities R10
DSN support of Pioneer Project S02
S03
S04
S05
selection of sampling filter bandwidth for digital data detector S06
DSN Command System performance evaluation S14
simplified formula for mean cycle-slip time of phase-locked loops with steady-state phase error T02
DSN support of Mariner Mars 1971 Project T05
synchronization methods for time-multiplexed phase-coherent telemetry T07
equivalence of time-multiplexed and frequency-multiplexed signals in digital communications T09
simulation conversion assembly for simulated interplex telemetry W02

Test Facilities and Equipment
Molsink vacuum facility used to study small rocket exhaust plumes C05
apparatus for stability evaluation of rocket engine C06
solid-state detector for analysis of X-rays excited in silicate rocks by alpha-particle bombardment F02
equipment for testing roll-up solar array H06
apparatus for laboratory simulation of diffuse reflectivity from a cloudy planetary atmosphere M03
anechoic-chamber facility for investigating aerodynamic noise M07
portable hydrazine attitude-propulsion test system M16
tuned reflectometer system for testing RF properties of perforated plates O05
apparatus for experimental determination of heat transfer from partially ionized argon with applied transverse magnetic field R14
apparatus for testing electroexplosive devices by terminated capacitor discharge R15
measurements of Hβ line shape in transient plasma using fiber-optics slit system S12
device for study of effects of impact on release of microbes from materials T03
facilities for testing solar-cell contact pull strength Y02

Subject **Entry**

Thermodynamics
- very high temperature laminar flow of gas through entrance region of cooled tube ... B01
- measurements of structure of ionizing shock wave in hydrogen–helium mixture ... L02
- heat transfer from partially ionized argon with applied transverse magnetic field ... R14
- measurements of Hβ line shape in transient plasma using fiber-optics slit system ... S12

Tracking
- third-order tracking filter ... C08
- Pioneer 10 tracking requirements ... D03
- DSN support of Helios Project ... G02
- DSN support of Apollo Project ... H05
- integration of DSN/Manned Space Flight Network joint-usage tracking stations ... M11
- initial spacecraft-signal acquisition planning ... M13
- DSN support of Viking Project ... M18
- DSN support of Mariner Jupiter–Saturn 1977 Project ... M19
- preliminary evaluation of radio-data orbit-determination capabilities required for vicinity of Saturn ... O03
- proposed determination of mass and ephemeris of Saturn by radio tracking ... O04
- performance of hydrogen maser cavity tuning servo ... P04
- study of weather-dependent characteristics of X- and K-band propagation through atmosphere ... R05
- DSN support of Pioneer Project ... S02, S03, S04, S05
- DSN support of Mariner Mars 1971 Project ... T05

Viking Project
- DSN support ... M18

Wave Propagation
- noise effects of spacecraft ion beam on antenna radio signal ... A03
- Interplex: efficient phase-shift-keyed/phase-modulated telemetry system ... B06
- third-order tracking filter ... C08
- programmed-oscillator development ... D03
- dipole antenna radiation in space–time periodic media ... E01
- electromagnetic wave propagation and wave-vector diagram in space–time periodic media ... E02
- deep space station clock synchronization by long-baseline interferometry ... H19

Subject **Entry**

Block IV receiver development ... J05
new 70-MHz limiting amplifier ... L01
analysis of signal-to-noise ratio estimator ... L03
repositioning of parabolic antenna panels ... L04
carrier synchronization and detection of polyphase signals ... L06
error analysis of precision calibrations of RF properties of perforated plates ... O05
analysis of asymmetrical antenna reflectors ... P05
study of weather-dependent characteristics of X- and K-band propagation through atmosphere ... R05
DSN functions and facilities ... R10
simplified formula for mean cycle-slip time of phase-locked loops with steady-state phase error ... T02
equivalence of time-multiplexed and frequency-multiplexed signals in digital communications ... T09
precision signal-power measurement ... W06

Publication Index

Technical Reports

Number	Entry
32-1505, Suppl. 1	H12
32-1561	C06
32-1562	H06
32-1563	Y02
32-1564	M07
32-1572	L08

DSN Progress Report for May–June 1972 (Technical Report 32-1526, Vol. X)

JPL Technical Section		Entry
331	Communications Systems Research	H19 M02 T07 W01
332	DSIF Engineering	H11 L04 L09 Z01
333	Communications Elements Research	O05 P04 P05 P06 R05

333 Communications Elements Research (contd) R06

335 R. F. Systems Development C08, D03, J01, J05, L01

337 DSIF Operations L03, M13

338 DSIF Digital Systems Development D01, G03, M11, W02

391 Tracking and Orbit Determination O03, O04

401 DSN Engineering and Operations Office H04, H05, K01, S11, S14, T05

420 Mission Support Office G02, L07, M18, M19, R10, S02, S03, S04

Technical Memorandums

Number	Entry
33-426, Vol. X	S05
33-466, Vol. I, Rev. 1	G06
33-466, Vol. II	G07
33-552	C03
33-553	S10
33-554	G05
33-555	H13

33-556	H07
33-557, Pt. I	S15
33-558	J03
33-560	M16
33-561	C07
33-562	J04
33-563	L02
33-564	R12
33-566	M08
33-568	M09

JPL Quarterly Technical Review, Vol. 2, No. 2

JPL Technical Division		Entry
290	Project Engineering	D02
330	Telecommunications	A03 W06
340	Guidance and Control	T01
350	Engineering Mechanics	O01 R13
360	Astrionics	S01
370	Environmental Sciences	O01
380	Propulsion	C05 M05 R03 S09
390	Mission Analysis	D05

Open Literature Reporting

Advances in X-Ray Analysis	Entry
Vol. 15, pp. 388–406	F02

AIAA Tenth Aerospace Sciences Meeting, San Diego, California, January 17–19, 1972	Entry
Preprint 72-106	S12

Appl. Opt.	Entry
Vol. 11, No. 5, pp. 1212–1216	M03

Astron. J.	Entry
Vol. 77, No. 2, pp. 120–133	D04

Clinical Chem.	Entry
Vol. 18, No. 5, pp. 476–478	R11

Earth Planet. Sci. Lett.	Entry
Vol. 15, pp. 59–64	H18

IEEE Trans. Anten. Prop.	Entry
Vol. AP-20, No. 3, pp. 280–287	E01
Vol. AP-20, No. 4, pp. 534–536	E02

IEEE Trans. Commun.	Entry
Vol. COM-20, No. 3, pp. 331–337	T02
Vol. COM-20, No. 3, pp. 415–419	B06
Vol. COM-20, No. 3, pp. 435–438	T09
Vol. COM-20, No. 3, pp. 438–441	S06
Vol. COM-20, No. 3, pp. 441–454	L06

IEEE Trans. Instr. Meas.	Entry
Vol. IM-21, No. 2, pp. 177–180	R15

Int. J. Heat Mass Transfer	Entry
Vol. 15, No. 5, pp. 1001–1021	B01

J. Am. Chem. Soc.	Entry
Vol. 94, No. 12, pp. 4255–4261	B03

J. Appl. Phys.	**Entry**
Vol. 43, No. 4, pp. 1764–1767	L05

J. Atmos. Sci.	**Entry**
Vol. 29, No. 4, pp. 741–747	C04

J. Geophys. Res., Space Physics	**Entry**
Vol. 77, No. 13, pp. 2250–2263	U01

J. Quant. Spectrosc. Radiat. Transfer	**Entry**
Vol. 12, No. 4, pp. 525–529	S13
Vol. 12, No. 4, pp. 751–757	M04
Vol. 12, No. 6, pp. 1023–1028	H17
Vol. 12, No. 7, pp. 1151–1156	T04

Life Sciences and Space Research X	**Entry**
pp. 23–28	T03

Macromolecules	**Entry**
Vol. 5, No. 3, pp. 253–260	N03
Vol. 5, No. 3, pp. 261–269	R09

Phycologia	**Entry**
Vol. 11, No. 2, pp. 133–139	C01

Rev. Geophys. Space Phys.	**Entry**
Vol. 10, No. 1, pp. 369–378	R04

Science	**Entry**
Vol. 176, No. 4032, pp. 242–245	H14

The Moon	**Entry**
Vol. 4, pp. 113–127	B04

Trans. ASME, Ser. C: J. Heat Transf. **Entry**

Vol. 94, No. 2, pp. 174–180 .... R14

NASA — JPL — Coml., L.A., Calif.

JPL Quarterly Technical Review
Volume 2, Number 2

Jet Propulsion Laboratory
California Institute of Technology
4800 Oak Grove Drive
Pasadena, California 91103

Prepared Under Contract NAS 7-100
National Aeronautics and Space Administration

Requests for copies of JPL publications should be made in writing to the attention of: Manager, Technical Information and Documentation Division Support Section 651.